ELECTROCHEMICAL AND SURFACE PLASMON BIOASSAYS FOR CIRCULATING BIOMARKERS

By

ALUTH GEDARA GAYAN CHANDIMA PREMARATNE

Bachelor of Science
St. Joseph's College of Arts and Science
(Affiliated to Bangalore University)
Bangalore, India
2010

Master of Science in Analytical Chemistry
University of Colombo
Colombo, Sri Lanka
2014

Submitted to the Faculty of the
Graduate College of the
Oklahoma State University
in partial fulfillment of
the requirements for
the Degree of
DOCTOR OF PHILOSOPHY
July, 2018

ELECTROCHEMICAL AND SURFACE PLASMON

BIOASSAYS FOR CIRCULATING BIOMARKERS

Dissertation Approved:

Dr. Sadagopan Krishnan

Dissertation Adviser

Dr. Ziad El Rassi

Committee Member

Dr. Richard A. Bunce

Committee Member

Dr. Toby Larue Nelson

Committee Member

Dr. Edralin Aguinaldo Lucas

Outside Committee Member

ACKNOWLEDGEMENTS

There is a number of special people without whose support this doctoral journey might have not been possible, and to whom I am greatly indebted. Firstly, I would like to express my deepest gratitude to my PhD advisor Dr. Sadagopan Krishnan, for his full support, patience, motivation, guidance and the immense amount of opportunities given to succeed in my graduate career. I could not have imagined having a better advisor and mentor for my doctoral study. Also I would like to thank my thesis committee members: Dr. Ziad El Rassi, Dr. Richard Bunce and Dr. Toby Nelson of the Department of Chemistry, and Dr. Edralin Lucas of the Department of Nutritional Sciences for their insightful comments and support provided to develop my research. I would like to thankfully remember the former committee members Dr. John Gelder and Dr. Gabriel Cook of the Department of Chemistry for their support.

A special thank goes to the faculty members, staff of the Department of Chemistry for their continuous assistance, and Chemistry and Physics Machine Shop for their tremendous support in designing the microfluidic systems for different projects. I would like to express my heartiest thank to the Department of Chemistry, the Graduate College and the Service and Learning Volunteer Center of Oklahoma State University for rendering numerous awards, scholarships and fellowships. Furthermore, I would like to thank the Electrochemical Society and the American Chemical Society for awarding me with travel awards to present at their national research conferences.

I would like to thank the past and present members of our group: Dr. Charuksha Walgama, Dr. Manoj K. Patel, Dr. Rajasekhar Nerimetla, Dr. Vini Singh, Dr. K. Sudakar Prasad, Asantha Dharmaratne, Jinesh Niroula, Zainab Al Mubarak, James Moulton, Sabrina Farias, Jimmy Dickinson, Mayowa Akinwale, Ryan Matlock, Trey Sunday and Anuruddha Pathiranage. Without their enthusiasm and corporation, research would have been a frustrating and overwhelming pursuit.

I should make a special note of thanks the faculty members of St. Joseph's College of Arts and Science, Bangalore, India and the Department of Chemistry of University of Colombo, Sri Lanka for setting a solid foundation in science education, which motivated me to pursue a PhD. I would also like to remember all my teachers and mentors from Mahanama College, Colombo 03, Sri Lanka who have truly been an inspiration during my primary, middle and high school education. A heartiest thank goes to the management and the staff members of the S.G.S Lanka (Pvt) Ltd for giving me enormous number of opportunities for professional growth.

I am truly grateful and thankful to my loving mother (Indumathi Aponso), father (Aluth Gedara Premaratne), and my siblings for their love and continuous encouragement. Most of all, a heartiest thank goes to my wonderful wife, Krishani Rajapaksa, who has been loving, supportive, encouraging and patient all throughout my PhD. Last but not least, I would like to dedicate this PhD dissertation to my loving son, Nisith Sudam Premaratne.

Gayan Premaratne
Oklahoma State University, Stillwater
July, 2018

Name: ALUTH GEDARA GAYAN CHANDIMA PREMARATNE

Date of Degree: JULY, 2018

Title of Study: ELECTROCHEMICAL AND SURFACE PLASMON BIOASSAYS FOR CIRCULATING BIOMARKERS

Major Field: CHEMISTRY

Abstract: To address analytical detection needs, sensitive and selective assay methodologies are of great importance. Compared to simple buffer medium, a great challenge exists in detecting ultra-low levels of biomarkers in clinical matrices due to their inherent complexity and interferences posed by non-specific molecules. In addition, small molecules do not yield measurable assay signal changes compared to large biomolecules. My thesis research is focused on designing nano-biological interfaces to detect small and large molecules at low parts-per-billion and femto/picomolar concentrations in complex biofluids (serum and urine samples). Compared to harsh and tedious chemical carboxylation, non-covalent carboxylation of multiwalled carbon nanotubes by π-π stacking 1-pyrenebutyric acid retains the innate sp^2 structure and electronic properties of the nanotubes and offers surface carboxyl groups for stable covalent amine coupling of a large amount of enzymes, thus improving the sensitivity of the assay. Chapter 2 demonstrates the first pyrenyl carbon nanostructure modified enzymatic bioelectrode for amperometric detection of urine formaldehyde at clinically relevant parts-per-billion levels with selectivity and wide dynamic range. Subsequently, we explored the low dielectric permittivity and intrinsic plasmonics of graphene for the detection of serum glutamic acid decarboxylase autoantibody (GADA). Graphene-based electrochemical immunosensing approach is advantageous due to its additional applicability for surface plasmon based validation and binding strength analysis with surface immobilized GAD-65 antigens (Chapter 3). My thesis focused on the third class of biomarkers, microRNAs, which are small oligonucleotides with 21-25 bases. To develop the microRNA assay with quantitative characterization, surface plasmon resonance imaging (SPRi) coupled with quartz crystal microbalance (QCM) was designed (Chapter 4). Gold nanoparticles (Au NPs) were linked to the oligonucleotides to increase the detection sensitivity upon hybridization with the selective capture oligonucleotide immobilized on the sensor surface with minimal non-specific signals. Often, cancer and other similar health disorders have been shown to be related to various types of biomarkers. Hence, in Chapter 5, we designed a multiplex assay platform for combined measurement of proteins and microRNAs. For this multiplex assay, we synthesized iron-gold bimetallic core/shell nanoparticles (Fe_3O_4@Au NPs) that displayed a greater plasmonic signal amplification than either Fe_3O_4 or Au NPs.
.

TABLE OF CONTENTS

CHAPTER 1 PAGE

LIST OF TABLES

CHAPTER 2

TABLE PAGE

CHAPTER 3

TABLE PAGE

CHAPTER 4

TABLE PAGE

CHAPTER 5

TABLE PAGE

LIST OF FIGURES

CHAPTER 1

FIGURE PAGE

CHAPTER 2

FIGURE PAGE

CHAPTER 3

FIGURE PAGE

CHAPTER 4

FIGURE PAGE

CHAPTER 5

FIGURE PAGE

CHAPTER 1

ELECTROCHEMICAL AND SURFACE PLASMON BIOASSAYS FOR CIRCULATING BIOMARKERS

1.1 Introduction

Designing highly sensitive and selective bioassay methodologies is imperative to overcome the analytical challenge of not only determining the ultra-low concentrations of biomarkers that are present in complex matrices (blood, serum, urine, saliva, etc.), but also to assess slight variations occurring during physiological abnormalities. Biomarkers are specific molecules whose concentration levels in blood, tissues and other organs/body fluids can be related to a normal or abnormal process, or a condition or disease.[1] Assaying clinically relevant biomarkers present in complex body fluids can enable early diagnosis and monitoring response to treatments as well as recurrence. An outline of various types of biomarkers and their applicability with relevance to different stages of disease depending on their biological function is shown in Figure 1.

Even though many sensitive techniques including chromatography-mass spectrometry, radioactive assays, and molecular biology techniques are known, high cost, complexity of assay steps for clinical samples, limitation of assaying in a multiplex format, no feature of real-time binding analysis (useful for sensitive biosensor development by facilitating conditions to attain strong interactions), and the need of expensive labels for the detection steps.

Electrochemical techniques have received immense attention because they are simple to operate, easy to fabricate, produce rapid detection signals, cost effective, and can be used as miniaturized

platforms for onsite measurements.[2,3] Surface plasmon resonance (SPR) has been predominantly used as a sensitive technique that could measure real-time ligand-receptor binding events and the kinetics associated with them.[4,5] Combining electrochemical and SPR techniques can provide complementing information useful for any new bioanalytical assay development.

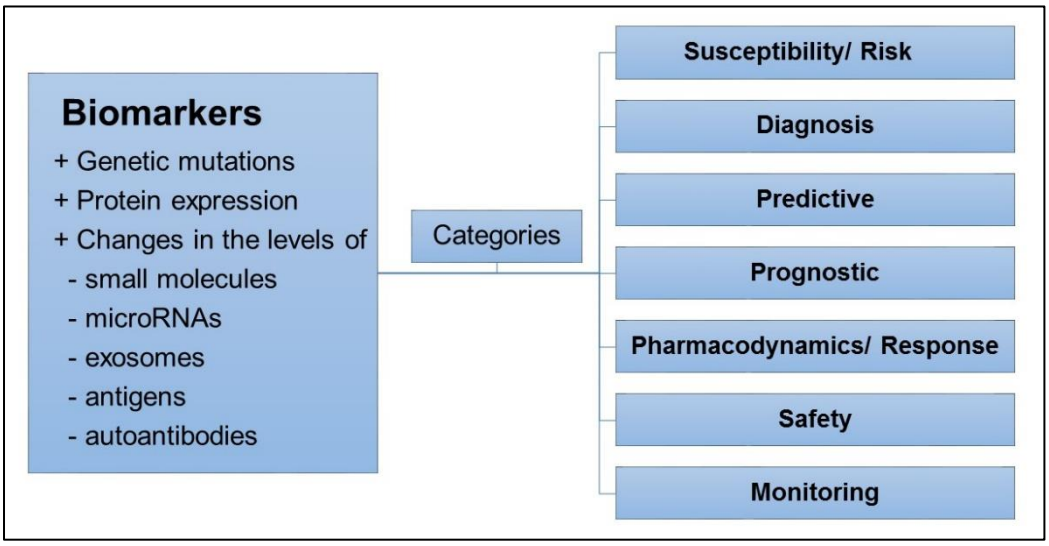

Figure 1. Types of biomarkers and the categories they fall under according to their potential roles (according to FDA, NIH and JDRF Biomarker Working Group categorization)

Both electrochemical and SPR biosensors carry or consist of the same basic elements as of a general biosensor. A bio-recognition molecule, specific for the target analyte, is immobilized on the surface and a transducer producing the desired signal change when the target analyte binds to the surface receptor.[6] These biosensors face the general limitations of suffering from non-specific signals, orientation issues of surface receptors affecting the extent of analyte binding sites, and long-term stability. To mitigate some of these drawbacks, various nanomaterials and surface bioconjugation chemistries to improve the detection sensitivity, orientation, and stability. In addition to addressing these common pitfalls, we have initiated a research direction focusing on binding constant based biosensor optimization to increase detection sensitivity and thus lower the detection limits.

This chapter provides an overview of recent trends in electrochemical and surface plasmon resonance (SPR) bioassays for small and large biomolecule markers. A summary of contribution from my thesis research on the design of various bioassay strategies is presented (Figure 2). Furthermore, the use of appropriate surface recognition elements and incorporation of different nanomaterial-based approaches for signal amplification and non-specific signal reduction are discussed.

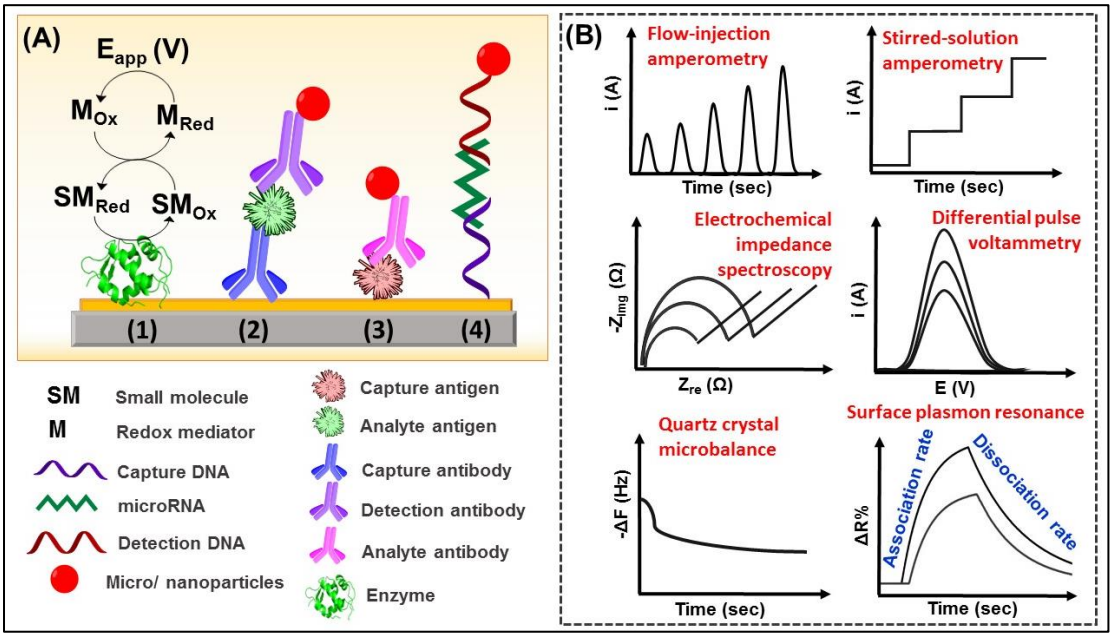

Figure 2. A. Schematic of different assay strategies designed in this thesis to measure biomarkers in clinical matrices: (1) small molecules, (2) antigens, (3) antibodies and (4) microRNAs. **B.** Various electrochemical and surface plasmon imaging-based detection strategies were utilized.

1.2 Nanostructure-modified enzyme electrodes

Enzyme-based electrochemical sensors are a sub-class of biosensors that are built by immobilizing substrate-specific enzymes on the working electrode surface. Electrochemical signals are produced as a result of the enzyme catalyzing the small molecule of interest. As the most critical component of the sensor, enzymes can be stably immobilized on the sensor by use of various nanomaterials

and nanocomposites as a type to improve sensitivity.[7] The analyte small molecule can be selectively probed as the substrate for a specific enzyme irrespective of the matrix it is available.

Thulium oxide nanorods (n-Tm_2O_3) electrophoretically-deposited onto indium-tin oxide glass electrode for total cholesterol detection in clinical samples through a dual enzyme functionalization (with cholesterol esterase (ChEt) and cholesterol oxidase (ChOx)) has been reported.[8] Tm_2O_3 improved the electroactive area, diffusion of substrates to the enzymes and electron transfer kinetics that resulted in a broad linear range for cholesterol detection. A poly(phenylenediamine) biomembrane with a molecular sieving feature was developed to amperometrically determine the glutamate uptake and accumulation in the nerve terminals at millimolar levels.[9] The biomembrane resulted storage stability up to 11 days at 4 ^{o}C with a loss of 25% of initial activity. Without the biomembrane, the sensor showed a large cross-reactivity with ascorbic acid, which was not clearly addressed. A reagentless amperometric biosensor was developed by Hughes *et al.* following a layer-by-layer process by alternatively depositing chitosan and multiwalled carbon nanotubes (MWNTs) on Meldola's Blue screen printed carbon electrodes.[10] The layers encapsulated the glutamate dehydrogenase enzyme and the cofactor nicotinamide adenine dinucleotide (NAD^+). The sensor had the capacity to determine glutamate concentrations in food and serum samples with less than 10% coefficient of variation among five replicates. Reagentless enzymatic amperometric biosensor eliminates the requirement for additional redox probes during the detection step, which decreases the assay duration. However, the effectiveness of layer-by-layer modification on the reproducibility and shelf-life of the sensor needs to be further investigated.

As another mechanistic approach to entrap large quantities of enzymes, Reuillard and coworkers developed an amperometric glucose sensor, which was efficiently built by polypyrrolic bipyridine bis(phenantrolinequinone) Ru(II) complex ($[Ru^{II}(PhQ)_2(bpy\text{-}pyrrole)]$) formed by eletropolymerization on a MWNT-modified glassy carbon electrode (GCE).[11] This one-step

development of [$Ru^{II}(PhQ)_2$(bpy-pyrrole)] nano-polymer composite was compared to a layer-by-layer deposition of [$Ru^{II}(PhQ)_2$(bpy-pyrrole)] and poly[12-(pyrrol-1-yl) dodecyl]triethylamnonium tetrafluoroborate. Even though the layer-by-layer method entrapped more enzymes, the sensor performance was poor due to additional steric effects imposed on cofactor permeation towards the electrocatalytic layer. Recently, a nanostructured enzyme-less glucose sensor was developed on a glassy carbon electrode modified with a nanohybrid mixture of MWNTs/Au NPs/iron oxide nanoparticles (Fe_2O_3 NPs).[12] The aggregation of Fe_2O_3 NPs above an optimum concentration hindered the electron transfer through MWNTs, which in turn lowered the sensitivity of the sensor by 2-folds.

1.3 Pyrenyl carbon nanostructures for ultrasensitive measurements of formaldehyde in urine (Chapter 2)

1.3.1 Approach and novelty

We recently demonstrated a novel approach for enzyme-selective detection of formaldehyde in urine using a flow injection amperometric sensor (Figure 3).[13] An amperometric nano-bioelectrode design that uniquely combined 1-pyrenebutyric acid (PBA) units pi-pi stacked with carboxylated MWNTs on the surface of gold screen printed electrodes was used for covalent attachment of NAD^+ dependent formaldehyde dehydrogenase (FDH). Based on our prior reports, the large number of –COOH groups made available by MWNT/PBA modification promotes greater covalent attachment of surface biomolecules,[14-16] and is convenient to perform compared to the tedious chemical functionalization of MWNTs that could potentially alter their electronic properties. FDH is a selective enzyme towards formaldehyde oxidation, which minimized non-specific interferences. Fourier transform infrared, Raman, and electrochemical impedance spectroscopic characterizations confirmed the successful design of the FDH bioelectrode. An electron transfer mediator-based efficient approach using quinone compound (Q: 1, 2-naphthaquinone-4-sulfonic

acid sodium salt) was followed to obtain electrochemical signals that are proportional to formaldehyde concentration.

1.3.2 Outcomes and significance

The non-covalent functionalization of MWNTs with PBA offered a larger amount of carboxyl functionalities, which in turn was useful to covalently immobilize a large amount of FDH on the electrode surface to increase the sensitivity. Flow injection analysis provided greater affinity for formaldehyde (apparent K_M 9.6 ± 1.2 ppm) when compared with stirred solution method (apparent K_M 19.9 ± 4.6 ppm). The flow injection analysis demonstrated a lower detection limit and wider dynamic range than the stirred solution method in 10-times diluted urine matrix. This could be likely due to the better diffusion of reactants to products on the electrode surface by use of a continuous sample flow. The sensor offered a superior selectivity over other homologous aldehydes except for a moderate cross-reaction with acetaldehyde (~25%) possibly due to its partial affinity to the enzyme's binding pocket.[17]

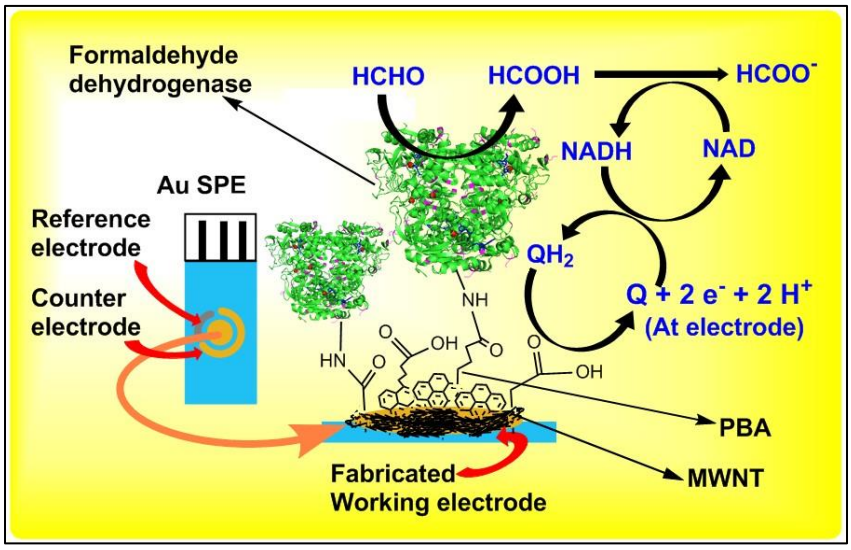

Figure 3. Pyrenyl-carbon nanostructure-modified disposable electrode for urine formaldehyde detection.

Our results demonstrated that pyrenyl carbon nanostructure-based FDH bioelectrode design represent a novel and simple for enzyme-selective electrochemical quantitation of small 30 Da formaldehyde. Broader applicability of our approach to other small-molecule markers is feasible depending on the design of appropriate marker-specific enzyme systems or receptor molecules.

1.4 Ultrasensitive electrochemical immunoassays

Nano-modified electrochemical immunoassays have received a sound attention in past few years in the rapidly growing biomarker sensing applications.[18] A typical electrochemical immunoassay consists of a reporter molecule which is responsible to produce the corresponding electrical signal upon the target molecule is bound to the specific receptor. Dutta and coworkers reported a sandwich type immunosensor to determine the low femtogram per milliliter concentration of *Plasmodium falciparum* histidine-rich protein-2 in plasma.[19] A highly sensitive redox-cycling approach was followed by using methylene blue tagged second antibodies to produce chronocoulometric signals after going through an endergonic reaction with $Ru(NH_3)_6^{3+}$ and a highly exergonic reaction with tris (2-carboxyethyl)phosphine (TCEP). This eliminated the requirement for expensive enzymatic labels and demonstrated high specificity, excellent reproducibility and good stability. Another highly sensitive immunosensing platform, which measured femtogram per milliliter levels of a food-borne pathogen marker *Enteropathogenic coli* (*E. coli*) antigen, a unique and highly sensitive redox-cycling detection mechanism was followed.[20] The outersphere reaction-philic/innersphere reaction-philic transfer from $Ru(NH_3)_6^{3+/2+}$/immunosensor to ferritin-H_2O_2 redox system resulted in a higher signal to noise ratio than a traditional ferritin labeled immunoassay. While this redox-cycling scheme offered similar sensitivity to the methylene blue-TCEP redox system, it has the advantage of having negligible interference from dissolved oxygen in the electro-reduction process.

A major number of immunosensors developed recently have been focused on determining biomarkers related to various cancer conditions. In this effort, an enzyme cascade reaction was

employed to measure serum concentration of a tumor marker neuron-specific enolase (NSE) utilizing a multifunctional conductive hydrogel containing polypyrrole-polythionine-Au NPs with glucose oxidase due to its ease of synthesis through a one-pot reaction, large specific surface area offered and high conductivity and signal to noise ratio.[21] However, the inherent mechanical weakness and non-adherence to certain surfaces could limit the use of hydrogels in biosensors.

Carvajal and coworkers reported a low-cost disposable inkjet-printed electrode array (< $0.25) to detect clinically relevant levels of a breast cancer biomarker human epidermal growth factor receptor 2 (HER-2).[22] Even though a relatively faster assay time (15 min) were achieved by an integrated flow of HER-2, biotinylated antibody, and polymerized horseradish peroxide labels *via* a microfluidic system, this study did not demonstrate any evidence that mimics the real-use of determining HER-2 in human serum. A direct immunoassay was built on disposable graphene screen-printed electrode modified with branched polyethylenimine to detect serum glial fibrillary acidic protein, a central nervous system injury biomarker.[23] The simple adsorption of PEI provided enriched amounts of primary and secondary amine functional groups for the immobilization of a large amount of capture antibody via a Schiff base reaction using glutaraldehyde. This was advantageous over the creation of self-assembled monolayers, electropolymerization, plasma-polymerization, and salts with functional groups that have complex protocols with several time-consuming functionalization steps. Nonetheless, adsorbed layers of polymers are prone to desorption due to strong mechanical stress applied on the sensor, which in turn, could hamper the sensitivity.

Recently, significant efforts have been put by scientists in regard to measurements of insulin levels in clinical matrices to draw plausible conclusions on diabetic conditions. Krishnan and coworkers reported electrochemical immunosensor designs that employed MWNTs non-covalently functionalized with 1-pyrenebutyric acid by pi-pi stacking to increase the surface carboxyl

functional groups, which in turn improved the amount of immobilized anti-insulin second antibodies to detect low picomolar levels of insulin in diluted human serum.[24,25] Magnetic nanoparticles covalently linked with anti-insulin capture antibodies were used to conveniently capture the serum insulin, which reduced the possible non-specific signals and increased the sensitivity of the detection signals.

1.5 Electrochemical and surface plasmon correlation of serum autoantibody immunoassay with binding insights: graphenyl vs. mercapto-monolayer surface (Chapter 3)

1.5.1 Approach and novelty

Conventionally, radioimmunoassay (RIA), enzyme-linked immunosorbent assay (ELISA), chemiluminescent immunoarray (CLIA), and electrochemiluminescence assays have been used by the researchers for clinical diagnosis of type 1 diabetes (T1D). These analytical techniques are tedious to perform, lacked quality check parameters and required expensive labels. We developed an immunosensor design on carboxylated graphene (graphene-COOH) or self-assembled monolayer of mercaptopropionic acid (MPA)-modified screen printed eight electrode array (8xAuSPE). We used an inexpensive ferricyanide reagent to accomplish the simple electrochemical detection of serum glutamic acid decarboxylase autoantibody (GADA) (Figure 4).[26] According to prior studies, both graphene[27-29] and mercapto monolayers[30-32] have been widely used to effectively functionalize immunoassay surfaces in order to immobilize biomolecules.

Graphene is an excellent alternative to surface chemistries that cannot be directly used on surface plasmon resonance imager (SPRi) array surface due to optical limitations (e.g., carbon nanotubes). With its conductive 2D nanostructure and intrinsic plasmonic activity, graphene can be used for both electrochemical and SPR surface modification. Herein, we used SPRi as a complementary method to the electrochemical methods to evaluate binding constants (K_D) associated with GADA interaction with its antigen, GAD-65. A unique approach was followed to isolate the GAD antibody

from serum samples by protein A/G modified magnetic beads to minimize non-specific interactions. This comparative analysis of the graphene-COOH and MPA provided useful fundamental information regarding immunosensing of serum GADA and binding insights on GADA-GAD65 interaction, which are discussed in detail in Chapter 3.

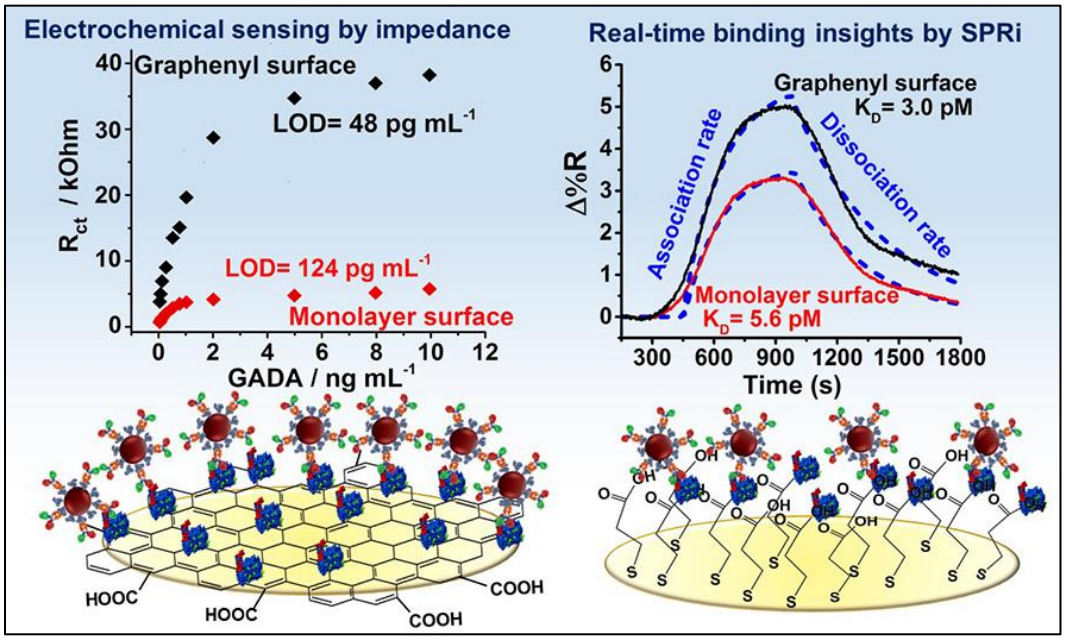

Figure 4. Immunosensor containing Graphene-COOH and MPA monolayers for serum GADA measurement and binding kinetic determination.

1.5.2 Outcomes and significance

The graphene surface offered a lower detection limit with a wider dynamic range compared to the MPA monolayer surface, and exhibited a good statistical correlation with the commercial ELISA method. The lower K_D value for the graphene-COOH modified surface suggests that graphene provides a stronger GADA-GAD-65 binding interaction, which in turn relates to a more sensitive platform. Through electrochemical quantitation, it was found that the number of surface carboxyl groups available for covalent interaction was about 9-times greater in graphene-COOH than the mercapto monolayer surface. The larger number of carboxyl groups on graphene provided room to immobilize a greater amount of GAD-65 antigen combined with the reduction of non-specific

binding occurring on the immunosensor surface, which improved sensitivity. The combined sensing and binding assessment studies provided useful insights for broader applications on developing reliable, and better throughput clinical immunosensors for biomarker based diagnostic assays.

1.6 SPRi bioassays for protein and nucleotide biomarkers

SPRi is one of the many SPR techniques that have been established, and can operate as a high-throughput and label-free technique for the analysis of variety of molecular interactions. Typical SPRi works based on Kretschmann configuration in which a monochromatic light source is used to generate surface plasmons across an array consisting of a thin plasmonic metal film in contact with a dielectric medium. A CCD camera is used to acquire digital images to monitor the intensity of light reflected as a result of refractive index changes occurring at the metal-dielectric interface.[33] To increase the sensitivity of the SPRi-based detection, various surface nanomaterial assemblies, enzymatic amplification, self-assembly of proteins and DNAs and plasmonic nanoparticle coupling have been followed.[34]

Sankiewicz and coworkers developed an SPR assay to measure fibronectin in blood samples of children with thermal injuries.[35] The assay used a simple immunoassay strategy by immobilizing fibronectin specific monoclonal antibodies on a mercapto monolayer formed on the gold SPRi array and did not require any tags, dyes or specialized reagents. However, the assay sensitivity was only moderate with the detection limit of 1.5 ng mL^{-1}, limiting its use to measure biomarkers of clinical relevance in ultralow picogram or femtogram per milliliter levels. In another work, an orthogonal signal amplification strategy was followed by coupling a miRNA-initiated surficial cyclic DNA-DNA hybridization reaction with a DNA-initiated upward cyclic polymerization reaction.[36] In this way the sensitivity was improved to sub-femtomolar concentration detection. However, this

method has an intrinsic limitation while applying to a multiplexing platform as it would require the design of multiple DNA oligonucleotides if a panel of miRNA markers are to be tested.

Multiplexing combined with a microfluidic format allows a rapid and efficient analysis of multiple biomarkers, minimizing the need for multiple experiments. Hendriks and coworkers recently developed a multiplexed SPRi detection cascade using neutravidin and gold nanoparticles to measure IL-1β, IL-6, IFN-γ, and TNF-α in femtogram and picogram per milliliter range.[37] Though the enhancement cascade improved the sensitivity by about 40,000 times in a buffer medium, when applied to complex fluids, large non-specific interactions of the surface receptor antibodies led to a 1000-fold decrease in the overall sensitivity of the assay. In another recent report, a competitive multiplexed SPRi immunoassay was developed to measure insulin, glucagon and somatostatin in buffer medium.[38] The indirect assay was useful to overcome the limitation arising from small molecule detection signals by SPRi, which would often result in no measurable signal changes at ultralow concentrations. The drawback in such assay is that it has detection limits in the nanomolar range and has not achieved measurements of markers under study in any complex matrix.

SPRi can become a vital complementary technique to electrochemical methods by enabling real-time binding insights on various types of molecules associated with appropriate receptor molecules immobilized on the array surface. Also, SPRi can be used as a better throughput platform at instances where the electrochemical methods cannot measure more than a single sample at a time.

1.7 Measuring ultra-low levels of nucleotide biomarkers using quartz crystal microbalance and SPR microarray imaging methods: a comparative analysis (Chapter 4)

1.7.1 Approach and novelty

Circulating serum nucleotide biomarkers are useful indicators for early diagnosis of various deadly diseases. In particular, miRNA-21 (miRNA-21) has been found to be relevant to infectious diseases, such as viral and bacterial infections, as well as non-infectious diseases such as

cardiovascular disorders and cancer. A combination of mass sensor and SPRi methods that utilize the same assay chemistry on gold are useful detection with quantitative insights. In this work, we compared detection performances of a quartz crystal microbalance (QCM), which is a mass sensor, with that of a SPRi microarray for an oligonucleotide mimic of the miRNA-21 biomarker (Figure 5).[39]

A surface immobilized capture oligonucleotide probe was designed and custom synthesized to hybridize with the target oligonucleotide (i.e., the miRNA-21 mimic) to facilitate selective detection. The direct method of forming a self-assembled monolayer of capture probes on the gold surface eliminated the need for additional surface functionalization steps. Gold nanoparticles (Au NPs, 50 nm) were conjugated with the target oligonucleotide to increase the detection sensitivity by adding more mass on the surface on the QCM sensor as well as enhancing the plasmonic signals in an SPRi microarray. To assess the selectivity of the capture probes towards the target oligonucleotide, an Au NP-linked control oligonucleotide containing five base-pair mismatches to the target oligonucleotide was used. Additionally, sample recovery studies were performed to analyze the serum matrix effect.

1.7.2 Outcomes and significance

We achieved detection limits of 28 and 47 fM for the target oligonucleotide by the QCM and SPRi microarray approaches, respectively. Although the QCM was more sensitive and had a lower detection limit, it was throughput limited. The microarray approach offered better throughput for analysis of up to 16 samples, thus the analysis of sample and controls in a single experiment using a dual channel microfluidic system was possible.

The combination of QCM with SPRi can be practically significant as it is useful for quantitative characterization and assay step optimization before applying for a high-throughput platform. We confirmed that the designed assay was selective for the target oligonucleotide and did not show

signals for the control base mismatch oligonucleotide. According to the sample recovery studies (> 90%), there was a negligible interference from the serum matrix up to 25% in buffer. QCM studies revealed the effectiveness of conjugating Au NPs with the target oligonucleotides to increase the sensitivity of the detection signal by about three times. The strategy discussed above opens up an avenue in developing a SPRi-based multiplexed platform to measure multiple biomarkers in clinical matrices.

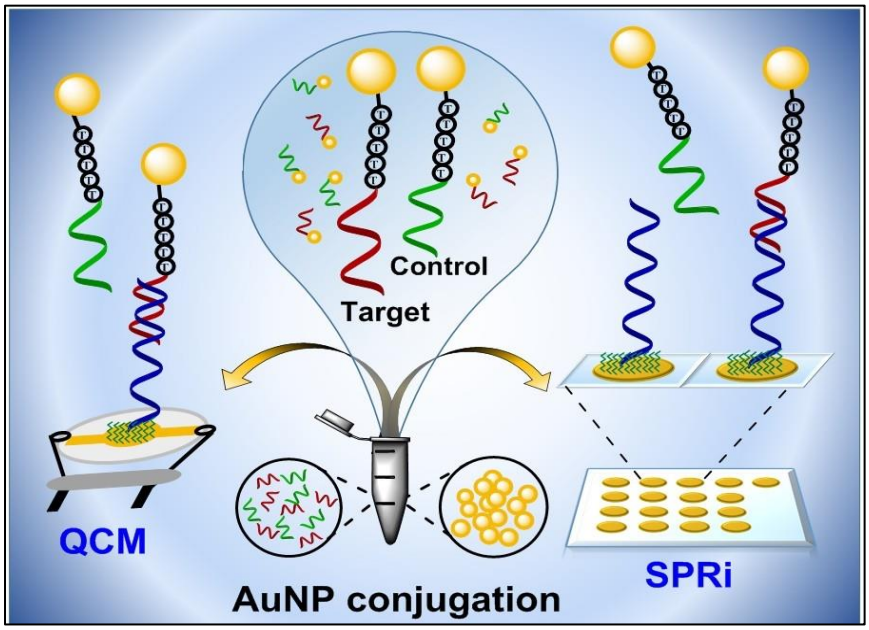

Figure 5. The QCM and SPRi sensors for selective detection of oligonucleotides of miRNA-21 mimic (Target) from a sequence containing five mismatches (Control) with AuNPs-based signal amplification.

1.8 Multiplexed surface plasmon assay for serum proteins and micro-ribonucleic acids: signal amplification by bimetallic Fe_3O_4@Au nanoparticles (Chapter 5)

1.8.1 Approach and Novelty

Highly expressed circulating protein and miRNA markers play a significant role in indicating critical health conditions and measuring them together in one assay platform offers the advantages of increasing the prediction rates and reduction of false positive diagnoses. We recently expanded

our existing dual channel SPRi microfluidic system into a four-channel system to develop a multiplexed assay to simultaneously measure four circulating cancer biomarkers (two proteins: IL-6 and IL-8, and two miRNAs: miRNA-21 and miRNA-155) in human serum (Figure 6).[40] The SPRi microarray uniquely employed citrate-stabilized bimetallic iron-gold bimetallic core/shell nanoparticles (Fe_3O_4@Au NPs) as signal amplification labels covalently linked with secondary detection molecules. Various bimetallic NPs have been built by combining the beneficial properties of two metals and have been employed in biosensing applications.[41] In particular, the Fe_3O_4@Au NPs offered the distinctive benefits of easy conjugation and magnetic separation of desired compounds for subsequent detection in the assay.[42] The plasmonic properties of the gold shell were useful for amplifying the SPR detection signals.[43] SPRi allowed the real-time monitoring of the binding events of the protein and miRNA biomarkers to their surface receptors. Multiplexing was useful to directly assay the two protein markers by a sandwich immunoassay and the two serum miRNA markers by a double hybridization assay in a serum sample.

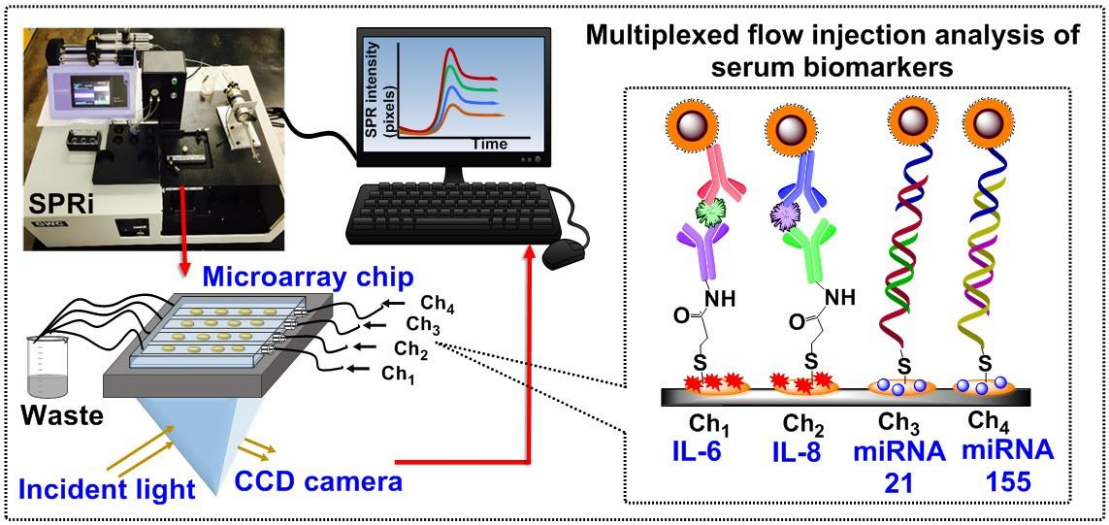

Figure 6. Bimetallic Fe3O4@Au core/shell nanoparticles enhanced multiplexed SPRi bioassay to measure four serum cancer biomarkers.

1.8.2 Outcomes and significance

The Fe_3O_4@Au (105 nm) NPs exhibited 13-times higher plasmon signal intensities than that of only Fe_3O_4 NPs (100 nm) and 6-times greater signals than Au only NPs (100 nm). The magnetic feature of Fe_3O_4@Au NPs was useful for convenient separation of the detection probes that were covalently linked (binding efficiency > 70%). The plasmon enhancing features of Fe_3O_4@Au NPs aided in amplifying the SPRi signal output for analyte markers while minimizing the non-specific signals arising from the serum matrix. The detection limits achieved for the markers were in the pM to sub-pM concentration range.

In 10% serum, the dynamic range of detection for the proteins was from pM to nM (~10^4 orders of magnitude), and for the miRNAs, the dynamic range was from fM to nM (~10^6 orders of magnitude). The binding constants determined from Langmuir-type binding kinetics was from µM to nM range, which provided evidence of strong affinities between the analyte biomarkers and their receptor molecules on the designed sensor surface. This feature is vital in understanding the degree of interaction of the chosen receptors with the target analytes in bioassays. Further, this SPRi array has the potential to be adopted as a tool for analysis of other biomarkers present in clinical samples.

1.9 Conclusions and future directions

In summary, this chapter mainly attempted on discussing various electrochemical and SPRi assay methodologies developed recently to measure biomarkers in complex matrices, and the contributions of the research presented in this dissertation have added new knowledge on combining electrochemical and SPRi methods to determine quality check parameters in devising clinical biosensors with high sensitivity and selectivity. Up to date, scientists have been working tirelessly to advance the field of sensors by developing many impressive electrochemical and SPR based biosensor technologies and have disseminated their findings through a plethora of research publications. However, so far, only a handful of electrochemical biosensors have reached the

commercialization stage. A similar trend can be observed with the reported superior SPR diagnostic assays for biomarker measurement that have still not made it to a clinical setting. Of course, it should be noted that significant research efforts are needed to increase the efficiency, robustness and reproducibility of bioassay designs, and applicability for a large number of samples in order to translate them from laboratory bench into practically implementable methods.

With the increasing population suffering from numerous types of deadly diseases, advanced biosensor technologies are critical for early-diagnosis and prognosis, in order to commence suitable therapeutic regimes in a timely manner. In particular, the advantages of electrochemical sensor technologies and nanotechnology can be combined to develop potential miniaturized devices for personalized continuous biomarker measurements. Future developments in embroidered electrochemical sensors, contact-lens based sensors, sweat sensors and edible biosensors would shift the diagnostic world to a new paradigm. Similarly, besides the biosensing feature, the ability to determine binding insights of various biomolecule interactions by SPRi can be utilized in selecting appropriate surface designs and biorecognition elements for a wide range of biosensors. In parallel to electrochemical techniques, SPR is expected to transform to a user friendly technology by appropriate tuning of the portability and interfacial sensing features. The outlook for electrochemical and SPR research certainly remains positive and many breakthroughs are realizable with continuous explorations.

1.10 References

1. Myers, M.J., Smith, E.R., and Turfle, P.G., Biomarkers in Veterinary Medicine. Annual Review of Animal Biosciences, 2017, 5, 65-87.
2. Ronkainen, N.J., Halsall, H.B., and Heineman, W.R., Electrochemical biosensors. Chemical Society Reviews, 2010, 39, 1747-1763.
3. Abdulbari, H.A., and Basheer, E.A., Electrochemical Biosensors: Electrode Development, Materials, Design, and Fabrication. ChemBioEng Reviews, 2017, 4, 92-105.
4. Guo, X., Surface plasmon resonance based biosensor technique: a review. Journal of Biophotonics, 2012, 5, 483-501.
5. Masson, J.F., Surface plasmon resonance clinical biosensors for medical diagnostics. ACS Sensors, 2017, 2, 16-30.
6. Perumal, V., and Hashim, U., Advances in biosensors: Principle, architecture and applications. Journal of Applied Biomedicine, 2014, 12, 1-15.
7. Xiao, F., Wang, L., and Duan, H., Nanomaterial based electrochemical sensors for in vitro detection of small molecule metabolites. Biotechnology Advances, 2016, 34, 234-249.
8. Singh, J., Roychoudhury, A., Srivastava, M., Solanki, P.R., Lee, D.W., Lee, S.H., and Malhotra, B.D., A dual enzyme functionalized nanostructured thulium oxide based interface for biomedical application. Nanoscale, 2014, 6, 1195-1208.
9. Soldatkin, O., Nazarova, A., Krisanova, N., Borysov, A., Kucherenko, D., Kucherenko, I., Pozdnyakova, N., Soldatkin, A., and Borisova, T., Monitoring of the velocity of high-affinity glutamate uptake by isolated brain nerve terminals using amperometric glutamate biosensor. Talanta, 2015, 135, 67-74.
10. Hughes, G., Pemberton, R.M., Fielden, P.R. and Hart, J.P., Development of a novel reagentless, screen-printed amperometric biosensor based on glutamate dehydrogenase and

NAD+, integrated with multi-walled carbon nanotubes for the determination of glutamate in food and clinical applications. Sensors and Actuators B: Chemical, 2015, 216, 614-621.

11. Reuillard, B., Le Goff, A., and Cosnier, S., Polypyrrolic bipyridine bis (phenantrolinequinone) Ru (II) complex/carbon nanotube composites for nad-dependent enzyme immobilization and wiring. Analytical Chemistry, 2014, 86, 4409-4415.
12. Mohammadi, F., Vesali-Naseh, M., Khodadadi, A.A. and Mortazavi, Y., A Comparison of a Nanostructured Enzymeless Au/Fe_2O_3/MWCNTs/GCE Electrode and a GOx Modified One in Electrocatalytic Detection of Glucose. Electroanalysis, 2018, (doi.org/10.1002/elan.201800164)
13. Premaratne, G., Farias, S. and Krishnan, S., Pyrenyl carbon nanostructures for ultrasensitive measurements of formaldehyde in urine. Analytica Chimica Acta, 2017, 970, 23-29.
14. Krishnan, S., and Armstrong, F.A., Order-of-magnitude enhancement of an enzymatic hydrogen-air fuel cell based on pyrenyl carbon nanostructures. Chemical Science, 2012, 3, 1015-1023.
15. Singh, V., and Krishnan, S., Voltammetric immunosensor assembled on carbon-pyrenyl nanostructures for clinical diagnosis of type of diabetes. Analytical Chemistry, 2015, 87, 2648-2654.
16. Niroula, J., Premaratne, G., Shojaee, S.A., Lucca, D.A., and Krishnan, S., Combined covalent and noncovalent carboxylation of carbon nanotubes for sensitivity enhancement of clinical immunosensors. Chemical Communications, 2016, 52, 13039-13042.
17. Ma, B., Shatsky, M., Wolfson, H.J., and Nussinov, R., Multiple diverse ligands binding at a single protein site: A matter of pre-existing populations. Protein Science, 2002, 11, 184-197.
18. Tang, Z., and Ma, Z., Multiple functional strategies for amplifying sensitivity of amperometric immunoassay for tumor markers: A review. Biosensors and Bioelectronics, 2017, 98, 100-112.

19. Dutta, G., and Lillehoj, P.B., An ultrasensitive enzyme-free electrochemical immunosensor based on redox cycling amplification using methylene blue. Analyst, 2017, 142, 3492-3499.
20. Akanda, M.R., and Ju, H., Ferritin-Triggered Redox Cycling for Highly Sensitive Electrochemical Immunosensing of Protein. Analytical Chemistry. 2018, 90 , 8028–8034.
21. Wang, H., and Ma, Z., A cascade reaction signal-amplified amperometric immunosensor platform for ultrasensitive detection of tumour marker. Sensors and Actuators B: Chemical, 2018, 254, 642-647.
22. Carvajal, S., Fera, S.N., Jones, A.L., Baldo, T.A., Mosa, I.M., Rusling, J.F., and Krause, C.E., Disposable InkJet-Printed Electrochemical Platform for Detection of Clinically Relevant HER-2 Breast Cancer Biomarker. Biosensors and Bioelectronics, 2018, 104, 158-162.
23. Khetani, S., Ozhukil Kollath, V., Kundra, V., Nguyen, M.D., Debert, C., Sen, A., Karan, K., and Sanati-Nezhad, A., bPolyethylenimine Modified Graphene-Oxide Electrochemical Immunosensor for the Detection of Glial Fibrillary Acidic Protein in Central Nervous System Injury. ACS Sensors, 2018, 3, 844-851.
24. Singh, V., and Krishnan, S., Voltammetric immunosensor assembled on carbon-pyrenyl nanostructures for clinical diagnosis of type of diabetes. Analytical Chemistry, 2015, 87, 2648-2654.
25. Niroula, J., Premaratne, G., Shojaee, S.A., Lucca, D.A., and Krishnan, S., Combined covalent and noncovalent carboxylation of carbon nanotubes for sensitivity enhancement of clinical immunosensors. Chemical Communications, 2016, 52, 13039-13042.
26. Premaratne, G., Niroula, J., Patel, M. K., Zhong, W., Suib, S.L., Kalkan, A.K., and Krishnan, S., Electrochemical and Surface Plasmon Correlation of Serum Autoantibody Immunoassay with Binding Insights: Graphenyl vs. Mercapto-Monolayer Surface, 2018, In revision.
27. Chiu, N.F., Huang, T.Y., Lai, H.C., and Liu, K.C., Graphene oxide-based SPR biosensor chip for immunoassay applications. Nanoscale Research Letters, 2014, 9, 445.

28. Patil, A.V., Fernandes, F.B., Bueno, P.R., and Davis, J.J., Graphene-based protein biomarker detection. Bioanalysis, 2015, 7, 725-742.
29. Wang, Y., Zhang, Y., Wu, D., Ma, H., Pang, X., Fan, D., Wei, Q., and Du, B., Ultrasensitive label-free electrochemical immunosensor based on multifunctionalized graphene nanocomposites for the detection of alpha fetoprotein. Scientific Reports, 2017, 7, 42361.
30. Luna, D.M., Avelino, K.Y., Cordeiro, M.T., Andrade, C.A., and Oliveira, M.D., Electrochemical immunosensor for dengue virus serotypes based on 4-mercaptobenzoic acid modified gold nanoparticles on self-assembled cysteine monolayers. Sensors and Actuators B: Chemical, 2015, 220, 565-572.
31. Singh, V., and Krishnan, S., An electrochemical mass sensor for diagnosing diabetes in human serum. Analyst, 2014, 139, 724-728.
32. Krishnan, S., Mani, V., Wasalathanthri, D., Kumar, C.V., and Rusling, J.F., Attomolar detection of a cancer biomarker protein in serum by surface plasmon resonance using superparamagnetic particle labels. Angewandte Chemie International Edition, 2011, 50, 1175-1178.
33. Hinman, S.S., McKeating, K.S., and Cheng, Q., Surface Plasmon Resonance: Material and Interface Design for Universal Accessibility. Analytical Chemistry, 2017, 90, 19-39.
34. Fasoli, J.B., and Corn, R.M., Surface enzyme chemistries for ultrasensitive microarray biosensing with SPR imaging. Langmuir, 2015, 31, 9527-9536.
35. Sankiewicz, A., Romanowicz, L., Pyc, M., Hermanowicz, A., and Gorodkiewicz, E., SPR imaging biosensor for the quantitation of fibronectin concentration in blood samples. Journal of Pharmaceutical and Biomedical Analysis, 2018, 150, 1-8.
36. Hu, F., Xu, J., and Chen, Y., Surface Plasmon Resonance Imaging Detection of Sub-femtomolar MicroRNA. Analytical Chemistry, 2017, 89, 10071-10077.

37. Hendriks, J., Stojanovic, I., Schasfoort, R.B., Saris, D.B., and Karperien, M., Nanoparticle Enhancement Cascade for Sensitive Multiplex Measurements of Biomarkers in Complex Fluids with Surface Plasmon Resonance Imaging. Analytical Chemistry, 2018, 90, 6563-6571.
38. Castiello, F.R., and Tabrizian, M., Multiplex Surface Plasmon Resonance Imaging-Based Biosensor for Human Pancreatic Islets Hormones Quantification. Analytical Chemistry, 2018, 90, 3132-3139.
39. Premaratne, G., Al Mubarak, Z.H., Senavirathna, L., Liu, L,. and Krishnan, S., Measuring ultra-low levels of nucleotide biomarkers using quartz crystal microbalance and SPR microarray imaging methods: A comparative analysis. Sensors and Actuators B: Chemical, 2017, 253, 368-375.
40. Premaratne, G., Dharmaratne, A.C., Al Mubarak, Z.H., and Krishnan, S., Multiplexed surface plasmon assay for serum proteins and microRNAs: signal amplification by bimetallic Fe_3O_4@Au nanoparticles. 2018, *submitted.*
41. Srinoi, P., Chen, Y.T., Vittur, V., Marquez, M.D., and Lee, T.R., Bimetallic Nanoparticles: Enhanced Magnetic and Optical Properties for Emerging Biological Applications. 2018, (doi:10.20944/preprints201804.0104.v1)
42. Pham, T.T.H., Cao, C., and Sim, S.J., Application of citrate-stabilized gold-coated ferric oxide composite nanoparticles for biological separations. Journal of Magnetism and Magnetic Materials, 2008, 320, 2049-2055.
43. Jain, P.K., Xiao, Y., Walsworth, R., and Cohen, A.E., Surface plasmon resonance enhanced magneto-optics (SuPREMO): Faraday rotation enhancement in gold-coated iron oxide nanocrystals. Nano Letters, 2009, 9, 1644-165.

CHAPTER 2

PYRENYL CARBON NANOSTRUCTURES FOR ULTRASENSITIVE MEASUREMENTS OF FORMALDEHYDE IN URINE

2.1 Introduction

Biomarkers are molecular indicators that play a crucial role in the diagnosis, prognosis, and theranostics of diseases such as cancer.[1] As a result, bioanalytical methods that allow sensitive and selective measurements of biomarkers are significant for clinical applications and therapeutics development. In view of diagnostic challenges, the molecular size of a biomarker present in complex body fluid matrices inversely affects the detection sensitivity. This is because small molecules do not yield measurable assay signal changes compared to large biomolecules. Additionally, dilution of samples to minimize clinical matrix effects can further lower the biomarker concentration and its detection. False-positive signals, tedious extraction procedures of analytes from the matrices, simplicity of the assay and detection protocol, and selectivity are other related problems.

Despite the issues described, nanotechnology-based optical and electrochemical methods have allowed detection of large proteins, receptors, antibodies, DNA, and RNA biomarkers at clinically relevant pM to aM concentrations in body fluids.[2] However, development of such analytical assays with simplicity, selectivity, sensitivity, and low-cost for detecting small-molecule markers of

Adapted from G. Premaratne, S. Farias, and S. Krishnan, Pyrenyl carbon nanostructures for ultrasensitive measurements of formaldehyde in urine, *Analytica Chimica Acta*, **2017**, *970*, 23 –29 with permission from Elsevier.

cancer and other diseases non-invasively remains to be a significant challenge. In particular, bioanalytical methods for detection of ultra-low ppb levels of formaldehyde (HCHO) in a complex clinical matrix (e.g., plasma, serum, urine) suffer by interferences from non-analyte components present in the matrix (non-specific signals), poor detection capability, and issues of enzyme instability and loss of enzyme activity. Furthermore, non-invasive detection of biomarker levels is advantageous for routine diagnosis of these diseases at an early stage as it eliminates painful invasive procedures (e.g., biopsy, bronchoscopy), which are known to cause tissue and organ damage.[3] Moreover, we can eliminate minimally invasive procedures, such as drawing of blood from patients for analysis.[4] In this study, we demonstrate for the first time the design of pyrenyl carbon nanostructure modified electrodes for formaldehyde dehydrogenase (FDH) immobilization and electrochemical quantitation of HCHO in a urine matrix with a 6 ppb detection limit.

Aldehydes, including HCHO, have received considerable attention as a key class of volatile organic compound markers that exhibit toxic effects in humans, and are suggested to be relevant for cancer and neural diseases.[5-8] Many techniques have been developed to detect HCHO, including spectrophotometric,[9] electrochemical,[10,11] optical,[12] electronic,[13] and colorimetric[14] methods. Sensitive detection of urine HCHO by chromatography-mass spectrometry methods is known. However, these methods involve expensive instrumentation, and time consuming laborious sample preparation, measurement, and analysis steps.[5] In contrast, electrochemical methods are straightforward and cost effective.[15,16] In particular, electrochemical enzymatic amperometric biosensors offer the advantages of direct and quick detection of analytes with simplicity. By appropriate design of surface strategies, high sensitivity, robustness, and excellent reproducibility can be attained.

FDH (~ 170 kDa), an enzyme of the oxidoreductase family,[17,18] is a homotetrameric enzyme containing 398 amino acids per subunit. Ali *et al.* developed a biosensor made from NAD^+ and glutathione-dependent recombinant FDH immobilized on the surface of a $Si/SiO_2/Si_3N_4$ structure.[11]

A mediator-based amperometric biosensor was constructed on disks of woven graphite gauze coated with NAD^+ and glutathione-independent FDH from *Hyphomicrobium zavarzinii* strain ZV 58.[19] Demkiv *et al.* modified platinized graphite electrodes with NAD^+ and glutathione-dependent FDH isolated from a genetically engineered strain *H. polymorpha.* In that study, electron transfer between the enzyme and the electrode was established using low molecular weight redox mediators or positively charged cathodic electrodeposition paints modified with Os-bis-*N,N*-(2,2'-bipyridyl)-chloride ($[Os(bpy)_2Cl]$).[20] FDH from *Pseudomonas* sp. immobilized on mesoporous silica materials[21] and multiwalled carbon nanotube-modified screen printed electrodes[22] for HCHO detection in buffer solution have been developed.

Herein, we report for the first-time 1-pyrenebutyric acid (PBA) pi-pi stacked with carboxylated multiwalled carbon nanotubes (MWNTs) on the surface of the gold screen printed electrodes (AuSPEs) for covalent FDH immobilization offering highly sensitive and selective ultra-low detection HCHO concentration in a 10-times buffer diluted urine. We combined here the –COOH groups of MWNTs with the non-covalently attached PBA because this combination approach, discovered by us recently, offered 3-fold improved sensitivity for a serum insulin immunosensor compared to the use of only carboxylated MWNTs.[23] HCHO was quantitated using a quinone compound (Q: 1, 2-naphthaquinone-4-sulfonic acid sodium salt) as an electron transfer mediator to obtain electrochemical signals in proportion to HCHO concentration. To our knowledge, this is the first report of a pyrenyl carbon nanostructure based enzymatic bioelectrode for urine HCHO quantitation.

2.2 Experimental

2.2.1 Materials and chemicals

Gold screen printed electrodes (AuSPEs) with a three-electrode cell configuration integrated on a ceramic substrate (Model: 250 BT, 4 mm diameter Au working electrode, Pt counter electrode, and

Ag pseudo reference electrode) were purchased from DropSens Inc. (Spain). Multiwalled carboxylic acid functionalized carbon nanotubes (MWNTs, > 8% carboxylic acid functionalized, avg. diam. 9.5 nm, length 1.5 μm), β-nicotinamide adenine dinucleotide sodium salt (NAD^+), FDH from *Pseudomonas* sp., PBA, 1,2-naphthaquinone-4-sulfonic acid sodium salt (Q), HCHO solution (36.5 – 38% in water), 1-ethyl-3-[3-dimethylaminopropyl]carbodiimide hydrochloride (EDC), *N*-hydroxysuccinimide (NHS), and formaldehyde-2,4-dinitrophenylhydrazone analytical standard (HCHO-DNPH) for liquid chromatography were purchased from Sigma and were used as received. Vivaspin 6 ultrafiltration cartridges (molecular weight cut off: 3 kDa, GE Healthcare, Little Chalfont, Buckinghamshire, UK) were used for filtration of urine. All aqueous reagents were prepared in deionized water (DI H_2O) using a Milli-DI water purification system (Millipore Ltd., Billerica, Massachusetts, USA). All other chemicals were high purity analytical grade.

2.2.2 Instrumentation

Amperometric measurements were performed at room temperature (23 ^oC) using a CHI 6017E electrochemical workstation coupled to a faraday cage and a picoamp booster (Austin, TX, USA). The flow-cell was connected to a syringe pump system (New Era Pump Systems Inc., NY, USA) and a sample injector valve (Rheodyne model 9725i PEEK injector, IDEX Health & Science LLC, CA, USA). The sample loop volume was 200 μL. Spectroscopic characterizations of the bioelectrode fabrication steps were carried out using Fourier transform infrared spectroscopy (FTIR, Thermo Scientific Nicolet iS50) in the attenuated total reflectance (ATR) mode. The bioelectrodes were placed directly on the ATR diamond crystal and 32 scans were taken and averaged to obtain a good signal-to-noise ratio. In addition, Raman spectroscopy (Nicolet NXR FT-Raman module, Nd:YVO_4 laser, 1064 nm, 0.2 W, resolution 4 cm^{-1}) and electrochemical impedance spectroscopy (Interface 1000 potentiostat/galvanostat/ZRA, Gamry instruments, Warminster, PA) were used for the characterization of the designed bioelectrode. Liquid chromatography-mass spectrometry (LC-MS) with an electrospray ionization source (Shimadzu

LCMS-2010EV) was used for identification of HCHO-DNPH derivative, methanal 2,4-dinitrophenylhydrazone.

2.2.3 Surface modification of AuSPE

Briefly, on the surface of disposable AuSPEs, 5 µL dispersions of 2 mg mL^{-1} MWNTs in dimethylformamide (DMF) were added to cover the entire AuSPE surface and allowed to dry at room temperature. The electrodes were washed well with deionized H_2O and dried under nitrogen prior to adding 3 µL of 3 mg mL^{-1} PBA solution in DMF. The electrodes were kept in a cold and moist environment for 1 h to allow the formation of strong pi-pi interactions between MWNTs and PBA. The electrodes then were washed well with deionized H_2O and dried under nitrogen.

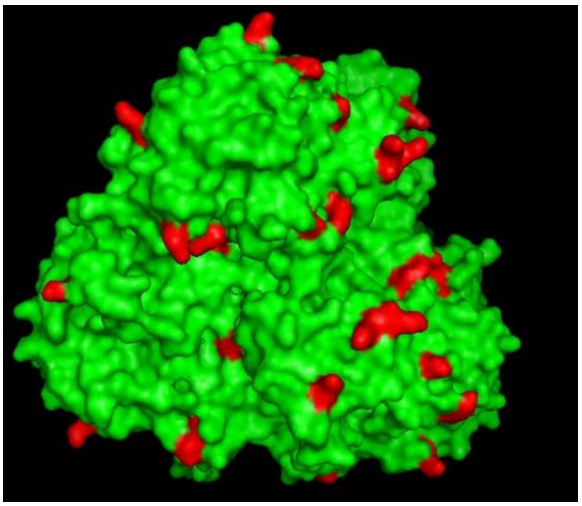

Figure 1. Representation of the crystal structure of FDH from Pseudomonas aeruginosa (PDB 4JLW). The surface lysine (Lys) residues available for covalent attachment to surface carboxylic acid groups of PBA and MWNT are highlighted in red.

FDH enzyme was covalently linked *via* its free surface lysine residues (PDB: 4JLW, Figure 1) to the –COOH terminal groups of both the MWNT and PBA assembly by the established carbodiimide chemistry.[24] To carry out this reaction, MWNT/PBA-modified AuSPEs were treated with 5 µL solution of a freshly prepared mixture containing 0.35 M EDC and 0.1 M NHS for 15 min to activate the surface carboxylic acid groups of MWNTs and PBA into lysine (Lys) amine reactive *N*-succinimidyl esters. The electrodes were then washed with deionized H_2O to remove unreacted reagents and subsequently treated with 5 µL of 200 µg/mL FDH solution prepared in

phosphate buffered saline (PBS) and incubated for 1 h to obtain covalently linked FDH films. The prepared electrodes were used immediately for measuring HCHO in urine.

2.2.4 Chronoamperometric detection of formaldehyde in urine samples

Urine samples were collected from a healthy male adult volunteer in a 50 mL sterile polyethylene vial. Samples were then immediately vortexed and divided into 10 mL aliquots and stored at -20 ^{o}C for up to 30 days to avoid any storage loss. Before use, the frozen samples were thawed at room temperature. Prior to spiking with formaldehyde, a 6 mL aliquot of the urine sample was subjected to centrifugal filtration using Vivaspin-6 cartridges at a speed of 4000 rpm for 30 min at room temperature.[25] Filtered urine samples were diluted 10-times in PBS. Various concentrations of formaldehyde were spiked in the 10-times diluted urine and were used for analysis.

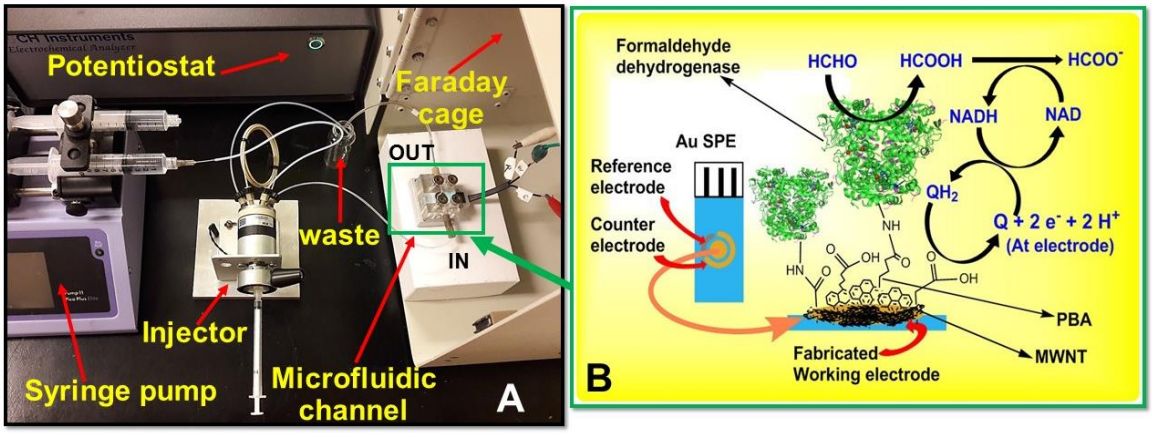

Figure 2. (A) Schematic of the microfluidics system used in this study. (B) Fabrication steps of the AuSPEs with FDH and the reaction sequence for catalyzing HCHO and detection by flow injection or stirred solution amperometry.

FDH-immobilized AuSPE/MWNT/PBA electrodes were attached to an in-house designed flow cell that was connected to a syringe pump and a sample injector (Figure 2A). The running buffer was made up of PBS containing 5 mM NAD^+ and 1 mM Q. Various concentrations of HCHO prepared in 10-times diluted urine in PBS were injected *via* a manual injector valve onto the bioelectrode surface. Real-time measurements of the oxidation currents of QH_2 formed from NADH as a result

of FDH catalyzed HCHO oxidation were performed at an applied constant potential of + 0.35 V (Figure 2B).[21,26] The current versus HCHO concentration was plotted and the resulting curve was fit by the Michaelis-Menten non-linear regression equation available with the K-graph software used.

2.3 Results and Discussion

2.3.1 FTIR characterization of the modified electrodes

Figure 3 shows the baseline corrected FTIR-ATR results for the modified bioelectrode surface that confirmed the covalent immobilization of FDH onto the –COOH groups of AuSPE/MWNT/PBA electrodes. A strong vibrational peak at 1714 cm^{-1} indicated the presence of carbonyl stretching from the –COOH groups of MWNTs. Pi-pi stacking of PBA with MWNTs red shifted the C=O stretching vibration to 1698 cm^{-1}, which has been attributed to the partial electron transfer from PBA to MWNT resulting in a relatively weaker C-C bond strength in the MWNT/PBA complex than the MWNT alone.[27] Additionally, a broad peak at 3136 cm^{-1} for the O-H stretching was observed.[28] Following covalent FDH attachment *via* coupling of Lys amines with surface carbodiimide activated (EDC/NHS) -COOH groups of PBA and MWNTs forming amide bonds, typical amide-I and amide-II bands from the peptide backbone of FDH were observed at 1683 and 1603 cm^{-1}, respectively.[29] The disappearance of the prior O-H stretching and appearance of a new broad band at 3472 cm^{-1} arising from N-H stretching of FDH indicated amide bond formation and thus the enzyme immobilization. Furthermore, it is possible that a partial non-covalent adsorption of the FDH onto the MWNT/PBA surface cannot be ruled out. Despite this, based on the observed FTIR spectral changes of the surface carboxylic acids the covalent FDH attachment is evident.

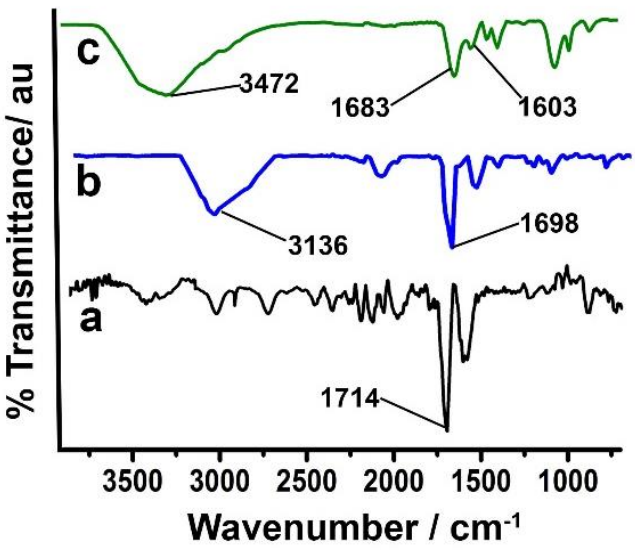

Figure 3. FTIR spectra of AuSPE coated with (a) carboxylated MWNTs, (b) after PBA stacking, and (c) after covalent immobilization of FDH

2.3.2 Raman characterization of the nano-bioelectrode fabrication steps

Figure 4 represents the Raman spectra of AuSPE coated with MWNT, after pi-pi stacking with PBA, and subsequent covalent immobilization of FDH by Lys amine-carboxylic acid coupling chemistry using EDC/NHS reagents. The Raman spectrum of carboxylated MWNT-coated AuSPEs showed the characteristics D, G, and G′ bands at 1316, 1594, and 2614 cm^{-1}, respectively.[30,31] Decrease in frequency of these bands to 1304, 1585, and 2605 cm^{-1}, respectively, as a result of pi-pi stacking of the PBA molecules was observed.[32,33]

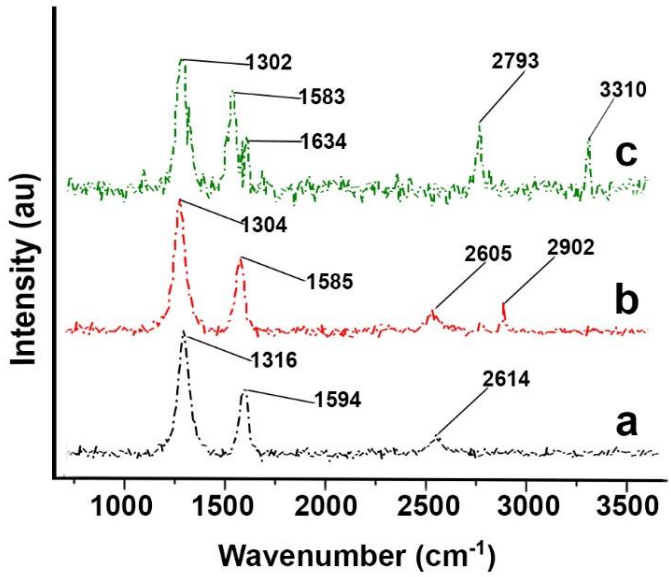

Figure 4. Raman spectra of AuSPEs coated with (a) Carboxylated MWNTs, (b) after PBA stacking, and (c) after covalent immobilization of FDH.

Another band at 2902 cm^{-1} can be attributed to the aromatic C-H groups arising from PBA molecules. A further shift in the G band and the appearance of new peaks at 1634 and 3310 cm^{-1} indicated the presence of amide groups confirming the covalent attachment of FDH onto MWNT/PBA assembly on AuSPEs.

2.3.3 Electrochemical impedance spectroscopy characterization

Figure 5 represents the Nyquist plots corresponding to the faradaic impedance measurements for each step of the FDH bioelectrode construction in an aqueous solution containing 0.1 M KCl and a mixture of 10 mM of each potassium ferricyanide and potassium ferrocyanide redox probe $[Fe(CN)_6^{3-/4-}]$. The Randles equivalent circuit model was used to fit the experimental impedance spectra to estimate the charge transfer resistance (R_{ct}) similar to our prior report.[34] MWNT/PBA modification of AuSPE surface decreased the R_{ct} and thus made the surface more conductive (inset of Figure 5 for clarity). This is suitable for facilitating interfacial charge transport. Subsequent covalent attachment of the FDH enzyme onto the EDC/NHS activated surface –COOH groups of PBA and MWNT increased the R_{ct} value, as would be expected for non-conductive enzyme molecules.

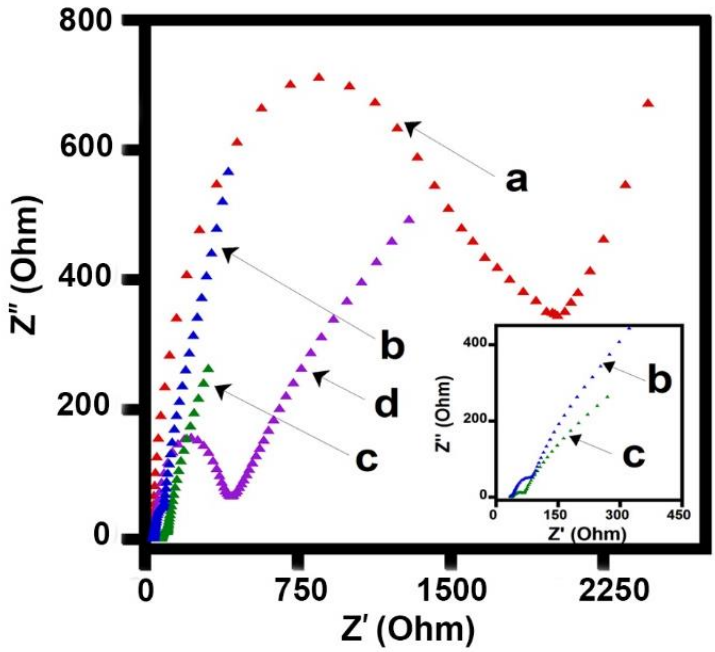

Figure 5. Faradaic impedance spectroscopic measurements of Rct values in an aqueous solution containing 0.1 M KCl and 10 mM of Fe(CN)63-/4- for stepwise modification of (a) AuSPE (1792 Ω), (b) after dry-coating of MWNT (154 Ω), (c) after pi-pi stacking of PBA (67 Ω), and (d) after covalent immobilization of FDH (410 Ω). Experimental conditions: 0.2 V vs Ag/AgCl, amplitude 10 mV, and frequency range 0.1-100 kHz.

2.3.4 Amperometric response for the stirred vs flow injection analysis

The enzyme fabricated SPEs were assessed for HCHO oxidation in a 10-times diluted urine matrix. The ability of the enzyme to function well in the urine matrix was very important, and thus adequate NAD+ cofactor (5 mM) was supplied. Ten times dilution of urine provided the optimum performance of the FDH bioelectrode with minimal non-specific signals in the working potential region as discussed below. FDH-catalyzed detection of HCHO was performed according to the reaction sequence shown in Figure 2B. Q was used as the electron transfer mediator to transfer electrons to the electrode from NADH formed in solution as a result of the FDH-catalyzed HCHO oxidation.[21] This in turn regenerates NAD^+ to receive subsequent protons upon HCHO oxidation.

Upon dilution of the urine matrix, an increase in the amperometric current was observed (Figure 6, tested using 1 ppm of HCHO for method optimization). This could be attributed to the reduction in high salt concentration and other interfering agents for the optimum performance of the sensor and/or the FDH enzyme.[35] Diluting the urine samples more than ten times did not significantly increase the amperometric response. Hence, ten times dilution of the urine was selected for further studies.

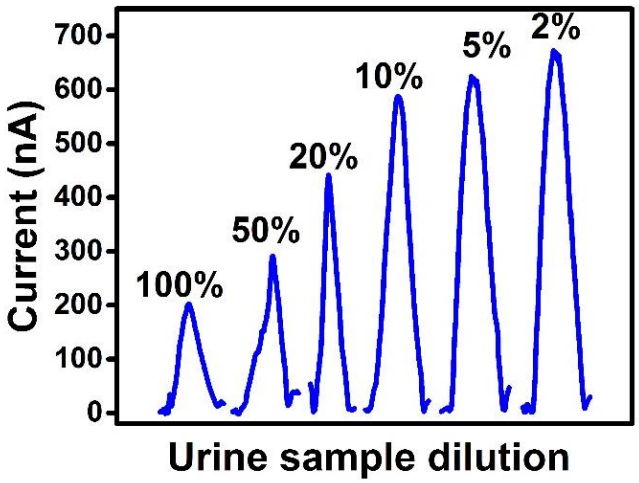

Figure 6. Amperometric responses (after subtraction of signals for control urine sample with no spiked HCHO) of flow injection analysis of 1 ppm HCHO at various dilutions of urine samples with PBS (pH 7.4) containing 5 mM NAD+ and 1 mM Q delivered a flow rate of 100 µL min^{-1} at an applied potential of + 0.35 V at 23 ºC.

Figure 7A-a shows the increase in currents of the bioelectrode in stirred solutions containing various concentrations of HCHO from ppb to ppm levels in 10-times diluted urine matrix at an optimum solution stirring rate of 150 rpm. Linearity of the currents vs. concentration of HCHO was observed between 100 ppb and 16 ppm (initial range in Fig. 7A-b), which is a wide dynamic range useful for clinical assay of such markers. A deviation from the linearity was observed at higher concentrations of HCHO (i.e., > 16 ppm) and followed typical electrochemical Michaelis-Menten enzyme kinetics (Fig. 7A-b).[36] The estimated apparent Michaelis-Menten constant (K_M^{app}) using KaleidaGraph software (version 4.1) was 19.9 ± 4.6 ppm. The limit of detection (LOD) (the

signal at three times the standard deviation of the mean of the HCHO unspiked control urine sample[37]) of the described stirred solution-based HCHO detection was 73 ppb. To examine improvements on the detection sensitivity of the stirred solution method by facilitating better mass transport of HCHO and other assay reagents, we used flow injection analysis.[38]

The cofactor and electron transfer mediator containing solution mixture (5 mM NAD^+ and 1 mM Q in PBS, pH 7.4) was delivered at an optimum flow rate of 100 µL min^{-1} onto the FDH bioelectrode surface using a syringe pump. Various concentrations of HCHO spiked in 10-times diluted urine in PBS (pH 7.4) then were injected via a manual injection valve, and the resulting oxidation currents were measured (Figure 7B-a).

The sensitivity of HCHO detection was only moderately enhanced (by two times) in the flow injection method compared to the stirred solution (calculated from the slopes of the initial linear range in Fig. 7A-b and 7B-b). A possible reason could be that the HCHO and mediators used are small molecules. As a result the mass transport by convection (stirring vs fluid flow) does not seem to be greatly different in view of sensitivity (i.e., the slope of response plots covering the linear range of HCHO concentrations). Nevertheless, the flow injection analysis significantly decreased the LOD to 6 ppb, which is 12-fold smaller than the stirred-solution method. This is likely because diffusion of reactants to products (cofactor, urine matrix, and mediator reaching the electrode and the product diffusing away) becomes much more prominent at the lowest concentration corresponding to the LOD. As a result, the flow injection method for the designed bioelectrode seems to be better than the stirred-solution analysis in facilitating effective electronic communication of the low levels of urine HCHO with the surface of the AuSPE/MWNT/PBA enzyme electrode.

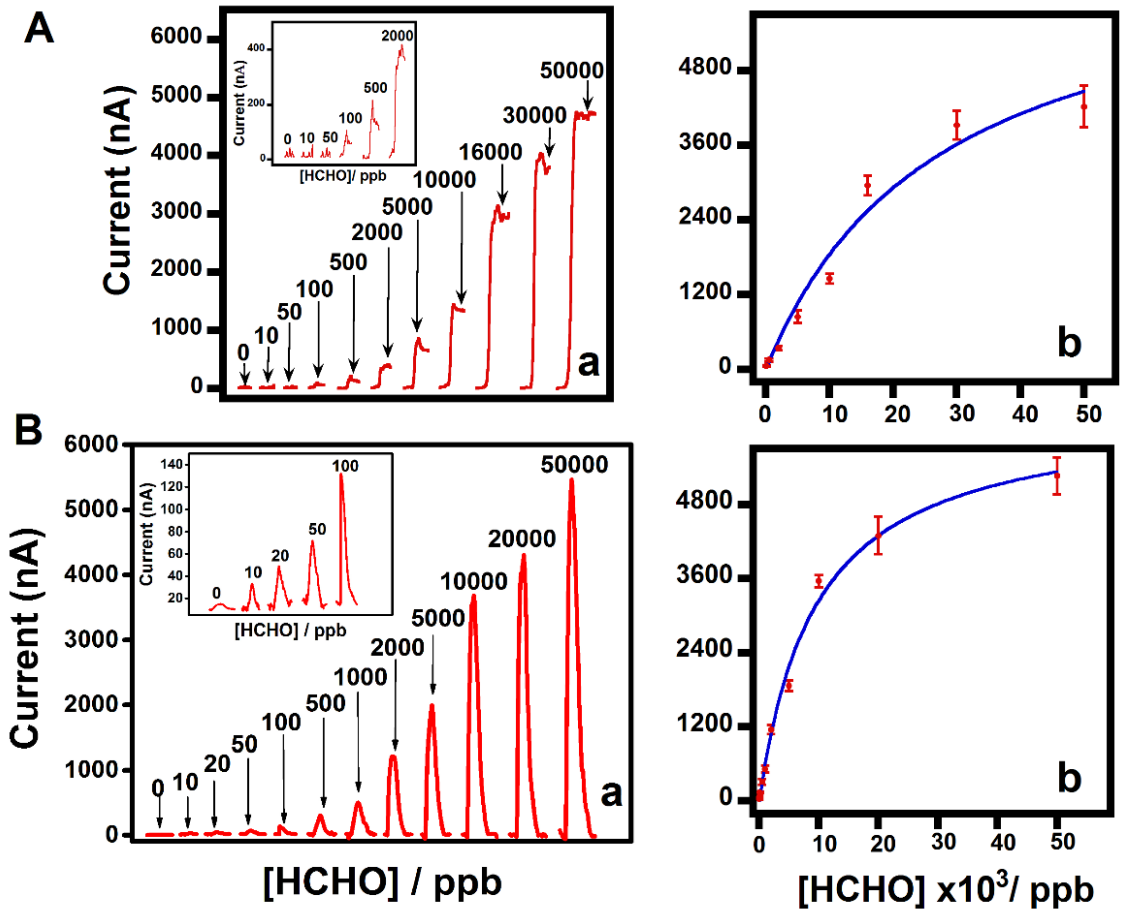

Figure 7. (A) Stirred solution method: (a) Amperometric responses of the AuSPE/MWNT/PBA-FDH bioelectrode for various concentrations of HCHO in 10-times diluted urine in PBS, pH 7.4, containing 5 mM NAD^+ and 1 mM Q at an applied potential of + 0.35 V at 23 ºC and a constant stirring of solution using a magnetic stirrer at 150 rpm. Inset shows the enlarged view for lower HCHO concentrations. **(b)** Michaelis-Menten fit of the designed bioelectrode in oxidizing HCHO. **(B) Flow injection analysis: (a)** Amperometric responses for the AuSPE/MWNT/PBA enzyme bioelectrode upon injection of various concentrations of HCHO at a flow rate of 100 µL min^{-1}. Inset shows the enlarged view for lower HCHO concentrations. **(b)** The corresponding Michaelis-Menten fit of the experimental data.

Reported studies based on chromatography and mass spectrometry methods identified increased levels of HCHO present in the urine samples of patients with dementia and bladder cancer conditions compared to healthy individuals. Thus, the obtained LOD of the FDH bioelectrode for measuring HCHO in urine meets the reported clinically relevant range [e.g., bladder cancer (> 85

ppb),[39] dementia (> 5.8 ppm),[8a] and early stages of cognitive impairments in older adults (> 330 ppb)[8b]]. The lower LOD illustrates the advantages of flow injection analysis in improving analyte mass transport and minimizing noise levels, resulting in an enhanced signal-to-noise ratio and thus an improved detection limit. The linear dynamic range of our flow analysis for HCHO in 10-times diluted urine was from 10 ppb to 10 ppm.

The relationship between current signal and HCHO concentration was fit by the Michaelis-Menten non-linear regression curve (Figure 7A-b and 7B-b) using KaleidaGraph software (version 4.1). The estimated K_M^{app} of flow injection method was 9.6 ± 1.2 ppm, which is better than the stirred-solution method and likely due to enhanced substrate mass transport facilitating kinetically faster steady state conditions in the flow system. The observed difference between the affinity constants was calculated to be significant at 95% confidence level. Previously reported K_M values of HCHO solution bioassays were 5.4 ppm for FDH from genetically engineered *H. polymorpha*,[20] 7.5–8.7 ppm for a homologous enzyme from *Candida boidinii*,[40] 6.3 ppm for FDH from *H. polymorpha*,[41] and 12.9 ppm for FDH from *Pichia pastoris.*[42] Results indicate that the K_M^{app} values obtained in the present work are comparable with the reported bioassays.

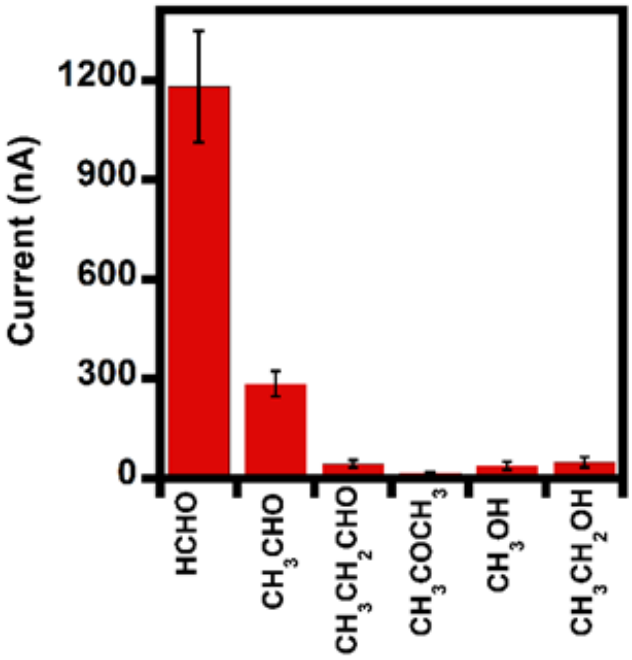

Figure 8. Selectivity of the designed AuSPE/MWNT/PBA-FDH bioelectrode for HCHO over other similar analytes in stirred solutions. Current signals for 5 ppm of analytes (x-axis) in 10-times diluted urine solutions in PBS are shown.

The presented FDH bioelectrode design offers sensitivity, ultra-low clinically useful LOD, and simplicity, but it is also essential to meet selectivity criteria for clinical diagnosis of small-molecule disease markers. Figure 8 depicts the current signals for HCHO with two immediate aldehyde homologues and with acetone and two types of alcohol. The current responses confirm the high selectivity for HCHO, with ~ 25% cross-reactivity for acetaldehyde (CH_3CHO) and negligible cross-reactivity for propanaldehyde, acetone, methanol, and ethanol. The moderate cross-reactivity for acetaldehyde suggests that the substrate binding pocket of the FDH enzyme has a slight affinity for this immediate homologue of HCHO that does not vary significantly in size.

2.3.5 LC-MS confirmation of the presence of HCHO in the prepared urine samples by derivatization with DNPH

The presence of spiked HCHO in the urine samples was independently verified by LC-MS (Figure 9).[43-45] In brief, to a vial containing 5 mL of HCHO (5 ppm) in 10-times diluted urine, 2 mL of 1 mg mL^{-1} DNPH and 0.2 mL of 5 N H_3PO_4 were added and the solution was thoroughly mixed. The solution was allowed to stand for 30 min for DNPH derivatization of HCHO forming a Schiff base (methanal 2,4-dinitrophenylhydrazone derivative: HCHO-DNPH)). The samples were then filtered using a 0.22 µm PTFE syringe membrane filter before analysis by LC-MS. A Premier C18, 3 µ 100 x 4.6 mm column (Schimadzu) was used with a mobile phase composition of acetonitrile:water mixture (60:40) and a flow rate of 0.3 mL min^{-1}. The LC peaks were detected using a photodiode array detector operating in the wavelength range of 200-800 nm with a selected wavelength of 354 nm that corresponds to the HCHO-DNPH derivative. Mass spectra were recorded in the *m/z* range of 100 to 350 Da using an electrospray ionization operated in negative ion mode. As shown in Figure 9-A(a), the HCHO-DNPH derivative appears around 5.8 min in agreement with the peak of the derivative standard [Figure 9-A(d)]. The peak at 4.5 min corresponds to the underivatized DNPH in the sample [Figure 9-A(a and b)]. It can be noted that the blank urine sample does not

interfere with the derivative detection [Figure 9-A(c)]. The 209 *m/z* corresponds to the HCHO-DNPH derivative that is in agreement with the prior report in literature (Figure 9-B).[45]

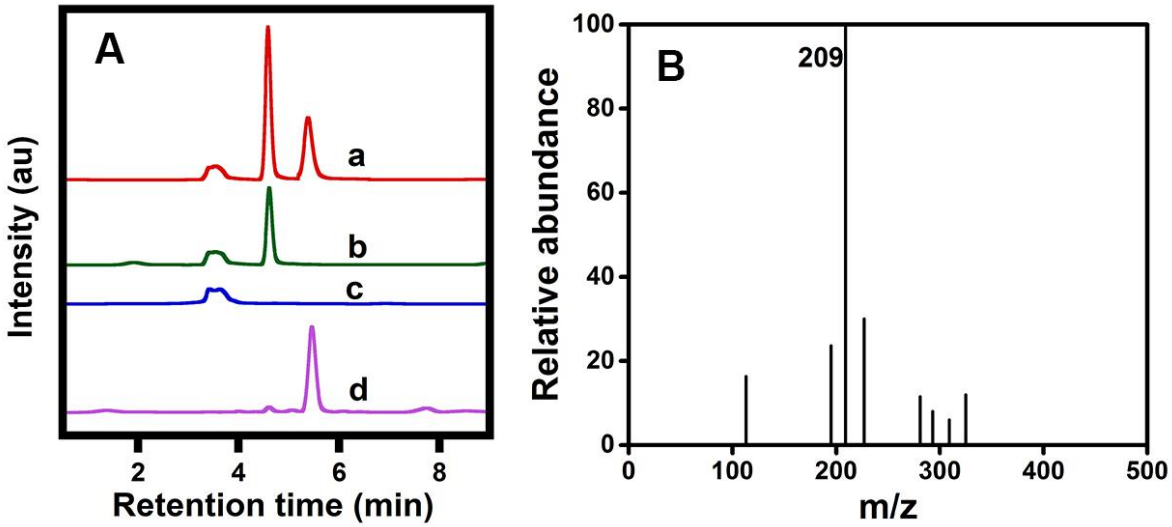

Figure 9. (A) LC-MS analysis of the presence of HCHO (5 ppm) in the prepared urine samples (10-times diluted) by DNPH derivatization method. Separation of (a) DNPH derivatized urine sample containing HCHO (5 ppm), (b) diluted urine sample with only DNPH, (c) diluted urine sample alone, and (d) standard DNPH-HCHO derivative (20 ppm). (B) MS analysis showing the 209 Da peak for the formed DNPH-HCHO derivative in the urine sample.

2.3.6 Stability and selectivity of the electrode

The fabricated FDH bioelectrodes were tested for film stability in PBS (pH 7.4 at 23 ^{o}C) for 40 h by non-faradaic impedance spectroscopy at an applied constant frequency of 5 Hz (Figure 10).[46] A stable impedance magnitude of 232 Ω was noted for more than 40 h. It is worth mentioning that AuSPEs are intended to be for disposable use and hence the observed stability upon continuous soaking of the modified, FDH attached SPE surface in a buffer solution is reasonably good.

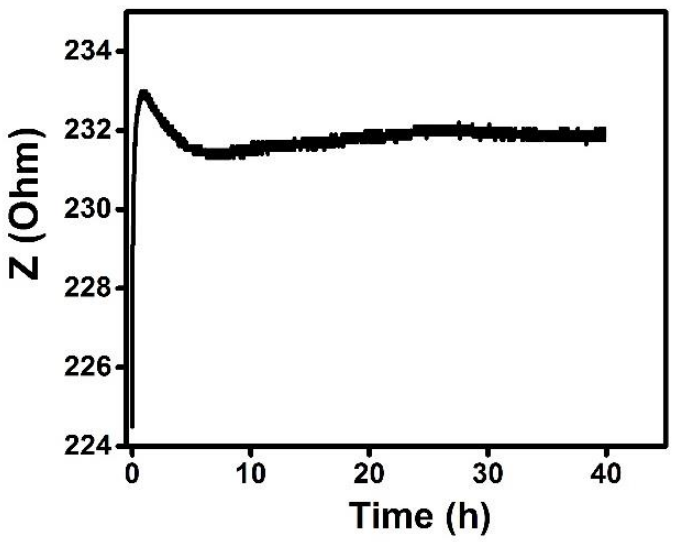

Figure 10. Film stability assessment of the designed AuSPE/MWNT/ PBA-FDH bioelectrode for 40 h using electrochemical non-faradaic impedance spectroscopy at an applied frequency of 5 Hz in PBS, pH 7.4, room temperature (23 ^{o}C).

Excluding the MWNT/PBA surface modification of AuSPEs, the bioelectrode design only required one step for FDH immobilization and subsequent detection and quantitation of HCHO in 10-times diluted urine. The various sample matrices used in the literature for HCHO and the reported linear dynamic range, detection limit, sensitivity, and bioelectrode stability are presented in Table 1. This comparison shows better performance of the pyrenyl-cabon nanostructure bioelectrode than simple buffer solution-based HCHO quantitation methods.

Table 1. Comparison of the present MWNT/PBA-FDH nano-bioelectrode with relevant reported studies.

Sensor type	**Construction material**	**Sensing method**	**Sensing element**	**Matrix**	**Linear dynamic range/ Sensitivity/ Detection limit**	**Ref.**
Planar electrochemical transducers	Potentiometric sensor – Si_3N_4-ISFET Conductometric and amperometric sensor – gold interdigitated electrodes vacuum deposited with sintered aluminum oxide	Potentiometry, conductometry, and amperomety	Alcohol oxidase from *Hansenula polymorpha*	10 mM Phosphate buffer (pH 7.7)	150 – 9000 ppm	47
Enzyme biosensor	$Si/SiO_2/Si_3N_4$ structure as physical transducers	Capacitance	NAD^+ and glutathione-dependent recombinant formaldehyde dehydrogenase	2.5 mM Borate buffer (pH 8.40)	0.3 – 600 ppm Sensitivity 31 mV/ decade Detection limit 0.3 ppm	11
Amperometric enzyme sensor	Disks of woven graphite gauze	Amperometry	NAD^+ and glutathione-independent formaldehyde dehydrogenase from	0.1 M KCl, 80mM KH_2PO_4 (pH 8.0)	0.5 – 15 ppm Sensitivity 0.39 µA/ppm	19

			Hyphomicrobium zavarzinii strain ZV 58			
Amperometric biosensor	Platinized graphite electrode modified with low-molecular free-diffusing redox mediators or positively charged cathodic electrodeposition paints modified with Os-bis-N,N-(2,2'-bipyridil)-chloride ($[Os(bpy)_2Cl]$)	Amperometry	NAD^+ and glutathione-dependent formaldehyde dehydrogenase isolated from a gene-engineered strain of the methylotrophic yeast *Hansenula polymorpha*	20 mM Phosphate buffer (pH 8.2)	0.3 – 3 ppm Sensitivity 358 $Am^{-2}\,M^{-1}$ Detection limit 90 ppb	20
Electrochemical biosensor	Glassy carbon electrode containing a membrane constructed with mesoporous silica materials	Amperometry	Formaldehyde dehydrogenase from *Pseudomonas* sp.	Phosphate buffer (pH 7.4)	30 ppb – 30 ppm Detection limit 36 ppb	21
Electrochemical biosensor	Screen-printed carbon electrode modified with MWCNT	Amperometry	Formaldehyde dehydrogenase from *Pseudomonas putida*	PBS (based on *in situ* released HCHO from a prodrug treated cancer cells in PBS)	3 ppb – 3 ppm Detection limit 300 ppb	22

Electrochemical biosensor	Screen printed gold electrodes modified with MWNT/PBA-FDH via the –COOH groups of both MWNT and PBA	Amperometry	Formaldehyde dehydrogenase from *Pseudomonas* sp.	10-times diluted urine (in PBS, pH 7.4)	**Stirred solution analysis:** 100 ppb - 16 ppm Sensitivity (based on the initial linear range, Fig. 3) 174 nA/ppm Detection limit 73 ppb **Flow injection analysis:** 10 ppb – 10 ppm Sensitivity (based on the initial linear range, Fig. 3) 342 nA/ppm Detection limit 6 ppb	**This work**

2.4 Conclusions

Ther results presented confirm the analytical detection features of pyrenyl carbon nanostructure-modified FDH bioelectrode for sensitive and selective quantitation of urine HCHO related to abnormal conditions that are known to result in elevated urine HCHO. The presented approach provides a viable nano-bioelectrode design for non-invasive detection of small-molecule markers for cancer and other diseases at clinically relevant ultra-low levels in complex matrices. Combining the current method with measurements of other biomarkers and assays of significance is expected to allow successful diagnostic outcome of an abnormal condition. By appropriate immobilization of marker specific-receptor molecules or enzymes coupled with a detection probe or mechanism, the proposed methodology is expected to allow broader applicability for quantitative measurement of any other small-molecule markers with selectivity.

Author contribution

Gayan Premaratne performed the majority of experiments, data analysis and drafted the manuscript. Sabrina Farias performed the repeats of the amperometric experiments. Dr. Sadagopan Krishnan provided thoughtful insights into this research project and reviewed the manuscript.

2.5 References

1. a) J.A. Ludwig, J.N. Weinstein, Biomarkers in cancer staging, prognosis and treatment selection, Nat. Rev. Cancer. 5 (2005) 845-856; b A. de Gramont, S. Watson, L.M. Ellis, J. Rodón, J. Tabernero, A. de Gramont, S.R. Hamilton, Pragmatic issues in biomarker evaluation for targeted therapies in cancer, Nat. Rev. Clin. Oncol. 12 (2015) 197-212; c) M. Kalia, Biomarkers for personalized oncology: recent advances and future challenges, Metabolism 64 (2015) S16-S21; d) S. Surinova, L. Radová, M. Choi, J. Srovnal, H. Brenner, O. Vitek, M. Hajdúch, R. Aebersold, Non-invasive prognostic protein biomarker signatures associated with colorectal cancer, EMBO Mol. Med. 7 (2015) 1153-1165.
2. G. Shipp, Ultrasensitive measurement of protein and nucleic acid biomarkers for earlier disease detection and more effective therapies, Biotechnol. Healthc. 3 (2006) 35-40; b) M. Swierczewska, G. Liu, S. Lee, X. Chen, High-sensitivity nanosensors for biomarker detection, Chem. Soc. Rev. 41 (2012) 2641-2655; c) S.B. Nimse, M.D. Sonawane, K. S. Song, T. Kim, Biomarker detection technologies and future directions, Analyst 141 (2016) 740-755; d) J.F. Rusling, C.V. Kumar, J.S. Gutkind and V. Patel, Measurement of biomarker proteins for point-of-care early detection and monitoring of cancer, Analyst 135 (2010) 2496-2511; e) S. Krishnan, V. Mani, D. Wasalathanthri, C.V. Kumar, J.F. Rusling, Attomolar detection of a cancer biomarker protein in serum by surface plasmon resonance using superparamagnetic particle labels, Angew. Chem. Int. Ed. 50 (2011) 1175 –1178; f) V. Singh, S. Krishnan, Voltammetric immunosensor assembled on carbon-pyrenyl nanostructures for clinical diagnosis of type of diabetes, Anal. Chem., 87 (2015) 2648-2654.
3. Y.S.L. Cheng, T. Rees, J. Wright, A review of research on salivary biomarkers for oral cancer detec-tion, Clin. Transl. Med. 3 (2014) 1.
4. a) H. M. Heneghan, N. Miller, A.J. Lowery, K. J. Sweeney, J. Newell, M.J. Kerin, Circulating microRNAs as novel minimally invasive biomarkers for breast cancer, Ann. Surg. 251 (2010)

499-505; b) J. Wang, J. Chen, P. Chang, A. LeBlanc, D. Li, J.L. Abbruzzesse, M. L. Frazier, A.M. Killary and S. Sen, MicroRNAs in plasma of pancreatic ductal adenocarcinoma patients as novel blood-based biomarkers of disease, Cancer Prev. Res. 2 (2009) 807-813; c) N. Goossens, S. Nakagawa, X. Sun and Y. Hoshida, Cancer biomarker discovery and validation, Transl. Cancer Res. 4 (2015) 256.

5. J. Zhang, R. Sun, Y. Chen, K. Tan, H. Wei, L. Yin, Y. Pu, Small Molecule Metabolite Biomarker Candidates in Urine from Mice Exposed to Formaldehyde, Int. J. Mol. Sci. 15 (2014) 16458-16468.A. Songur, O.A. Ozen, M. Sarsilmaz, The toxic effects of formaldehyde on the nervous system. In Reviews of environmental contamination and toxicology, Springer New York, (2010) 105-118.
6. A. Songur, O.A. Ozen, M. Sarsilmaz, The toxic effects of formaldehyde on the nervous system. In Reviews of environmental contamination and toxicology, Springer New York, (2010) 105-118.
7. a) B. Buszewski, M. Kęsy, T. Ligor, A. Amann, Human exhaled air analytics: biomarkers of diseases, Biomed. Chrom. 21 (2007) 553-566; b) P. Fuchs, C. Loeseken, J. K. Schubert, W. Miekisch, Breath gas aldehydes as biomarkers of lung cancer, Int. J. Cancer. 126 (2010) 2663-2670; c) A. Wehinger, A. Schmid, S. Mechtcheriakov, M. Ledochowski, C. Grabmer, G.A. Gastl, A. Amann, Lung cancer detection by proton transfer reaction mass-spectrometric analysis of human breath gas, Int. J. Mass Spectrom. 265 (2007) 49-59.
8. a) Z. Tong, J. Zhang, W. Luo, W. Wang, F. Li, H. Li, H. Luo, J. Lu, J. Zhou, Y. Wan, R. He, Urine formaldehyde level is inversely correlated to mini mental state examination scores in senile dementia, Neurobiol. Aging 32 (2011) 31-41; b) J. Yu, T. Su, T. Zhou, Y. He, J. Lu, J. Li, R. He, Uric formaldehyde levels are negatively correlated with cognitive abilities in healthy older adults, Neurosci. Bull. 30 (2014) 172-184; c) Z.H. Hao, W.J. Li, M. Li, R. He, Correlation of urine formaldehyde levels and mini mental state examination scores in Alzheimer's disease, Chin. J. Gerontol. 31 (2011) 3442-3444.

9. Y.Y. Maruo, J. Nakamura, M. Uchiyama, M. Higuchi, K. Izumi, Development of formaldehyde sensing element using porous glass impregnated with Schiff's reagent, Sens. Actuators B Chem. 129 (2008) 544-550.
10. a) F. Vianello, A. Stefani, M.L. Di Paolo, A. Lui, B. Margesin, M. Zen, M. Scarpa, G. Soncini, Potentiometric detection of formaldeyde in air by an aldehyde de-hydrogenase FET Sens. Actuators B. 37 (1996) 49–54; b) R. L. Bunde, E. J. Jarvi and J. J. Rosebtreter, A piezoelectric method for monitoring formaldehyde induced cross-link formation between poly-lysine and poly-deoxyguanosine, Talanta 51 (2000) 159–171; c) T. Kida, N. Morinaga, S. Kishi, K.M. An, K.W. Sim, B.Y. Chae, J.K. Kim, B.K. Bong-Ki Ryu, K. Shimanoe, Electrochemical detection of volatile organic compounds using a Na3Zr2Si2PO12/Bi2Cu0.1V0.9O5.35 heterojunction device, Electrochim. Acta. 56 (2011) 7484-7490; d) W. Vastarella, R. Nicastri, Enzyme/semiconductor nanoclusters combined systems for novel amperometric biosensors, Talanta, 66 (2005) 627-633; e) T. Chen, Q. Liu, Z. Zhou, Y. Wang, The fabrication and gas-sensing characteristics of the formaldehyde gas sensors with high sensitivity, Sens. Actuators B Chem. 131 (2008) 301-305; f) J. Wang, P. Zhang, J.Q. Qi, P.J. Yao, Silicon-based micro-gas sensors for detecting formaldehyde, Sens. Actuators B Chem. 136 (2009) 399-404; g) H. Dai, L. Gong, G. Xu, X. Li, S. Zhang, Y. Lin, B. Zeng, C. Yang, G. Chen, An electrochemical impedimetric sensor based on biomimetic electrospun nanofibers for formaldehyde, Analyst 140 (2015) 582-589.
11. M.B. Ali, M. Gonchar, G. Gayda, S. Paryzhak, M. Maaref, N. Jaffrezic-Renault, Y. Korpan, Formaldehyde-sensitive sensor based on recombinant formaldehyde dehydrogenase using capacitance versus voltage measurements. Biosens. Bioelectron. 22 (2007) 2790-2795.
12. a) S. Friedfeld, M. Fraser, D. Lancaster, D. Leleux, D. Rehle, F. Tittel, Field intercomparison of a novel optical sensor for formaldehyde quantification, Geophys. Res. Lett. 27 (2000) 2093–2096; b) H. Kudo, Y. Suzuki, T. Gessei, D. Takahashi, T. Arakawa, K. Mitsubayashi,

Biochemical gas sensor (bio-sniffer) for ultrahigh-sensitive gaseous formaldehyde monitoring, Biosens. Bioelectron. 26 (2010) 854-858.

13. a) J.A. Dirksen, K. Duval, T.A. Ring, NiO thin-film formaldehyde gas sensor, Sens. Actuators B Chem. 80 (2001) 106-115; b) P. Lv, Z.A. Tang, J. Yu, F.T. Zhang, G.F. Wei, Z.X. Huang, Y. Hu, Study on a micro-gas sensor with SnO2–NiO sensitive film for in-door formaldehyde detection, Sens. Actuators B Chem. 132 (2008) 74-80; c) J. Wang, L. Liu, S.Y. Cong, J. Q. Qi, B.K. Xu, An enrichment method to detect low concentration formaldehyde, Sens. Actuators B Chem. 134 (2008) 1010-1015.
14. X. Qin, R. Wang, F. Tsow, E. Forzani, X. Xian and N. Tao, Colorimetric chemical sensing platform for real-time monitoring of indoor formaldehyde. IEEE Sens. J. 15 (2015) 1545-1551.
15. L. Nyholm, Electrochemical techniques for lab-on-a-chip applications, Analyst, 130 (2005) 599-605.
16. O. A. Sadik, A.O. Aluoch, A. Zhou, Status of biomolecular recognition using electrochemical techniques, *Biosens. Bioelectron.* 24 (2009,) 2749-2765.
17. B. Persson, J. Hedlund, H. Jornvall, Medium-and short-chain dehydrogenase/ reductase gene and protein families. Cell. Mol. Life Sci. 65 (2008) 3879.
18. N. Tanaka, Y. Kusakabe, K. Ito, T. Yoshimoto, K.T. Nakamura, Crystal structure of formaldehyde dehydrogenase from *Pseudomonas putida*: the structural origin of the tightly bound cofactor in nicotinoprotein dehydrogenases. J. Mol. Biol. 324 (2002) 519.
19. S. Achmann, M. Hermann, F. Hilbrig, V. Jérôme, M. Hämmerle, R. Freitag, R. Moos, Direct detection of formaldehyde in air by a novel NAD+ and glutathione-independent formaldehyde dehydrogenase-based biosensor, Talanta 75 (2008) 786-791.
20. O. Demkiv, O. Smutok, S. Paryzhak, G. Gayda, Y. Sultanov, D. Guschin, H. Shkil, W. Schuhmann, M. Gonchar, Reagentless amperometric formaldehyde-selective biosensors based on the recombinant yeast formaldehyde dehydrogenase, Talanta 76 (2008) 837-846.

21. T. Shimomura, T. Itoh, T. Sumiya, F. Mizukami, M. Ono, Electrochemical biosensor for the detection of formaldehyde based on enzyme immobilization in mesoporous silica materials, Sens. Actuators B Chem. 135 (2008) 268-275.

22. L. Bareket, A. Rephaeli, G. Berkovitch, A. Nudelman, J. Rishpon, Carbon nanotubes based electrochemical biosensor for detection of formaldehyde released from a cancer cell line treated with formaldehyde releasing anticancer prodrugs, Bioelectrochemistry **77** (2010) 94-99.

23. J. Niroula, G. Premaratne, S. A. Shojaee, D.A. Lucca, S. Krishnan, Combined Covalent and Noncovalent Carboxylations of Carbon Nanotubes for Sensitivity Enhancement of Clinical Immunosensors, Chem. Comm. 52 (2016) 13039-13042.

24. a) S. Krishnan, F.A. Armstrong, Order-of-magnitude enhancement of an enzymatic hydrogen-air fuel cell based on pyrenyl carbon nanostructures, Chem. Sci., 3 (2012) 1015-1023; b) R.A. Kamin, G.S. Wilson, Rotating ring-disk enzyme electrode for biocatalysis kinetic studies and characterization of the immobilized enzyme layer, Anal. Chem. 52 (1980) 1198–1205; c) J.J. Gooding, V.G. Praig, E.A.H. Hall, Platinum-catalyzed enzyme electrodes immobilized on gold using self-assembled layers, Anal. Chem. 70 (1998) 2396-2402.

25. C. E. Baños, M. A Silva, A novel clean-up method for urine analysis of low-molecular mass aldehydes by capillary electrophoresis with laser-induced fluorescence detection, J. Chromatogr. B, 879 (2011) 1412-1418.

26. P. N. Bartlett, R. G. Whitaker, Strategies for the development of amperometric enzyme electrodes, Biosensors 3 (1987) 359-79.

27. V. A. Karachevtsev, S. G. Stepanian, A. Y. Glamazda, M. V. Karachevtsev, V. V. Eremenko, O. S. Lytvyn and L. Adamowicz, Noncovalent interaction of single-walled carbon nanotubes with 1-pyrenebutanoic acid succinimide ester and glucoseoxidase, J. Phys. Chem. C 115 (2011) 21072.

28. S. Majeed, V. Filiz, S. Shishatskiy, J. Wind, C. Abetz, V. Abetz, Pyrene-POSS nanohybrid as a dispersant for carbon nanotubes in solvents of various polarities: its synthesis and application in the preparation of a composite membrane. Nanoscale Res. Lett. 7 (2012) 1.
29. M. Zhang, A. Smith, W. Gorski, Carbon nanotube-chitosan system for electrochemical sensing based on dehydrogenase enzymes, Anal. Chem. 76 (2004) 5045-5050.
30. V. Datsyuk, M. Kalyva, K. Papagelis, J. Parthenios, D. Tasis, A. Siokou, I. Kallitsis, C. Galiotis, Chemical oxidation of multiwalled carbon nanotubes. Carbon 46 (2008) 833-840.
31. M. Zdrojek, W. Gebicki, C. Jastrzebski, T. Melin, A. Huczko, Photoexcitations in fully organic nanocomposites of poly (3-hexylthiophene) and multiwalled carbon nanotubes. In Solid State Phen. 99 (2004) 265-268.
32. Choi, E. Y., Roh, S. C., Kim, C. K. Noncovalent functionalization of multi-walled carbon nanotubes with pyrene-linked nylon66 for high performance nylon66/multi-walled carbon nanotube composites. Carbon, 2014, 72, 160-168.
33. K. S. Prasad, C.Walgama, S. Krishnan, Enhanced electroactivity and substrate affinity of microperoxidase-11 attached to pyrene-linkers π–π stacked on carbon nanostructure electrodes. RSC Adv., 5 (2015) 11845-11849.
34. V. Singh, S. Krishnan, An electrochemical mass sensor for diagnosing diabetes in human serum. Analyst 139 (2014) 724 – 728.
35. M. W. Wood, S. K. Nordone, S. L. Vaden, E. B. Breitschwerdt, Assessment of urine solute and matrix effects on the performance of an enzyme-linked immunosorbent assay for measurement of interleukin-6 in dog urine. J. Vet. Diagn. Invest. 23 (2011) 316-320.
36. S. Krishnan, C. Walgama, Electrocatalytic features of a heme protein attached to polymer-functionalized magnetic nanoparticles, Anal. Chem. 85 (2013) 11420−11426.
37. T. Bryan, X. Luo, P. R. Bueno, J. J. Davis, An optimised electrochemical biosensor for the label-free detection of C-reactive protein in blood, Biosens. Bioelectron. 39 (2013) 94-98.

38. a) J. Lankelma, Z. Nie, E. Carrilho, G. M. Whitesides, Paper-based analytical device for electrochemical flow-injection analysis of glucose in urine, Anal. Chem. 84 (2012) 4147-4152. b) J. Wang, R. Krause, K. Block, M. Musameh, A. Mulchandani, M.J. Schöning, Flow injection amperometric detection of OP nerve agents based on an organophosphorus–hydrolase biosensor detector, Biosens. Bioelectron. 18 (2003) 255-260. c) J.A. Cox, T. Gray, K.R. Kulkarni, Stable modified electrodes for flow-injection amperometry: application to the determination of thiocyanate, Anal. Chem. 60 (1988) 1710-1713.
39. P. Španěl, D. Smith, T. A. Holland, W.A. Singary, J.B. Elder, Analysis of formaldehyde in the headspace of urine from blad-der and prostate cancer patients using selected ion flow tube mass spectrometry. Rapid Commun. Mass Spectrom. 13 (1999) 1354-1359.
40. H. Schutte, J. Flossorf, H. Sahm, M.R. Kula, Immobilized formaldehyde-metabolizing enzymes from Hansenula polymorpha for removal and control of airborne formaldehyde, J. Eur. Biochem. 62 (1976) 151.
41. J.J. Allais, A. Louktibi, J. Baratti, Oxidation of methanol by the yeast, Pichia pastoris, purification and properties of the formaldehyde dehydrogenase, Agric. Biol. Chem. 47 (1983) 1509.
42. R.J.S. Baerends, G.J. Sulter, T.W. Jeffries, J.M. Cregg, M. Veenhuis, Molecular characterization of the Hansenula polymorphaFLD1 gene encoding formaldehyde dehydrogenase, Yeast 19 (2002) 37.
43. Van Leeuwen, S. M.; Hendriksen, L.; Karst, U. Determination of aldehydes and ketones using derivatization with 2, 4-dinitrophenylhydrazine and liquid chromatography–atmospheric pressure photoionization-mass spectrometry. J. Chromatogr. A. 1058 (2004) 107-112.
44. A. Soman, Y. Qiu, Q. C. Li, HPLC-UV method development and validation for the determination of low level formaldehyde in a drug substance. J. Chromatogr. Sci. 46 (2008) 461-465.

45. J. H. Miller, W. P. Gardner, R. R. Gonzalez, UHPLC separation with MS analysis for eight carbonyl compounds in mainstream tobacco smoke. J. Chromatogr. Sci. 48 (2010) 12-17.
46. J. Rickert, W. Göpel, W. Beck, G. Jung, P. Heiduschka, A 'mixed'self-assembled monolayer for an impedimetric immunosensor, Biosens. Bioelectron. 11 (1996) 757-768.
47. Y. Korpan, S. Dzyadevich, V. Arkhipova, A. El'skaya, M. Gonchar, T. Gibson, N. Jaffrezic-Renault, C. Martelet, A. Soldatkin, Enzyme-based electrochemical sensors for formaldehyde detection, Sensor. Mater. 12 (2000) 79-87.

CHAPTER 3

ELECTROCHEMICAL AND SURFACE PLASMON CORRELATION OF SERUM AUTOANTIBODY IMMUNOASSAY WITH BINDING INSIGHTS: GRAPHENYL VS. MERCAPTO-MONOLAYER SURFACE

3.1 Introduction

The design of a reliable and reproducible biosensing assay platform with molecular insights into binding and quantitative nano-bio surface designs is significant for successful diagnostic applications. Serum concentration of autoantibodies has been proposed to associate with the occurrence of type 1 diabetes (T1D).[1,2] T1D is a chronic immune disorder that results from the destruction of β-cell function in the islets of Langerhans, causing deficient insulin production and hyperglycemia.[3] The etiology of T1D is largely unknown, but a combination of genetic predisposition, environmental factors, and a dysregulated immune system is believed to be the cause of the disorder.[4-6] Over recent years, the prevalence of diabetes, in particular T1D has significantly increased from 5% to 10%. This has in turn affected the incidence of associated health complications on a large population of children and adults worldwide.[7,8]

Pociot and Lernmark recently reported that T1D could be characterized by the appearance of β-cell autoantibodies at an early stage, and glutamic acid decarboxylase autoantibody (GADA) is one of them.[9] In the early 1990s, GADA was recognized to interact with a 65-kDa autoantigen known as the glutamic acid decarboxylase-65 (GAD-65).

Later, Urban and coworkers reported the association of GAD-65 and GADA immune complexes in stiff syndrome and T1D.[10] GADA has been recognized as a highly valuable biomarker for the prediction of T1D, thus representing significance for the development of simple and accurate methods for early diagnosis of T1D.

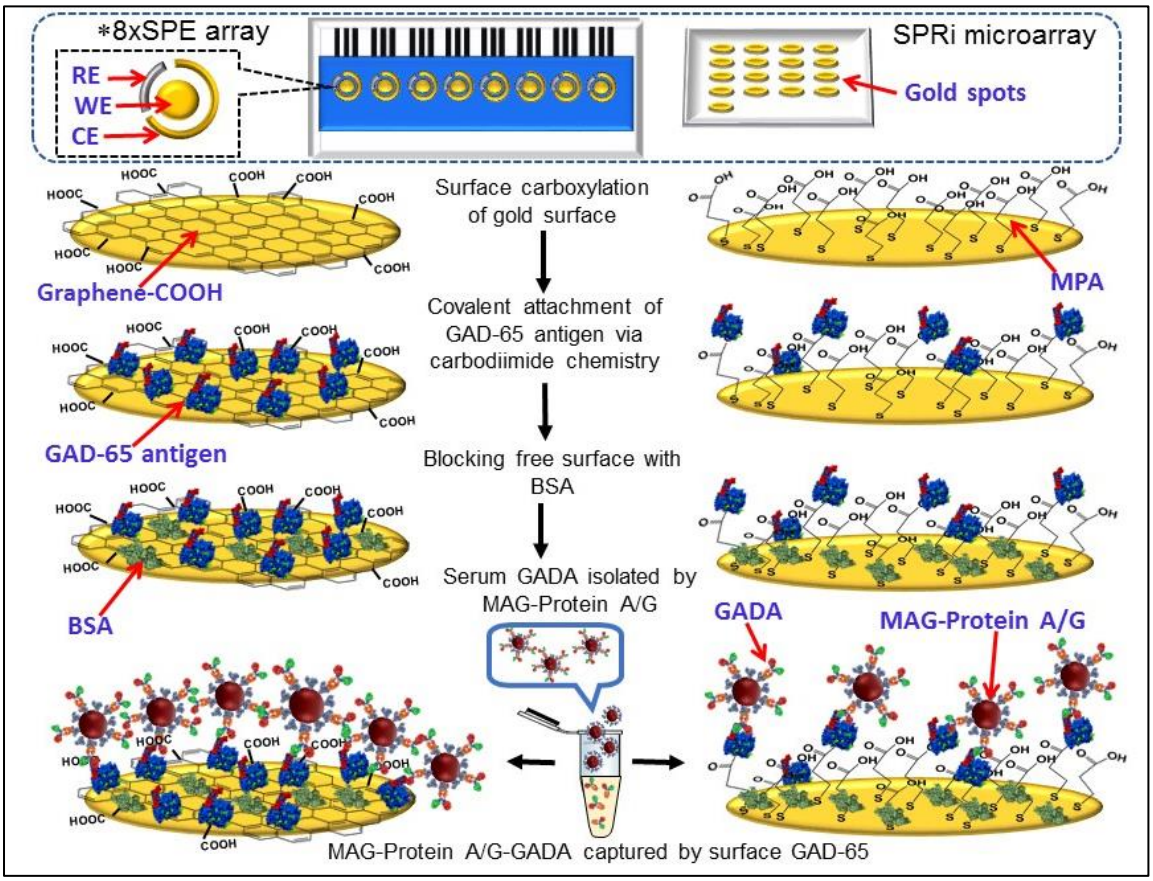

Figure 1. Design of graphenyl and mercapto monolayer based immunosensors for biosensing and binding kinetics analysis. *Three electrode system in the 8xSPE array: gold working electrode (WE) and counter electrode (CE), pseudo Ag-reference electrode (RE).

Over the past two decades, many research groups have demonstrated methods including radioimmunoassay (RIA),[11] enzyme-linked immunosorbent assay (ELISA),[12] chemiluminescent immunoarray (CLIA)[13], and electrochemiluminescence assay[14] for clinical diagnosis of T1D. Here we use an inexpensive ferricyanide reagent to demonstrate the electrochemical detection of GADA, compare the binding constants and analytical assay parameters, and provide quantitative insights into carboxylated graphene and mercapto-monolayer surface modifications (Figure 1).

As a novel class of two-dimensional nanocarbon material, graphene has recently attracted researchers in biomedical sciences for the development of sensitive electrochemical and optical devices.[15-17] The high surface area to volume ratio, electrical conductivity, aqueous dispersibility suitable for screen-printed electrode surfaces, thin structure and apparent biocompatibility of carboxylated graphene makes it a unique carbon nanomaterial for biorecognition events and biosensing applications.[18-20] Although, glucose and insulin biosensors are useful for diabetes management, non-glucose biomarkers are critical for enabling early diabetes prediction in children and adults.[21-23]

To increase detection sensitivity, sensor surface modifications with various nanomaterials and selective isolation of analytes from complex sample matrices (e.g., blood, saliva, urine) by nanomaterials for amplified detection have been demonstrated.[24-29] In particular, magnetic (MAG) beads are unique for the ease of magnetic isolation, separation, and highly sensitive detection of proteins, nucleic acids, and cells due to their high surface area and intrinsic magnetic properties.[30-34] Appropriate designs of the surface of MAG beads with specific capture molecules can be used to separate biomolecules selectively from complex clinical matrices to facilitate ultra-low detection with reduced nonspecific signals.[30,31,35-37] In the present study, we demonstrate that by combining electrochemical immunosensing with surface plasmon resonance (SPR) spectroscopy, we can validate the electrochemical platform, and use the binding constant as a quality control checkpoint for large-scale production of the relatively inexpensive electrochemical sensors.

Furthermore, in this work, a carboxylated graphenyl surface is quantitatively compared with the conventional mercapto-monolayer surface to obtain insights into analytical assay performance. The knowledge gained from the combined sensing and binding assessment is useful for developing reliable and better throughput clinical immunosensors for biomarker based diagnostic assays.

3.2 Experimental

3.2.1 Materials and chemicals

Eight-channel screen-printed gold electrodes (8xSPE) were purchased from DropSens, Spain (Product No. 8x220BT). SPR imaging (SPRi) gold array chips (Spot Ready 16, 1 mm diameter gold spots) were purchased from GWC Technologies (Madison, WI). Carboxylated graphene (graphene-COOH) was purchased from ACS materials (Medford, MA). Glutamic acid decarboxylase-65 antigen (GAD-65) was bought from Creative Diagnostics (Shirley, NY, USA). Monoclonal glutamic acid decarboxylase autoantibody (GADA), bovine serum albumin (BSA, ≥ 98%), aminoferrocene, 3-mercaptopropionic acid (MPA, ≥99%), 1-ethyl-3-[3-(dimethylamino) propyl] carbodiimide (EDC), and *N*-hydroxysuccinimide (NHS) were purchased from Sigma (St. Louis, MO, USA). Normal human serum was purchased from Atlanta Biologicals (Flowery Branch, GA, USA).

Human serum samples were diluted 10-times in phosphate buffered saline (PBS), pH 7.4. Protein A/G coated magnetic beads (MAG-protein A/G, 2 µm, 10 mg mL^{-1}) were purchased from Biotool (Houston, TX, USA). The beads contain 9.3×10^{13} protein A/G molecules/cm^2 (Biotool). All other chemicals used were analytical grade. A NanoOrange Protein Quantitation Kit was purchased from Thermo Fisher Scientific (Waltham, MA, USA). The commercial GADA ELISA kit was purchased from MyBioSource, Inc. (San Diego, CA, USA). The reagents were prepared using ultra-pure water (Invitrogen Corporation, Grand Island, NY, USA). All measurements were carried out at room temperature (23 ˚C).

3.2.2 Instrumentation

Electrochemical impedance spectroscopy (EIS) measurements were performed to characterize the sensor surface modification as well as measure the GADA concentration dependent increase in charge transfer resistance (R_{ct}) for ferricyanide/ferrocyanide redox probe added in solution. For the

EIS, an Interface 1000 potentiostat/galvanostat/ZRA from Gamry Instruments was used (Warminster, PA, USA).

Surface plasmon measurements of GADA-GAD-65 interaction were made using GWC SPR imager-II (Horizon SPR imager model, GWC Technologies, Madison, WI). A light source with an operating wavelength of 800 nm was used. Real-time reflectivity changes followed by imaging of these changes as pixel intensity was completed using a charge-coupled device. The SPR curves were fit for kinetic analysis using TraceDrawer Software (Ridgeview Instruments AB, Vänge, Sweden).

ELISA measurements were performed using a Biotek Synergy H1 Plate Reader based on UV/VIS/Fluorescence quantitation (BioTek Instruments, Inc., Winooski, VT, USA).

Characterization of each step of the surface modification was conducted by scanning electron microscopy (SEM, Model: FEI Quanta 600FE) at an accelerating voltage of 20 kV. The images were acquired using FEIxT Microscope Control Software. Additional characterization of the sensor designs was conducted by Fourier transform infrared spectroscopy (FTIR, Thermo Scientific Nicolet iS50) operated in the attenuated total reflection mode using a diamond crystal.

NanoOrange protein quantitation kit that works based on fluorescence was employed for quantifying the surface immobilized GAD-65 by measuring the difference in GAD-65 concentration in solution before and after the immobilization step (Varian Cary Eclipse Fluorescence Spectrophotometer).

3.2.3 Fabrication of the electrochemical immunosensor

Each gold disk working electrode (geometric area = 0.2 cm^2) of 8xSPE arrays were drop-coated with a 3.5 µL aliquot of a well-dispersed aqueous solution of carboxylated graphene (2.0 mg mL^{-1}). The electrodes were placed in an oven (50 ^oC) for 30 mins in order to dry-coat the graphene

on the gold surface. The electrodes were then washed well with deionized water. For comparison, a conventional monolayer of MPA on 8xSPE arrays was prepared by incubating the working electrodes with 3.5 µL of 2 mg mL^{-1} solution of MPA in ethanol for 4 h in a cold and moist environment. All further assay steps were carried out under ice cold conditions. Carbodiimide chemistry was followed to covalently link the surface lysine groups of GAD-65 (PDB: 2OKK, ~29 surface lysine residues) to the electrode surface via surface carboxyl groups of graphene or a MPA monolayer.[38-40] For this, the 8xSPEs were treated with 4 µL of a freshly prepared solution mixture of EDC (0.35 M) and NHS (0.1 M) in deionized water for 20 min to activate the carboxyl groups to converting them to amine reactive *N*-succinimidyl esters. Following removal of unreacted reagents with deionized water, 3.5 µL of GAD-65 solution (6.5 µg mL^{-1} in PBS) was placed on each electrode of the arrays to covalently link GAD-65 through formation of amide bonds with the activated surface carboxyl groups for a duration of 30 min. After washing the unbound antigens with PBS, the free graphene surface was blocked for 15 min using 3 µL of a 1% BSA solution prepared in PBS. Finally, 3.5 µL of MAG-protein A/G-captured 10% serum GADA samples of various concentrations were added on the electrodes and allowed to incubate for 1 h. The modified immunosensor was rinsed in PBS to remove any unbound molecules and used for electrochemical measurements.

3.2.4 Magnetic bead-protein A/G capturing of autoantibody from 10% human serum (MAG-protein A/G-GADA)

MAG beads functionalized with surface protein A/G molecules offer binding sites with orientation for capturing antibodies from serum. The capturing procedure followed the instructions provided by the manufacturer with slight modifications. In brief, 25 µL of MAG-protein A/G beads were washed twice with 150 µL of phosphate buffered saline (PBS, pH 7.4, 10 mM phosphate, 0.14 M NaCl, 2.7 mM KCl), and separated out using a small piece of magnet after each wash. The beads were then washed twice in 150 µL of binding buffer (50 mM tris, 150 mM NaCl, 0.1% Tween 20,

pH 7.5). Different concentrations of GADA spiked in 10% normal human serum in the binding buffer (250 µL) were added to separate aliquots of MAG-protein A/G beads and rotated in a tube rotor (Fisher Scientific) for 1 h at room temperature. Upon completion of the incubation, the contents were suspended by pipetting in and out for 10 times, and the supernatant was removed immediately from the magnetically separated beads. The beads were washed two times with 300 µL of the binding buffer. Finally, the beads were suspended to a final volume of 200 µL in the binding buffer. The MAG-protein A/G captured serum GADA samples were stored at 4 ^{o}C and used for up to 5 days.

3.2.5 SPRi microarray modification

Prior to use, the SPRi gold array chip was cleaned in piranha solution (3:1 mixture of concentrated H_2SO_4 and 30% H_2O_2 for 10 seconds. Caution: Piranha solution is highly corrosive and a strong oxidizer). First, 0.30 µL of 0.1 mg mL^{-1} of carboxyl-functionalized graphene (graphene-COOH) was dry-coated on each gold spot of the SPRi chip (1 mm diameter) and dried at 50 °C for 30 minutes. The chip was then washed thoroughly with deionized water to remove any unbound material. Following the dry-coating, the immobilization of GAD-65 and BSA blocking steps were similar to that described above for the electrochemical immunoassay. The chip was then mounted in the SPRi instrument to monitor real-time reflectivity changes upon the binding of various concentrations of serum GADA captured onto MAG-protein A/G beads. Once the steady state response was reached, the SPR chip surface was rinsed well with PBS (pH 7.4) to remove any unbound molecules present in the bulk solution and to attain a new baseline signal. Similar SPR measurements were taken for an immunosensor prepared with a self-assembled monolayer of MPA instead of the graphene-COOH modification.

3.2.6 Quantitation of GAD-65 on the immunoassay surface

The amount of GAD-65 bound per electrode was quantified using a NanoOrange protein quantitation kit as follows: A calibration curve was obtained for various concentrations (2 – 10 ng mL^{-1}) of GAD-65 prepared in the NanoOrange working solution provided in the assay kit. The solutions were heated at 95 ^{o}C for 10 min in the dark followed by cooling to room temperature for 20 min before measuring fluorescence intensity. GAD-65 (3.5 µL of 6.5 µg mL^{-1}) was then coated onto each carboxyl activated graphene working electrode for 30 min and washed twice with 5 µL aliquots of PBS. The wash solutions were collected and made up to 2 mL with the NanoOrange working solution. A similar heating and cooling protocol as described above was followed before measuring the fluorescence intensity (excitation at 465 nm and emission at 603 nm). From the difference in fluorescence of free GAD-65 before and after surface immobilization, the amounts of GAD-65 immobilized on the graphene-COOH and MPA surfaces were estimated.

3.2.7 Quantitation of surface carboxyl groups based on electroactive aminoferrocene functionalization of graphene-COOH or MPA monolayer surface on 8xSPEs

8xSPEs were dry-coated with graphene-COOH or with a self-assembled monolayer of MPA (one 8xSPE was used for each modification) followed by carbodiimide activation of the surface carboxyl groups using the EDC (0.35 M)/NHS (0.1 M) solution mixture. A 4.5-µL solution of 1 mM aminoferrocene in PBS, pH 7.4 was then placed on the –COOH activated electrodes and incubated for 45 min in a cold and moist atmosphere. To ensure the covalent strategy of linking, we prepared graphene-COOH or MPA modified 8xSPEs with an electrostatically adsorbed layer of aminoferrocene. The electrodes were then rinsed with deionized water to remove any unbound molecules. Cyclic voltammograms (CVs) were recorded to calculate the electroactive aminoferrocene molecules, and in turn, the relative amounts of –COOH groups on graphene-COOH and MPA surfaces.

3.2.8 Electrochemical measurements of serum GADA by an immunoassay

Faradaic impedance measurements for various concentrations of MAG-protein A/G captured serum GADA (10% normal human serum) bound onto GAD-65 were performed at room temperature (23 ^{o}C) in an aqueous electrolyte solution containing 0.1 M KCl and 10 mM each of $Fe(CN)_6^{3-}$ /$Fe(CN)_6^{4-}$ as the redox probe. A potential of 0.2 V vs a pseudo Ag reference electrode was applied at an AC amplitude of 10 mV, and the frequency was scanned from 0.1-100 kHz. The experimental impedance data were fit by the Randles equivalent circuit model to determine the charge transfer resistance (R_{ct}) values. Differential pulse voltammetry (DPV) was employed as a complementary technique that measured current signals. The same redox solution as of the EIS assay was used to measure the currents upon scanning the potential from +0.6 to -0.1 V vs a pseudo-Ag reference electrode (50 mV for amplitude, 10 mV step potential, 20 ms sampling width, and 50 ms pulse width). Each experiment was replicated five times to obtain the average responses with good reproducibility.

3.3 Results and Discussion

3.3.1 Optimization of GAD-65 concentration on the immunosensor surface

The immunosensor responses for various concentrations of GAD-65 used for surface immobilization (325 ng mL^{-1} – 13 µg mL^{-1} in PBS, pH 7.4) (Fig. 2) upon binding of a constant serum concentration of GADA (4 ng mL^{-1} in 10% human serum) captured onto the MAG-protein A/G beads were measured. This procedure allowed us to identify the optimum GAD-65 concentration that provided the maximum R_{ct} signals for GADA binding. The R_{ct} values measured by Faradaic impedance spectroscopy for increasing concentration of surface immobilized GAD-65 antigen, are shown in Figure 2. No appreciable change in the R_{ct} was observed beyond 6.5 µg mL^{-1} of GAD-65 concentration. Therefore, we chose this solution concentration of GAD-65 to immobilize on the designed graphene-COOH surface for the immunosensor.

The amount of surface immobilized GAD-65 on the graphene-COOH modified surface was estimated to be 17 ± 2 pmol cm^{-2} when using a solution concentration of 6.5 µg mL^{-1} of GAD-65. This estimation was based on the difference in free GAD-65 amount in solution before and after immobilization (NanoOrange protein quantitation kit). The immobilization efficiency of GAD-65 was 76 ± 4% under the experimental conditions followed.

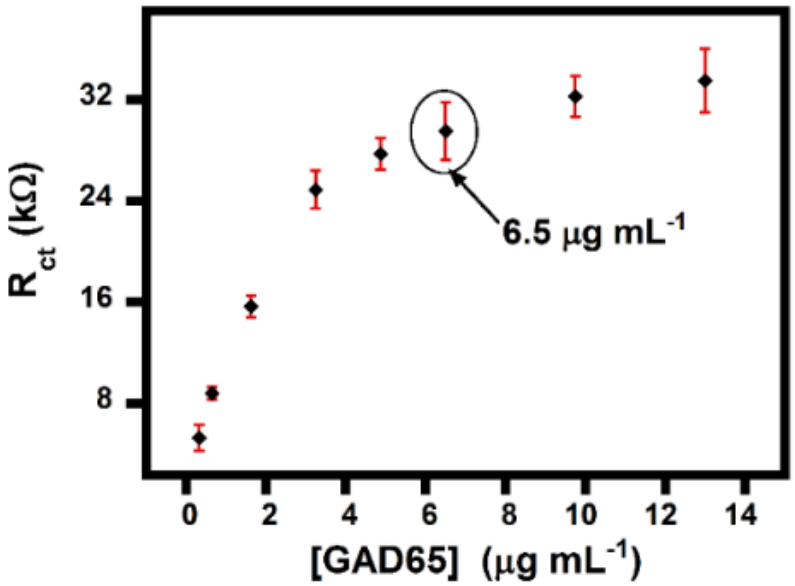

Figure 2. R_{ct} values for increasing solution concentration of GAD-65 (in PBS solution) used for immobilization onto the carbodiimide activated graphene-COOH/gold surface, and followed by the binding of a constant concentration of 10% serum GADA (4 ng mL^{-1}) captured onto MAG-protein A/G beads.

3.3.2 Hydrodynamic size and zeta potential measurements

We noted that the capturing of GADA from 10% human serum onto the MAG-protein A/G beads caused an increase in the average hydrodynamic size, and a negative shift in the Zeta potential of the beads (Table 1). This shift is reasonable because the IgG antibody has a net negative charge at pH 7.4 (isoelectric point is 6.1-6.5).[41]

Table 1. Hydrodynamic size and Zeta potential values of MAG-protein A/G and MAG-protein A/G-GADA beads (five times diluted in PBS, pH 7.4), temperature 25 ^{o}C.

Particle type	**Hydrodynamic size (nm)**	**Zeta potential (mV)**
MAG-protein A/G	1980 ± 49	-16 ± 1
MAG-protein A/G-serum GADA	2061 ± 37	-22 ± 2

The samples used for the hydrodynamic and Zeta potential analysis were five times diluted in PBS. This dilution was required to facilitate measurements within the saturating limit of the detector in the instrument.

3.3.3 Microscopic characterization of the graphene immunosensor

The SEM images acquired at each step of the immunoassembly on an 8xSPE array are presented in Figure 3 – A to D. We identified that a rough Au surface (gold-ink cured on a ceramic substrate at low temperatures, DropSens Inc.) provided better reproducibility of the immunoassay than a smooth gold surface (DRP-8x220BT- U20, DropSens Inc.). This is likely due to the stronger adhesion of the graphene-COOH onto the rough Au over a smooth Au surface. Also, we determined that the aqueous suspension of graphene-COOH is more suitable for dry coating on screen printed electrodes than an organic solvent dispersion based carbon nanomaterials. This is because the screen-printed electrode surface tends to wear away when exposed for longer duration in organic solvents during the dry-coating process of nanomaterials.

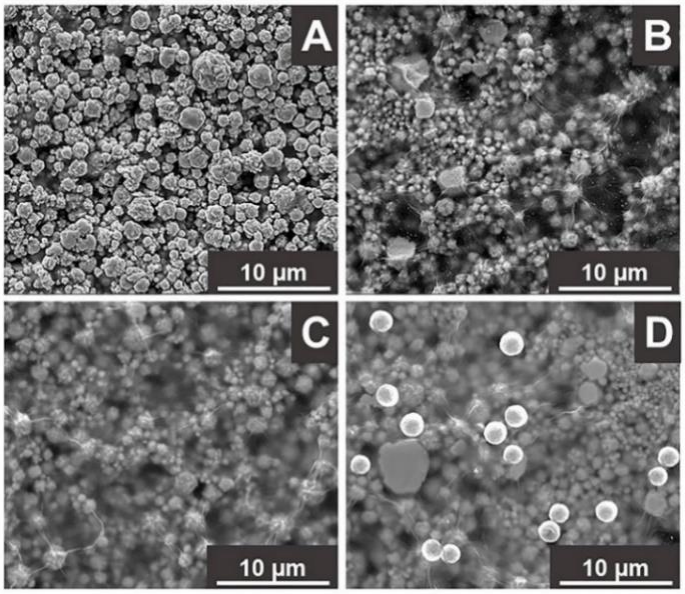

Figure 3. SEM images of A. rough AuSPE surface, B. after dry coating of an aqueous suspension of graphene-COOH, C. after covalent attachment of GAD-65 antigen and surface blocking with 1% BSA, and D. after the binding of GADA spiked in 10% human serum (0.05 ng mL^{-1}) and captured onto MAG-protein A/G beads.

Fig. 3-A shows the image for the rough Au surface of an 8xSPE array. Dry coating of graphene-COOH on the AuSPE surface resulted in spherical mesh-like and thread-like features (Fig. 3-B).[42] The graphene surface features became denser upon the covalent immobilization of GAD-65 antigen followed by blocking with a solution of 1% BSA in PBS (Fig. 3-C). After the binding of the MAG-protein A/G-GADA conjugate onto the surface GAD-65 sites, the appearance of spherical MAG bead features on the electrode surface can be seen (Fig. 3-D).

3.3.4 Spectroscopic characterization of the graphene immunosensor

FTIR spectra further confirmed the results obtained from the SEM image analysis. The bare AuSPE surface did not show any peak in the measured region of the IR spectrum (Fig. 4-a). Upon coating with graphene-COOH (Fig 4-b), the appearance of a strong and broad peak at about 3219 cm^{-1} was attributed to the hydroxyl vibration of surface carboxyl groups.[43] Additionally, the peaks at 1719 cm^{-1} and 1078 cm^{-1} are characteristics of the stretching vibrations of carboxylic acid and other surface carbonyl groups.[44] Upon activation of the surface carboxyl groups using EDC/NHS chemistry, the characteristic decrease in the O-H stretching vibration was observed (Fig 4-c).

Additionally, new peaks centered at 1764 and 1043 cm^{-1} corresponding to the C=O and C-O stretching vibrations of the succinimidyl esters from the EDC/NHS modification were present.[45,46]

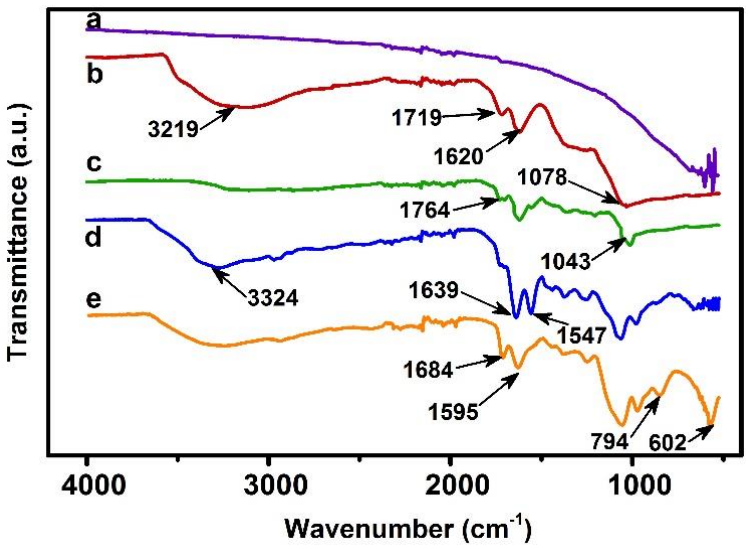

Figure 4. FTIR spectra of a. rough gold 8xSPE, b. after dry-coating with graphene-COOH, c. after EDC/NHS activation, d. after GAD-65 immobilization, and e. after the binding of 5 ng mL-1 concentration of 10% serum GADA captured by the MAG-protein A/G beads.

The protein amide-I band at 1639 cm^{-1} and amide-II band at 1547 cm^{-1} were observed due to the formation of amide bonds after the covalent attachment of the GAD-65 antigen with the graphene-COOH surface (Fig 4-d).[46,47] In addition, a new peak at 3324 cm^{-1} indicated the N-H stretching vibration of the protein. Once the serum GADA carried by the MAG-protein A/G beads was bound to the surface GAD-65 antigen, a new peak appearing at 602 cm^{-1} was assigned to the Fe-O stretching of Fe_3O_4 magnetic beads (Fig. 4-e).[48] Furthermore, a slight shift in the amide-I and amide-II bands was possibly the result of complexation of GAD-65 with GADA. In addition, the N-H bending vibration peak at 794 cm^{-1} became more prominent due to the overall increase in the total protein molecules on the surface as the result of GADA-GAD 65 immunoassembly formation.

3.3.5 Electrochemical impedance spectroscopy characterization of the immunosensor fabrication

The stepwise construction of the immunosensor assembly starting from the bare gold 8xSPE to the GADA binding measurement step was characterized by Faradaic EIS as shown in Figure 5 with

Nyquist plots. An aqueous solution containing 0.1 M KCl and a mixture of 10 mM of each potassium ferricyanide and potassium ferrocyanide [$Fe(CN)_6^{3-/4-}$] was employed as the redox probe in solution. The Randles equivalent circuit model was used to fit the experimental impedance spectra and obtain the R_{ct} values. The R_{ct} corresponds to the diameter of the semicircular region in the Nyquist plot.[49]

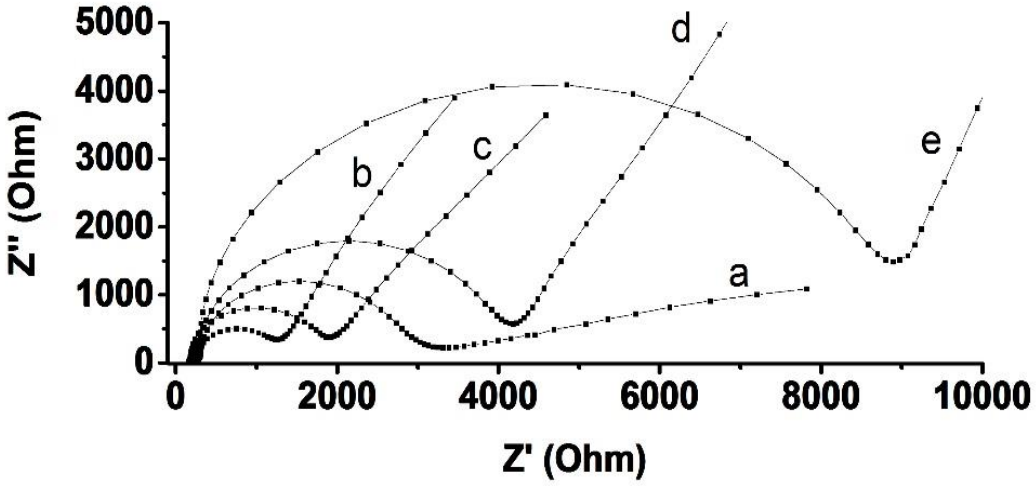

Figure 5. Faradaic impedance spectroscopic measurements in an aqueous solution containing 0.1 M KCl and 10 mM each of $Fe(CN)_6^{3-/4-}$ mixture: (a) AuSPE (3310 ± 101 Ω), (b) after dry-coating of graphene-COOH (1054 ± 154 Ω), (c) after covalently attaching GAD-65 by the carbodiimide coupling chemistry (2108 ± 67 Ω), (d) after blocking the free surface with 1% BSA (4190 ± 410 Ω), and (e) after the binding of serum GADA (0.04 ng mL^{-1}) captured onto the MAG-protein A/G beads (9290 ± 580 Ω). Experimental conditions: 0.2 V vs Ag/AgCl, amplitude 10 mV, and frequency range 0.1 - 100 kHz.

Figure 5 (curve a) corresponds to the Nyquist plot of a rough Au surface of 8xSPE. Carboxylated graphene modification of the Au surface decreased the R_{ct}, implying an increased surface conductivity favorable for the redox probe to communicate with the electrode (Fig. 5-curve b). This higher conductivity is advantageous to increase interfacial charge transport from the redox probe to the electrode, and subsequently facilitate sensitive monitoring of R_{ct} changes. Immobilization of the GAD-65 antigen (Fig. 5-curve c), subsequent BSA blocking of the free electrode surface (Fig.

5-curve d), and the binding of serum GADA (0.04 ng mL^{-1}) carrying MAG-protein A/G beads onto the surface GAD-65 increased the R_{ct} values (Fig. 5-curve e).

3.3.6 Estimation of signal enhancement and reduction of non-specific signals by the MAG-protein A/G beads over the direct use of serum GADA solution

Results indicate that the MAG-protein A/G bead strategy to isolate GADA from serum reduced the non-specific background signals from proteins and other components present in the free serum matrix, and thus offered an enhanced sensitivity (Fig. 6-A).[50-52] Although protein A/G is not selective for capturing GADA alone, but to all serum antibodies, the designed immunosensor is successful in measuring the low GADA concentration above the nonspecific control serum-treated MAG-bead signals (no spiked GADA).

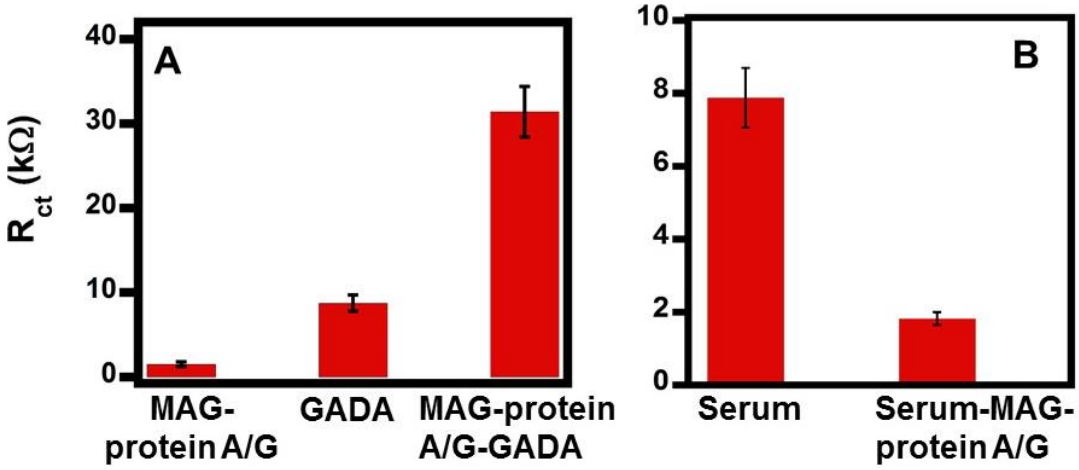

Figure 6. A. R_{ct} values for the BSA blocked, graphene-COOH coated gold surface immobilized with GAD-65 upon the binding of MAG-protein A/G beads alone (1.25 mg mL^{-1}), GADA (2 ng mL^{-1}) spiked in 10% serum in PBS (pH 7.4), and serum GADA (2 ng mL^{-1}) captured onto the MAG-protein A/G beads. **B.** Reduced non-specific background signals for MAG-protein A/G added to GADA unspiked serum compared to the GADA unspiked free serum solution.

Furthermore, Fig. 6-A shows that the R_{ct} signal enhancement for the binding of 2 ng mL^{-1} serum GADA captured with MAG-protein A/G beads was ~3-times greater than the direct use of GADA spiked 10% serum samples not captured onto the beads. This is the result of reduced nonspecific

signals from the MAG-protein A/G strategy over the free serum background signals (Fig. 6-B). The simplicity of magnetic capturing and isolation of the bound GADA from free serum by the MAG-protein A/G beads is not feasible with other non-magnetic nanomaterials,[53,] which would require centrifugation and other tedious separation procedures.

3.3.7 Serum GADA concentration dependent increase in charge-transfer resistance

The Faradaic impedance responses and the respective calibration plots are presented in Fig. 7-A to D. The R_{ct} of GAD-65 sensor surface increased with the binding of increasing serum GADA concentration (10% serum in PBS) captured with the MAG-protein A/G beads. This trend suggests that the increase in surface bound GADA carried by the MAG-protein A/G beads from the specific complexation with GAD-65 antigen sites increased the resistance to the ferri/ferrocyanide redox probe added in solution over the control serum treated with magnetic-protein A/G beads (no spiked GADA).

The results infer that the graphenyl sensor compared to the MPA monolayer modified sensor (0.04–0.75 ng mL^{-1}) displayed a wider dynamic range of 0.02 - 2 ng mL^{-1} and several thousands enhanced R_{ct} values for the same GADA concentration. The slope of the response curve in the linear range corresponds to the sensitivity of the sensor. A sensitivity enhancement of about 3-fold was observed for the graphenyl surface over the MPA modified surface (slopes in Figures-6C and 1D). The detection limits (three times the standard deviation of the control response/slope of the calibration graph) were 48 and 124 pg mL^{-1} for the graphenyl and MPA modified immunosensors, respectively. It is evident that the large surface area and -COOH functional groups on graphene-COOH are favorable for high-density immobilization of surface biomolecules to detect lower concentrations of analytes than the MPA monolayer sensor. The clinically relevant serum GADA concentration range has been reported to be 0.03–19.9 nM, or 1.95 ng mL^{-1}–1.29 µg mL^{-1}.[54] Saturation behavior on the assay response was observed beyond 2 ng mL^{-1} serum GADA.

Although, higher concentrations of GADA will require a dilution to measure in the designed assay platform, several biomarkers with clinically relevant low nM concentrations can directly benefit from the assay.

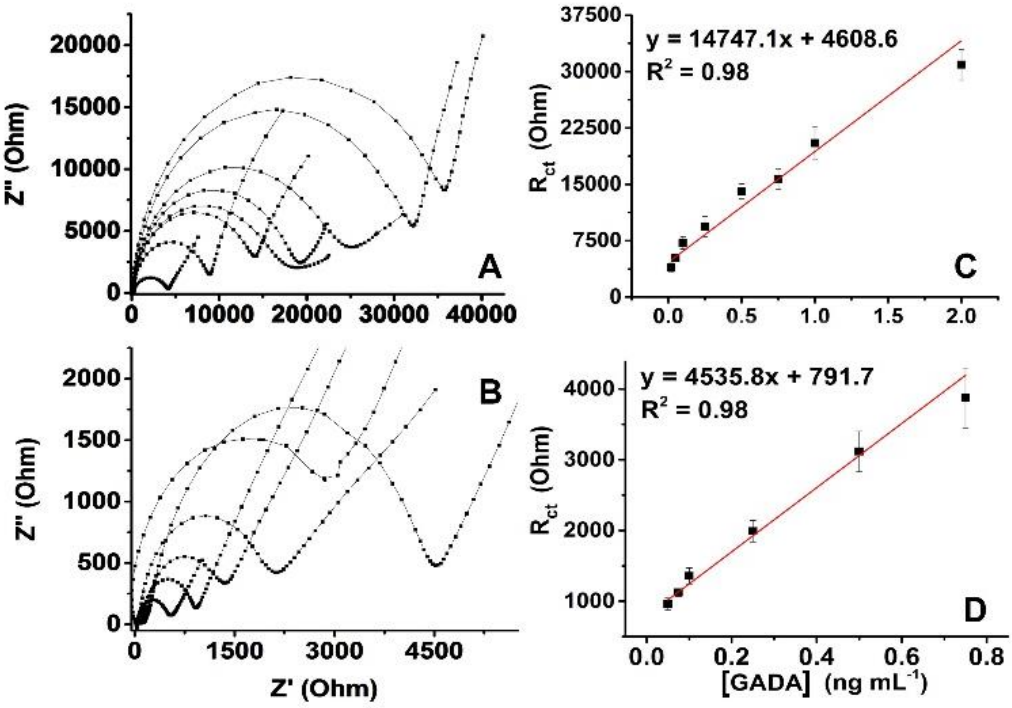

Figure 7. Nyquist plots obtained from the Faradaic impedance measurements in an aqueous solution containing 0.1 M KCl and 10 mM each of $Fe(CN)_6^{3-}/Fe(CN)_6^{4-}$ for various concentrations of surface bound serum GADA immunoassembly : A. Graphene-COOH (0.02, 0.05, 0.1, 0.25, 0.5, 0.75, 1, and 2 ng mL^{-1}) and B. MPA (0.02, 0.05, 0.1, 0.25, 0.5, and 0.8 ng mL^{-1}) modified immunosensors.C and D represent the dynamic range of respective response plots for R_{ct} changes with concentration of GADA for N = 3 replicates. Ten percent serum not spiked with any GADA but treated with the MAG-protein A/G beads was used as the control sample, and its R_{ct} value was subtracted from each of the GADA spiked serum sample responses. (Experimental conditions: 0.2 V vs pseudo-Ag reference electrode, amplitude 10 mV, and frequency range 0.1–100 kHz.)

3.3.8 Comparison of SPR responses for graphene-COOH and MPA modified immunosensor and bimolecular kinetic analysis

The kinetic parameters from the real-time binding of surface immobilized GAD-65 with MAG-protein A/G beads captured with serum GADA were determined by use of an SPRi assay. The

experimentally obtained SPR sensograms (Figure 8A and B) for different concentrations of GADA were fit into a 1:1 bimolecular kinetic model.[33,55] The equations presented below were used to calculate the association rate (k_a), the dissociation rate (k_d), and the binding constant (K_D) (Table 2). The kinetic analysis was performed for the biomolecule interaction by assuming a 1:1 binding reaction as detailed below:

$$A+B \rightleftharpoons AB \quad (1)$$

Rate of association: $$\frac{d[AB]}{dt} = k_a[A][B] - k_d[AB] \quad (2)$$

Rate of dissociation: $$\frac{d[AB]}{dt} = - k_d[AB] \quad (3)$$

where A is the GAD-65 antigen immobilized on the SPR chip, B is the GADA captured MAG-protein A/G beads, and AB is the antigen-antibody complex formed. Since the concentration of A is constant, the antigen-antibody complex formation is considered to follow pseudo first order kinetics, where the SPR responses of the interaction with time is given as:

$$\frac{dR}{dt} = k_a C R_{max} - (k_a C + k_d) R_t \quad (4)$$

The integrated form of (4) is given as:

$$R_t = \frac{k_a C R_{max}\left[1-e^{-(k_a C + k_d)t}\right]}{k_a C + k_d} + R_0 \quad (5)$$

$$K_D^{app} = \frac{k_d}{k_a} \quad (6)$$

Where, R_t and R_o are the SPR responses at any time t and at t = 0 respectively, R_{max} is the maximum reflectivity change, C is the concentration of serum GADA captured onto the MAG-protein A/G beads, k_a is the apparent association rate, k_d is the apparent dissociation rate, and K_D^{app} is the apparent binding constant. The values of k_a and k_d were obtained by fitting the experimental SPR curves using the TraceDrawer kinetics software.

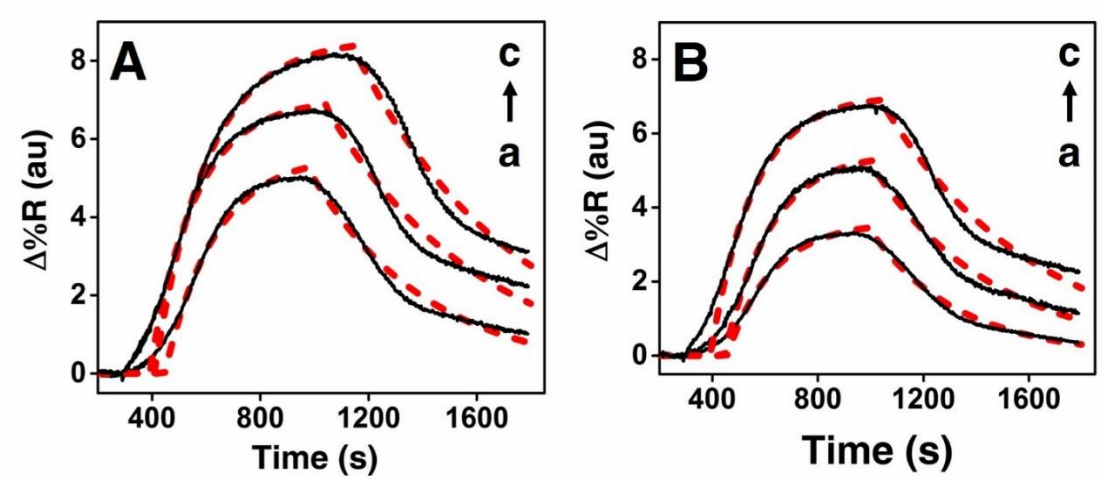

Figure 8. Simulated (red) and real-time SPR sensograms (black) for different concentrations (a to c) of 10% serum GADA, 0.05, 0.10, and 0.50 ng mL^{-1}, captured with MAG-protein A/G beads and bound onto GAD-65 immobilized sensor surfaces modified with A. graphene-COOH and B. MPA.

The lower K_D value for the graphene-COOH modified SPRi chip suggests that graphene provides a stronger GADA-GAD-65 binding interaction [i.e., a more sensitive platform from an analytical perspective] through its increased number of surface carboxyl groups and plasmon enhancing feature when compared to the MPA modified chip. Moreover, the K_D values of both MPA and graphene-COOH modified chips are smaller (better affinity) in comparison to the previously reported SPR assay value (K_D = 1.37 nM) in PBS buffer medium on the surface of a mixed self-assembled monolayer.[56] This is more likely due to the signal enhancements from the MAG-protein A/G bead strategy offering a highly enhanced signal output than free GADA present in solution. Moreover, the MAG-bead based strategy was shown to allow a significantly greater amount of immobilization of surface antibodies due to the large number of particles with a net high surface area.[57] This high-density antibody carrying beads are expected to facilitate a greater rate of association with surface GAD-65 molecules and a slower dissociation rate for graphene-COOH than the MPA surface (Table 2). A prior report estimated that over 100,000 molecules of antibody can be bound selectively to MAG-beads to obtain attomolar detection limits of prostate specific antigen.[52,57]

Table 2. Kinetic parameters for the MAG-protein A/G beads captured serum GADA binding onto a surface immobilized GAD-65 antigen.

Kinetic parameters	**Graphene-COOH**	**MPA**
Association rate constant, k_a [M^{-1} s^{-1}]	1.05 (± 0.13) × 10^9	0.90 (± 0.13) × 10^9
Dissociation rate constant, k_d [s^{-1}]	3.2 (± 0.4) × 10^{-3}	5.0 (± 0.6) × 10^{-3}
Binding constant, K_D [pM]	3.0 ± 0.5	5.6 ± 1.0

3.3.9 Validation of the graphene-COOH and MPA modified serum GADA

DPV was employed as a complementary method to the impedimetric immunosensor. Decrease in DPV peak currents was observed with the increase in serum GADA MAG-beads binding to surface GAD-65. This is because the insulating character imparted on the electrode surface by the bound MAG-protein A/G-GADA beads onto GAD-65 is expected to decrease the redox currents of the added ferri/ferrocyanide probe in solution (Figure 9). The DPV results are in correlation with EIS. The limits of detection were 34 and 92 pg mL^{-1} for the graphene-COOH and MPA modified immunosensors, respectively, which are slightly lower than the EIS method.

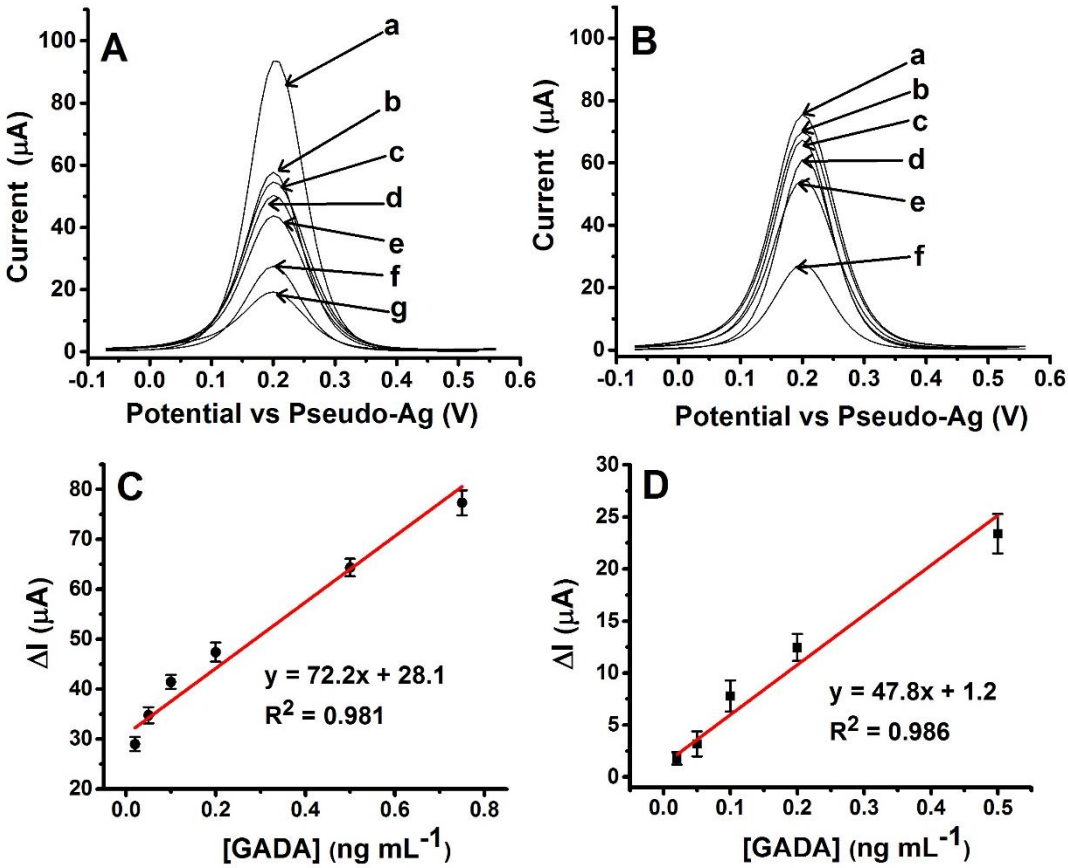

Figure 9. DPV responses showing the decrease in currents for 10% serum containing GADA concentrations of a. 0.0, b. 0.02, c. 0.05, d. 0.1, e. 0.2, f. 0.5, and g. 0.75 ng mL^{-1} captured with MAG-protein A/G beads, and upon binding with the surface GAD-65 antigen on A. graphene-COOH and B. MPA modified immunosensors. Experimental conditions: aqueous mixture containing 0.1 M KCl and 10 mM each of $Fe(CN)_6^{3-}/Fe(CN)_6^{4-}$ with potential scanned from + 0.6 to - 0.1 V vs a pseudo-Ag reference electrode. C and D represent the linear DPV responses of the immunosensors modified with graphene-COOH and MPA, respectively.

3.3.10 Estimation of the relative surface carboxyl groups on graphene-COOH and MPA modified gold surfaces

Figure 10-A and B show the cyclic voltammograms of the graphene-COOH and MPA coated electrodes covalently attached and electrostatically adsorbed with redox active aminoferrocene molecules (a and b, respectively, in each plot). Resulting peak currents and integrated peak areas

(charge in Coulombs) are directly proportional to the number of aminoferrocene molecules bound to either graphene-COOH or MPA surface. No redox peaks were shown by either the graphene-COOH or MPA surfaces not immobilized with aminoferrocene, confirming no interferences from the surface modifications on the –COOH estimation (Insets of Figure 11-A and B). The linear dependence of the anodic current with scan rate suggested that the voltammetry of aminoferrocene molecules exhibited a surface confined redox process (Figure 11-C and D).

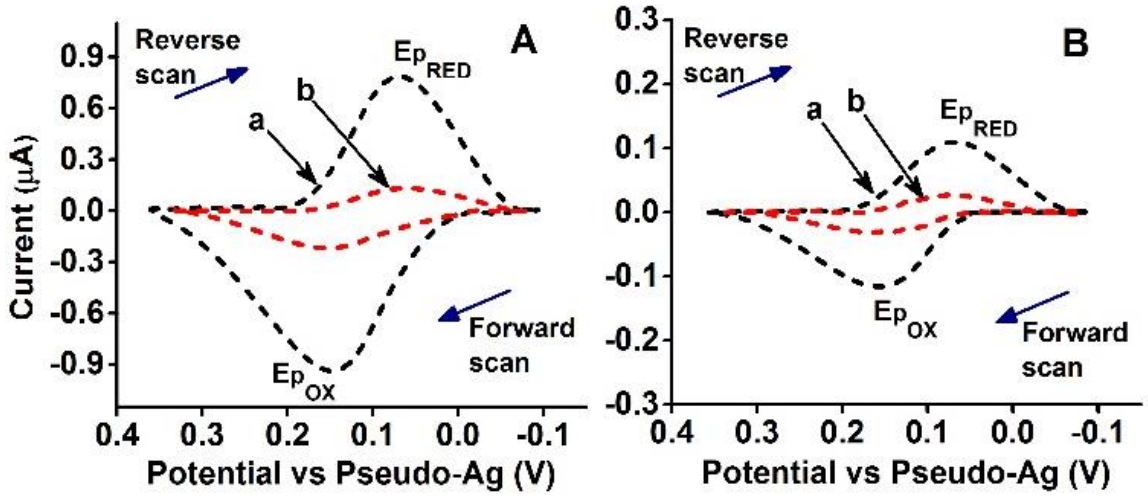

Figure 10. Background subtracted CVs of A. graphene-COOH, B. MPA modified gold electrodes with a. covalently attached, and b. adsorbed films of aminoferrocene in argon purged PBS buffer, pH 7.4, 23 °C. The scan rate was 0.1 V s^{-1}.

The average formal potentials of the covalently attached aminoferrocene film on the graphene-COOH and MPA surfaces were 112 ± 5 and 114 ± 8 mV, respectively. The electrostatically adsorbed films of aminoferrocene on each of the modified surfaces exhibited a similar formal potential as the covalent films. However, the covalent films enabled higher electroactive aminoferrocene immobilization than the electrostatic films as discussed below.

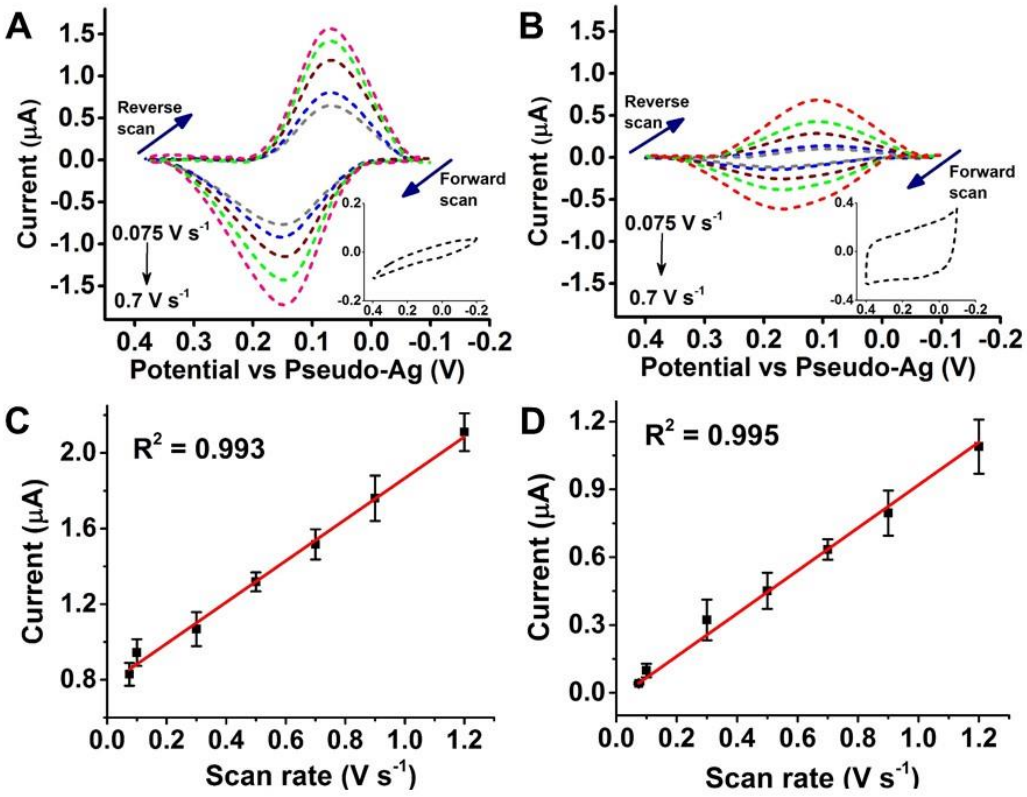

Figure 11. Background subtracted scan rate dependent CVs of the covalently attached aminoferrocene on A. graphene-COOH and C. MPA modified Au 8xSPEs and the respective plots of peak current vs scan rate (B and D). The scan rate inner to outer: 0.075 - 1.2 V s^{-1} at 23 °C, in PBS, pH 7.4.

From the measured oxidation peak area, the electroactive surface coverage (*Γ, Eq. 1*) of aminoferrocene and in turn the relative extent of carboxyl groups were determined.[58] *Q* is the area of the oxidation peak of aminoferrocene, *n* is the number of electrons involved in the aminoferrocene oxidation (*n* = 1), F is the Faraday constant, and A is the area of the working electrode (*A* = 0.2 cm^2).

$$\Gamma = Q / nFA \qquad \text{(Eq. 1)}$$

The *Γ* values were also calculated from the anodic peak current by using Eq. 2,[59] where I_p is the anodic peak current, *υ* is the scan rate, *R* is the universal gas constant (8.314 J mol^{-1} K^{-1}), and *T* (296 K) is the temperature in Kelvin.

$$I_p = n^2F^2\upsilon A\Gamma/4RT \qquad \text{(Eq. 2)}$$

The peak area and peak current based estimations of Γ agreed well with each other. The graphene-COOH surface provided 9-fold greater surface carboxyl groups than the MPA monolayer surface (Table 3).

Table 3. Estimated electroactive amounts of aminoferrocene on graphene-COOH and MPA modified electrodes. The estimations were based on anodic peak area (Q in nC) or peak currents (I_p in nA) from cyclic voltammograms shown in Fig. 9.

Parameter		**Graphene-COOH**	**MPA**
Covalently attached aminoferrocene	Q (nC)	920.3 ± 86.6	98.1 ± 5.9
	Calculated Γ (pmoles/cm^2)	47.6 ± 5.1	5.1 ± 0.3
	I_p (nA)	918.2 ± 76.2	108.3 ± 5.9
	Calculated Γ (pmoles/cm^2)	48.6 ± 4.2	5.7 ± 0.6
Adsorbed aminoferrocene	Q (nC)	189.4 ± 15.4	31.0 ± 1.9
	Calculated Γ (pmoles/cm^2)	9.8 ± 1.3	1.6 ± 0.11
	I_p (nA)	208.2 ± 28.3	34.2 ± 1.3
	Calculated Γ (pmoles/cm^2)	11.2 ± 2.5	1.8 ± 0.2

3.3.11 Application to T1D patient samples and validation by a commercial ELISA kit

We determined that the designed immunosensor platform is applicable to measure serum GADA concentrations in T1D patient serum samples. The samples were prepared in a similar manner as the spiked GADA serum standards, and captured onto MAG-protein A/G beads for detection upon binding onto surface immobilized GAD-65. A good correlation was obtained between our electrochemical immunoassay and the commercial ELISA kit (paired t-test performed at 95% confidence level). The dynamic range was sufficient to determine the sample GADA concentrations with a good precision (Table 4-A).

Table 4. A. Results from the analysis of patient samples (10% serum) on the designed graphene-COOH electrochemical immunosensor and ELISA (N = 3). B. Recovery data of the designed EIS immunoassay with the ELISA method for a patient serum sample spiked with GADA.

A. T1D patient samples	EIS immunosensor ($ng\ mL^{-1}$)	ELISA ($ng\ mL^{-1}$)
1	3.4 ± 0.2	3.0 ± 0.1
2	2.2 ± 0.3	1.9 ± 0.2

B. Method	Spiked [GADA] ($ng\ mL^{-1}$)	Measured [GADA] ($ng\ mL^{-1}$)	Recovery %
EIS	0.50	0.45	90%
	2.50	2.34	94%
ELISA	0.50	0.46	92%
	2.50	2.43	97%

To assess the accuracy of our electrochemical assay, a known concentration of GADA was spiked to one of the patient serum samples. A recovery percentage of ≥90% was obtained from the electrochemical assay, which is comparable to the recovery in ELISA (Table 4-B). The electrochemical immunoassay presented takes less time than the ELISA method (EIS immunoassay ~2 h 30 min, ELISA ~4h), requires smaller sample volumes (EIS immunoassay 3.5 μL per electrode, ELISA 100 μL sample per well), and with a reasonably good linear range (EIS immunoassay 0.02–2.0 ng mL^{-1}, ELISA 0.16–5.0 ng mL^{-1}). However, the EIS approach is throughput limited, because each impedance channel needs a separate potentiostat unit, hence an array-based impedance detection is an expensive approach. Therefore, our ongoing research direction is to translate the fundamental knowledge and assay designs derived from this work to develop a high-throughput cost-effective assay format.

3.4 Conclusions

The presented graphene modified immunosensor array successfully measured serum GADA levels at clinically relevant concentrations. The selectivity of GAD-65 on the sensor surface was useful to capture GADA carried by MAG-protein A/G beads. The combination of protein A/G coated MAG beads to separate GADA from serum samples minimized the effect of interferences from the serum matrix, and thus enhanced the detection sensitivity. Electrochemical and surface plasmon methods correlated with each other. Plasmon enhancing graphene-COOH offered better analytical detection features compared to a self-assembled monolayer of MPA. A good, statistically valid correlation was obtained for the electrochemical immunosensor with the commercial ELISA. Overall, the binding kinetics parameters can be used as an excellent quality control checkpoint for large-scale production of graphenyl biosensors for reliable applications in clinical diagnostic assays.

3.5 References

1. Wasserfall, C.H.; Atkinson, M.A. *Autoimmun. Rev*. **2006**, *5*, 424–428.
2. Morran, M. P.; Vonberg, A.; Khadra, A.; Pietropaolo, M. *Mol. Aspects Med.* **2015**, *42*, 42–60.
3. Pihoker, C.; Gilliam, L. K.; Hampe, C. S.; Lernmark, Å. *Diabetes* **2005**, *54*, S52–S61.
4. Atkinson, M. A.; Eisenbarth, G. S. *The Lancet* **2001**, *358*, 221–229.
5. Akerblom, H. K.; Vaarala, O.; Hyöty, H.; Ilonen, J.; Knip, M. *Am. J. Med. Genet.* **2002**, *115*, 18–29.
6. Ziegler, A.-G.; Nepom, G. T. *Immunity* **2010**, *32*, 468–478.
7. Gan, M. J.; Albanese-O'Neill, A.; Haller, M. J. *Curr. Probl. Pediatr. Adolesc. Health Care.* **2012**, *42*, 269–291.
8. Lehuen, A.; Diana, J.; Zaccone, P.; Cooke, A. *Nat. Rev. Immunol.* **2010**, *10*, 501–513.
9. Pociot, F.; Lernmark, Å. *The Lancet* **2016**, *387*, 2331–2339.
10. Urban, G. J. G.; Friedman, M.; Ren, P.; Törn, C.; Fex, M.; Hampe, C. S.; Lernmark, Å.; Landegren, U.; Kamali-Moghaddam, M. *Sci. Rep.* **2015**, *5*.
11. Heding, L. G. *Diabetologia* **1975**, *11*, 541–548.
12. Andersen, L.; Dinesen, B.; Jorgensen, P. N.; Poulsen, F.; Roder, M. E. *Clin. Chem.* **1993**, *39*, 578–582.
13. Forest, J. C.; Masse, J.; Lane, A. *Clin. Biochem.* **1998**, *31*, 81–88.
14. Miao, D.; Guyer, K. M.; Dong, F.; Jiang, L.; Steck, A. K.; Rewers, M.; Eisenbarth, G. S.; Yu, L. *Diabetes* **2013**, *62*, 4174–4178.
15. Bonaccorso, F.; Sun, Z.; Hasan, T.; Ferrari, A. *Nat. Photon.* **2010**, *4*, 611–622.
16. Chiu, N.-F.; Huang, T.-Y.; Lai, H.-C.; Liu, K.-C. *Nanoscale Res. Lett.* **2014**, *9*, 1.
17. Lee, H.; Choi, T. K.; Lee, Y. B.; Cho, H. R.; Ghaffari, R.; Wang, L.; Choi, H. J.; Chung, T. D.; Lu, N.; Hyeon, T.; Choi, S. H.; Kim, D.-H. *Nat. Nanotechnol.* **2016**, *11*, 566–572.
18. Patil, A. V.; Fernandes, F. B.; Bueno, P. R.; Davis, J. J. *Bioanalysis* **2015**, *7*, 725–742.

19. Yang, W.; Ratinac, K. R.; Ringer, S. P.; Thordarson, P.; Gooding, J. J.; Braet, F. *Angew. Chem. Int. Ed.* **2010**, *49*, 2114–2138.
20. Ma, H.; Wu, D.; Cui, Z.; Li, Y.; Zhang, Y.; Du, B.; Wei, Q. *Anal. Lett.* **2013**, *46*, 1–17.
21. Shanbhag, V. K. L.; Prasad, K. S. *Anal. Methods* **2016**, *8*, 6255–6259.
22. Pu, Y.; Zhu, Z.; Han, D.; Liu, H.; Liu, J.; Liao, J.; Zhang, K.; Tan, W. *Analyst* **2011**, *136*, 4138–4140.
23. Yagati, A. K.; Park, J.; Cho, S. *Sensors* **2016**, *16*, 109.
24. Son, S.J.; Reichel, J.; He, B.; Schuchman, M.; Lee, S. B. *J. Am. Chem. Soc*. **2005**, *127*, 7316–7317.
25. Connolly, D.; Currivan, S.; Paull, B. *Proteomics*, **2012**, *12*, 2904–2917.
26. Zeng, S.; Baillargeat, D.; Ho, H. P.; Yong, K.T. *Chem. Soc. Rev.* **2014**, *43*, 3426–3452.
27. Singh, V.; Krishnan, S. *Anal. Chem.* **2015,** *87*, 2648–2654.
28. Ríos, A.; Zougagh, M.; Bouri, M. *Anal. Methods*, **2013**, *5*, 4558–4573.
29. Bao, F.; Yao, J. L.; Gu, R. A. *Langmuir*, **2009**, *25*, 10782–10787.
30. Nam, J. M.; Thaxton, C. S.; Mirkin, C. A. *Science*, **2003**, *301*, 1884–1886.
31. Shad, T. C.; Elghanian, R.; Thomas, A. D.; Stoeva, S. I.; Lee, J-. S.; Smith, N. D.; Schaeffer, A. J.; Klocker, H.; Horninger, W.; Bartsch, G.; Mirkin, C. A. *Proc. Natl. Acad. Sci.* **2009**, *106*, 18437–18442.
32. Zhao, X.; Shippy, S. A. *Anal. Chem.* **2004**, *76*, 1871–1876.
33. Singh, V.; Nerimetla, R.; Yang, M.; Krishnan, S. *ACS Sensors*, **2017**, *2*, 909–915.
34. Mani, V.; Chikkaveeraiah, B. V.; Rusling, J. F., *Expert. Opin. Med. Diagn*. **2011**, *5*, 381–391.
35. Paleček, E.; Fojta, M. *Talanta*, **2007**, *74*, 276–290.
36. Adam, V.; Huska, D.; Hubalek, J.; Kizek, R. *Microfluid. Nanofluidics*, **2010**, *8*, 329–339.
37. Laschi, S.; Centi, S.; Mascini, M.; *Bioanal. Rev*. **2011**, *3*, 11–25.
38. Kamin, R. A.; Wilson, G. S. *Anal. Chem.* **1980,** *52*, 1198–1205.

39. Premaratne, G.; Nerimetla, R.; Matlock, R.; Sunday, L.; Hikkaduwa Koralege, R. S.; Ramsey, J. D.; Krishnan, S. *Catal. Sci. Technol*. **2016**, *6*, 2361–2369.

40. Niroula, J.; Premaratne, G.; Shojaee, S. A.; Lucca, D. A.; Krishnan, S. *Chem. Commun*. **2016**, *52*, 13039-13042.

41. Wu, X. Z.; Huang, T.; Mullett, W. M.; Yeung, J. M.; Pawliszyn, J. J. *Microcolumn Sep*. **2001**, *13*, 322-326.

42. Wang, H.; Shi, L.; Yan, T.; Zhang, J.; Zhong, Q.; Zhang, D. *J. Mater. Chem. A.* **2014**, *2*, 4739-4750.

43. Wu, H.; Zhao, W. F.; Hu, H. W.; Chen, G. H. *J. Mater. Chem.* **2011**, *21*, 8626.

44. Wu, N.; She, X.; Yang, D.; Wu, X.; Su, F.; Chen, Y. *J. Mater. Chem*. **2012**, *22*, 17254-17261.

45. Ding, W.; Cai, J.; Yu, Z.; Wang, Q.; Xu, Z.; Wang, Z.; Gao, C. *J. Mater. Chem. A.* **2015**, *3*, 20118-20126.

46. Falahati-Pour, S. K.; Lotfi, A. S.; Ahmadian, G.; Baghizadeh, A. *J. Appl. Microbiol*. **2015**, *118*, 976-988.

47. Song, X.; Wang, L.; Tang, C. Y.; Wang, Z.; Gao, C. *Desalination* **2015**, *369*, 1-9.

48. Liao, T.; Yuan, F.; Yu, H.; Li, Z. *Anal. Methods*, **2016**, *8*, 1577-1585.

49. Lee, K. Willner, I.; Throckmorton, D. J.; Singh, A. K. *Anal. Chem*. **2001**, *73*, 5287 −5295.

50. Lee, K. B.; Park, S.; Mirkin, C. A. *Angew. Chem*. **2004**, *116*, 3110-3112.

51. Shen, M.; Joshi, A. A.: Vannam, R.; Dixit, C. K.; Hamilton, R. G.; Kumar, C.V.; Rusling, J. F.; Peczuh, M. W. *ChemBioChem,* **2017**, DOI:10.1002/cbic.201700513

52. Krishnan, S.; Mani, V.; Wasalathanthri, D.; Kumar, C. V.; Rusling, J. F., *Angew. Chem. Int. Ed*., **2011**, *50*, 1175-1178.

53. Stoeva, S. I.; Lee, J. S.; Smith,J. E.; Rosen, S. T.; Mirkin, C. A. *J. Am. Chem. Soc*., **2006**, *128*, 8378-8379.

54. Walikonis, J. E.; Lennon, V. A. *Mayo Clin. Proc.* **1998**, *73*, 1161–1166.

55. Walgama, C.; Al Mubarak, Z. H.; Zhang, B.; Akinwale, M.; Pathiranage, A.; Deng, J.; Berlin, K. D.; Benbrook, D. M.; Krishnan, S. *Anal. Chem.* **2016**, *88*, 3130–3135.
56. Nogues, C.; Leh, H.; Langendorf, C. G.; Law, R. H. P.; Buckle, A. M.; Buckle, M. *PLoS ONE* **2010**, *5*, e12152.
57. Mani, V.; Wasalathanthri, D. P.; Joshi, A. A.; Kumar, C. V.; Rusling, J. F. *Anal. Chem.* **2012**, *84*, 10485–10491.
58. Booth, M.A.; Kannappan, K.; Hosseini, A.; Partridge, A. *Langmuir*, **2015**, *31*, 8033–8041.
59. R.W. Murray, in: A.J. Bard (Ed.), Electroanal. Chem., Marcel Dekker, NewYork, **1984**, *13*, 53–157.

CHAPTER 4

MEASURING ULTRA-LOW LEVELS OF NUCLEOTIDE BIOMARKERS USING QUARTZ CRYSTAL MICROBALANCE AND SPR MICROARRAY IMAGING METHODS: A COMPARATIVE ANALYSIS

4.1 Introduction

In recent years, DNA-based biosensors have received immense attention due to their applicability in the fields of gene sequencing,[1] therapeutic and delivery systems,[2] pathogen detection,[3-5] and forensic studies.[6] Single stranded DNA molecules can be used as inexpensive molecular analogs of RNA for assay methodology development for complex sample matrices. Recently, microRNAs (miRNAs) have become important genetic biomarkers for early diagnosis of various diseases, including cancer,[7,8] and lung diseases.[9,10] miRNAs are a group of small RNAs approximately 21–25 nucleotides in length that function mainly by binding the 3′-untranslated regions of specific target messenger RNAs (mRNAs) to repress protein translation or cleave mRNAs.[11] In particular, miRNA-21 has been found to be relevant to infectious diseases, such as viral[12] and bacterial[13] infections, as well as non-infectious diseases such as cardiovascular disorder[14] and cancer.[15] Hence, ultra-sensitive and selective detection of miRNA biomarkers present in a complex clinical matrix such as blood, plasma, or serum is significant for diagnostic applications.

Adapted from G. Premaratne, Z. H. Al Mubarak, L. Senavirathna, L. Liu, and S. Krishnan, Measuring Ultra-low Levels of Nucleotide Biomarkers Using Quartz Crystal Microbalance and SPR Microarray Imaging Methods: A Comparative Analysis, *Sensors & Actuators: B. Chemical*, **2017**, *253*,368–375 with permission from Elsevier.

Suitable structural features of a capture oligonucleotide probe are essential for selective hybridization with a target miRNA in the presence of other nucleotides. A quartz crystal microbalance (QCM) is a mass sensor that provides both qualitative and quantitative measurements by translating changes in the oscillation frequency of the quartz crystal to the corresponding mass changes.[16] Surface plasmon resonance imaging (SPRi)[17-19] is an emerging technique that is superior to conventional SPR for *in situ* detection of biomolecular interactions in real-time in a single microarray platform.[20,21] SPRi offers simplicity and higher throughput compared to the conventional single sample analysis by allowing measurements at a fixed angle of incidence to directly collect reflectivity changes (ΔR%) across an array of gold spots.[22] Furthermore, the SPRi microarray requires less assay time than conventional SPR to analyze several replicates at once leading to high precision.[23,24] The hybridization of oligonucleotides with the SPR surface-immobilized capture probe results in an increase in the refractive index. The use of gold nanoparticles (AuNPs) has been shown to increase the reflectivity changes of a hybridization reaction due to their effect on enhancing the surface plasmon signals.[25-27]

In this study, an inexpensive target oligonucleotide containing a similar number of nucleotides to that of the miRNA-21 marker with thymine in place of uracil and with a poly-T tail and a free thiol group was designed to covalently attach to AuNPs via the well-known Au-thiol chemisorption.[28] The AuNP-linked mimic oligonucleotide was hybridized with a complementary surface immobilized capture probe. The effect of serum matrix percentage on the resulting detection signals for the miRNA-21 mimic was evaluated. Selectivity of the assay also was assessed using a five base pair mismatch-containing sequence as the control. Furthermore, we measured the changes in SPR reflectivity with an image output in the designed hybridization assay along with quantitative QCM mass analysis. Such oligonucleotide models are a cost-effective way to develop sensitive assay strategies for complex sample matrices, compare two analytical methods, and evaluate the

efficiency of a hybridization strategy that may be useful for measuring ultra-low levels of miRNA markers in circulating body fluids.

4.2 Experimental

4.2.1 Materials and chemicals

Thiol-modified custom-designed oligonucleotides (sequences are presented in Table 1), dithiothreitol (DTT), 6-mercaptohexanol (MHOH), and NAP-10 columns were obtained from Sigma-Aldrich (Woodlands, TX, USA). AuNPs (50 nm diameter) were purchased from BBI Solutions (Cardiff, UK). Human serum samples were purchased from Fitzgerald Industries International Inc. (North Acton, MA, USA). SpotReady-16 gold spotted glass microarray chips (spot size 1 mm diameter, SPR-1000-016) were obtained from GWC Technologies (Madison, WI, USA).Gold disc infused quartz crystals (gold diameter 0.2 inch) used for the QCM were purchased from International Crystal Manufacturing Co, Inc.(Oklahoma City, OK, USA). All other chemicals were of high-purity analytical grade. To prepare all solutions, ultrapure distilled water (DNAse and RNAse free) purchased from Life Technologies (Carlsbad, CA, USA) was used.

Table 1. Sequences of designed oligonucleotides.

Surface capture Probe	5′-HS-TGTCAGACAGCCCATCGACTGGTGTTGCCATGAGATTCAACAGTCAACATCAGTCTGATAAGCTACCCGACA-3′
Target	5′-HS-TTTTTTTTTTTTTTTTTTTTTTTTTTTTTTTTTTTTTTTTTTTTTTTTTTTTTTTTTTAGCTTATCAGACTGATGTTGA-NH_2-3′
Control	5′-HS-TTTTTTTTTTTTTTTTTTTTTTTTTTTTTTTTTTTTTTTTTTTTTTTTTTTTTTTTTAGGATATCACACTGATGAAGA-NH_2-3′

The hybridization sequences for probe, target, and control are highlighted. Base pair mismatches of the control with respect to the target are highlighted in red. The addition of Poly-T_{50} segments to the target and control sequences provides stability and flexibility to the strands.[29]

4.2.2 Instrumentation

The optical imaging experiments were performed using a SPRimagerII array instrument at room temperature (GWC Technologies). The experiments were conducted using a dual-channel set-up equipped with two syringe pumps (100 µL sample loop, New Era Pump System, Inc., Farmingdale, NY, USA) in order to assess hybridization of the target and control oligonucleotides with the surface capture probe. The Digital Optics V++ software package provided with the instrument was used to collect SPRi difference images (i.e., differences of the pixel intensities before and after hybridization events), and the images were visualized using ImageJ 1.49v software (National Institutes of Health, USA).

The mass changes resulting from hybridization were measured using a QCM instrument (Gamry Instruments Inc., Warminster, PA, USA). Each modification step on the gold quartz crystal was performed offline, and the frequency changes were measured in the QCM system at a sample measurement interval of 0.1 s until a constant frequency response with time was reached. The fundamental oscillation frequency of the crystals was 10 MHz, and the QCM sensor surface was immersed in 0.1 M NaCl/0.1 M sodium phosphate buffer (pH 7.4) during measurements.

A Nanodrop ND1000 spectrophotometer (Thermo Scientific, Waltham, MA, USA) was used to quantify the surface capture probes immobilized on the SPR array or quartz crystal surface and additionally to quantify the target and control oligonucleotides linked to AuNPs. Surface characterization of the gold surface of the SPR microarray before and after coating with the surface capture probe was conducted by scanning electron microscopy (SEM, Model: FEI Quanta 600FE). An accelerating voltage of 20 kV was applied. The images were acquired using the FEIxT Microscope Control Software.

4.2.3 AuNP-linked oligonucleotide preparation

The disulfide-modified oligonucleotide reduction protocol provided by the manufacturer (Sigma-Aldrich) was followed to activate the oligonucleotides to link with the AuNPs. For thiol activation, the dry oligonucleotide samples were treated with an aqueous solution of DTT (100 mM) at a 10:1 ratio (µL DTT to A_{260} units of oligonucleotides), which is sufficient to activate the thiol groups of the oligonucleotides.[30] The reaction mixture was incubated for 1 h at room temperature. DTT and other reaction byproducts were removed using a NAP-10 column that was pre-equilibrated with approximately 15 mL of 50 mM sodium phosphate buffer (pH 6.0). The purified oligonucleotides were quantified by measuring absorbance at 260 nm using a Nanodrop spectrophotometer (1 mm path length light source; CCD array detector).[31,32] The molar extinction coefficient of each oligonucleotide sequence was used to calculate concentrations (ε_{probe}: 698.2, ε_{target}: 637.9, $\varepsilon_{control}$: 622.7 $mM^{-1}\,cm^{-1}$, Sigma-Aldrich).

AuNP-linked oligonucleotides were prepared with slight modifications to previously described methods.[33-35] Briefly, 250 µL of test concentrations (50 fM – 50 pM) of the target and control oligonucleotides were prepared in sodium phosphate buffer (pH 6.0), mixed with 100 µL of 50 nm AuNP solution, and incubated for 4 h at 37 °C. At the completion of incubation, 150 µL of 1 M NaCl/0.1 M sodium phosphate buffer (pH 7.4) and 350 µL of distilled water were added, and the samples were left to age in an incubator for 24 h at 37 °C. The samples then were centrifuged at 12,500 rpm for 45 min to remove the supernatant, and the precipitate obtained was rinsed twice with 0.1 M NaCl/0.1 M sodium phosphate buffer (pH 7.4). Samples were resuspended to the original volume of 250 µL using the same buffer solution for both SPRi and QCM analysis. The calibration plot generated for the AuNP-target oligonucleotide conjugates was used to assess the recovery when the target oligonucleotide was dissolved in various percentages of human serum.

4.2.4 Quartz crystal surface modification and detection

New gold-coated quartz crystals were washed with ethanol followed by distilled water and dried under N_2 gas prior to surface modification steps. Each crystal was incubated with 20 µL of thiol-activated probes for 4 h in a moist and cold environment (4 ^oC) following a wash with phosphate buffer (pH 7.4). The free surface was blocked using 25 µL of 5 mM MHOH, followed by a wash with distilled water after a 30 min incubation. The initial oscillation frequency was measured by QCM in solution mode. The surface capture probe-modified quartz crystals were exposed to 20 µL of AuNP-linked control oligonucleotide for 45 min and then washed with 0.1 M NaCl/0.1 mM sodium phosphate buffer (pH 7.4) to remove any unbound material from the crystal surface. Decrease in the oscillation frequency was measured on the modified quartz crystal surface. The same crystals were exposed to 20 µL of AuNP-linked target oligonucleotide (miRNA-21 mimic) and incubated for 45 min. Decrease in the frequency of the quartz crystal was measured after washing with 0.1 M NaCl/0.1 M sodium phosphate buffer (pH 7.4) to remove any unbound target oligonucleotide. Separate experiments were conducted using the target and control oligonucleotides that were devoid of AuNP conjugation to assess the signal amplification resulting from the AuNP linkage strategy.

4.2.5 Modification of the SPR microarray surface and detection

After an initial wash step of the SPR gold array chip with ethanol, 20 µL of thiol-activated capture probes (Figure 1) were added to 12 spots and incubated for 4 h in a moist and cold environment (4 ^oC), followed by washing with phosphate buffer (pH 7.4). The free surface of the whole array was blocked by incubation with 25 µL of 5 mM MHOH for 30 min to minimize nonspecific binding interactions. The modified chip was immediately placed on the SPRi dual flow channel system. The chip-prism contact surface was filled with a layer of index matching fluid (Cargille Labs, Cedar Grove, NJ, USA). Two sample injector units and two syringe pump systems were connected to the

flow channels. Real-time measurements were taken using the running buffer, 0.1 M NaCl/0.1 M sodium phosphate buffer (pH 7.4).

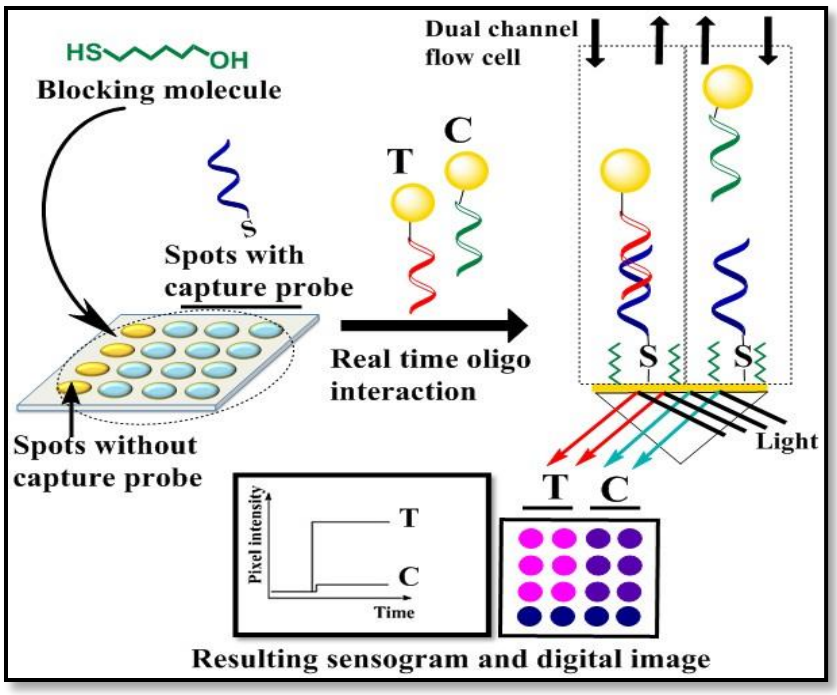

Figure 1. Fabrication procedure of the SPR microarray chip for selective detection of the target miRNA-21 mimic (T) from the control (C) oligonucleotide sequence by hybridization in a dual channel SPRi system.

The running buffer was pumped at a flow rate of 50 µL/min, and a reference image of the array was taken. The dual sample injector loops (100 µL volume) were then separately filled with suspensions of target or control oligonucleotide-conjugated AuNPs in 0.1 M NaCl/0.1 M sodium phosphate buffer (pH 7.4) and allowed to pass onto the capture probe-modified array surface for 45 min. Upon completion of the incubation, the chip surface was washed for 10 min with the running buffer to remove all unhybridized oligonucleotides present in solution. The final images of the microarray, after introducing target and control oligonucleotides, were acquired using a CCD camera. The difference between the images taken before and after the hybridization events were obtained as SPR pixel intensity changes, which can be represented in a 3D format using ImageJ software. Gold spots treated with only the blocking reagent were used to assess nonspecific signals.

Two control spots and six test spots each for detecting the target and control nucleotides were designed within the same microarray chip, which minimized spot-to-spot variations among different chips. The average SPR pixel intensities and standard deviations were calculated from the results obtained for six test spots with three replicate measurements.

4.3 Results and Discussion

4.3.1 Spectroscopic analysis of AuNP-linked oligonucleotides

Figure 2 shows the UV-vis spectra of unmodified AuNPs in aqueous solution and AuNPs linked with 5′- thiol modified control and target oligonucleotides in 0.1 M NaCl/0.1 M sodium phosphate buffer (pH 7.4). After linking AuNPs to the target and control oligonucleotides, the Soret band absorbance shifted from 517 nm to 526 and 524 nm, respectively.

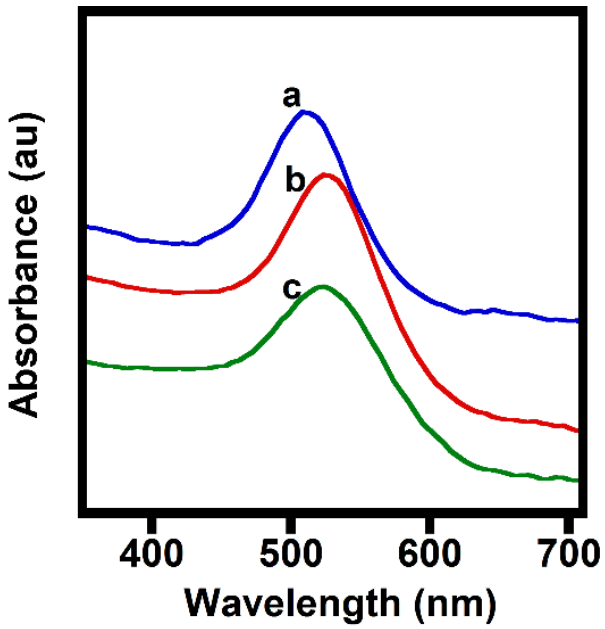

Figure 2. UV-visible spectra of (a) AuNPs before conjugation to oligonucleotides and AuNPs linked to (b) target or (c) control oligonucleotide present in 0.1 M NaCl/ 0.1 M sodium phosphate buffer (pH 7.4).

The shift could be a result of surface modifications that occurred on the AuNPs and/or the centrifugation step used to separate the AuNP-linked oligonucleotides affecting the particle size distribution.[36] The oligonucleotide linking to AuNPs was free of aggregate formation, as no drastic changes in the absorption band or decrease in peak intensity were detected. Aggregation of 13 nm AuNPs upon conjugation with thiolated oligonucleotides has been shown to red shift the Soret

band.[37] Thus, the absence of notable aggregation in our system was possibly facilitated by the relatively larger AuNPs (50 nm) and/or negatively charged citrate stabilization of the AuNPs that repel particle aggregation.[38]

Table 2 presents the results of quantitation of thiol-activated oligonucleotides before and after attachment to gold surfaces, which was performed to estimate binding efficiency. The immobilization efficiency of the surface capture probe was slightly greater for the QCM than for the SPR microarray. This can be attributed to the larger surface area provided by the gold disc of the QCM crystal (0.2 cm^2) compared to the gold spots of the SPR microarray (0.008 cm^2). Binding of the surface capture probe to the gold surface of the quartz crystal resulted in a frequency change of 979 ± 18 Hz, which corresponded to a mass change of 662 ± 12 ng. This correlates with the results obtained from Nanodrop analysis of the surface capture probes that were bound to the quartz crystal.

Table 2. Quantitation of oligonucleotides immobilized on the QCM or SPR gold surface and conjugated to AuNPs (N = 3 replicates).

Molecule type	**Surface used to bind**	**Amount introduced (pmoles)**	**Amount bound (pmoles)**	**Average percentage binding**
Surface capture probe (9.3 nM)	SPR microarray	461.4 ± 26.8	375.3 ± 39.6	81%
	Quartz crystal	461.4 ± 26.8	406.5 ± 41.7	88%
Target (10 nM)	AuNPs	2.48 ± 0.35	2.17 ± 0.23	87%
Control (10 nM)	AuNPs	2.52 ± 0.41	2.27 ± 0.16	91%

Capture efficiencies of >80% suggest that the design of the surface capture probe on the gold surface of the quartz crystal and microarray was efficient and that the strategy for AuNP conjugation of target and control oligonucleotides was effective. The globular morphologies that appeared after modifying the SPR microarray surface with capture probes are presented as SEM images (Fig. 3A–C).

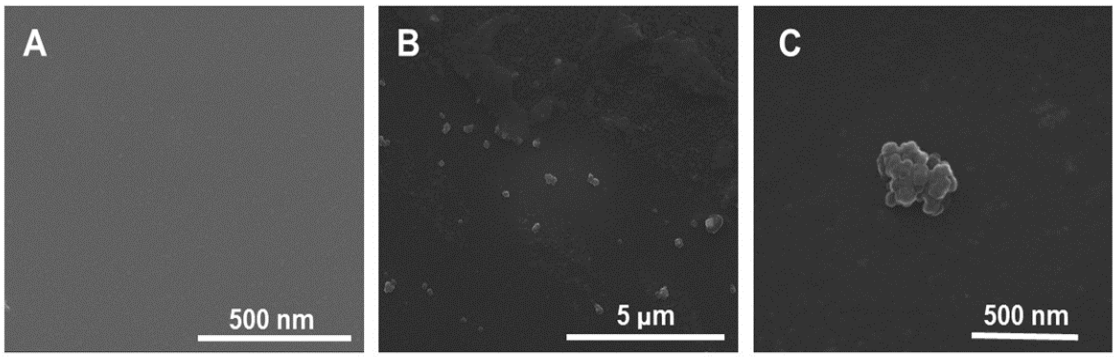

Figure 3. SEM images of (A) a bare gold spot of the SPR microarray before modification and (B) the gold spot self-assembled with the thiol-activated surface capture probe. (C) Higher magnification image of (B).

4.3.2 Assessment of target hybridization and signal amplification by the mass sensor

We quantified the mass changes that occurred on the quartz crystal (Δm) based on the observed decrease in oscillation frequency for successive modification steps and by using the Sauerbrey equation:

$$\Delta f = \frac{-2 f_o^2 \Delta m}{A \sqrt{\mu \rho}}$$

where Δf is the frequency change from the mass adsorbed, f_o is the fundamental frequency of oscillation (10 MHz), A is the geometric area of the gold disc bonded to the quartz crystal (0.2 cm^2), μ is the shear modulus of the quartz crystal (2.947×10^{11} dyn cm^{-2}), and ρ is the density of the quartz crystal (2.648 g cm^{-3}).[39-41] The Sauerbrey equation, used to calculate the mass bound on

to the quartz crystal, has a thousand times greater sensitivity compared to an electronic balance with 0.1 µg sensitivity.[42]

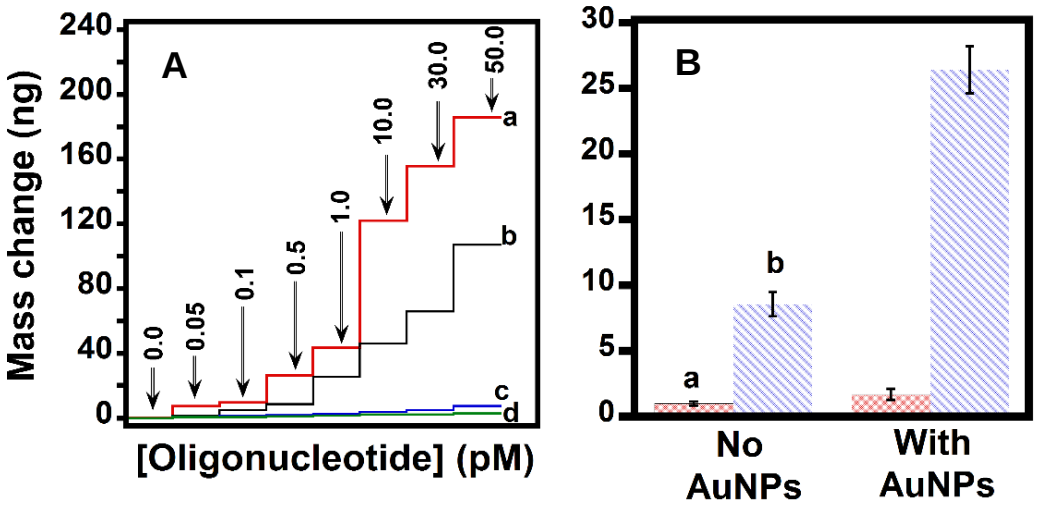

Figure 4. A. Mass changes for the gold-coated quartz crystals modified with the surface capture probe upon addition of increasing concentration (in pM) of (a) target oligonucleotide captured onto AuNPs, (b) target oligonucleotide not linked to AuNPs, (c) control oligonucleotide linked to AuNPs, and (d) the control not linked to AuNPs. **B.** Mass changes shown for (a) control and (b) target oligonucleotides (0.5 pM) with or without linking to AuNPs. Data shown are mean ± standard deviations represented by error bars for N = 3 replicates. Relative standard deviations (RSDs) for the control were 17% with no AuNPs and 22% with AuNPs linkage. The RSDs for the target were 11% (no AuNPs) and 7% (with AuNPs).

The QCM showed a significant mass change when the crystal was exposed to MHOH, suggesting that this reagent has an efficient free surface blocking ability to minimize non-specific interactions. The AuNP bioconjugation with the target oligonucleotide amplified the mass changes by ~2.5 times in comparison to the hybridization signals without the AuNPs strategy (Fig. 4A–B). The small QCM signal responses for the control oligonucleotide suggest good selectivity and specificity for the surface capture probe to the target miRNA-21 mimic sequence. Even after linking with AuNPs, the responses were quite negligible in the control, which had five base pair mismatches relative to the target (~13 times less signal than the target). With the signal amplification strategy, we were able to detect the target concentrations from 0.05 to 50 pM.

4.3.3 Pixel intensity changes in the SPR microarray in response to target or control nucleotide hybridization with the surface capture probe.

Selective hybridization of the target over the control oligonucleotide with the surface capture probe coated on the SPR gold microarray was observed, similar to the mass sensor results. Figure 5 shows the real-time response plots of the SPR imager. Measurements were made from the new steady state baseline observed after washing the microarray surface with phosphate-buffered saline (PBS) for 10 minutes, which was sufficient to remove bulk and unhybridized oligonucleotides in solution.

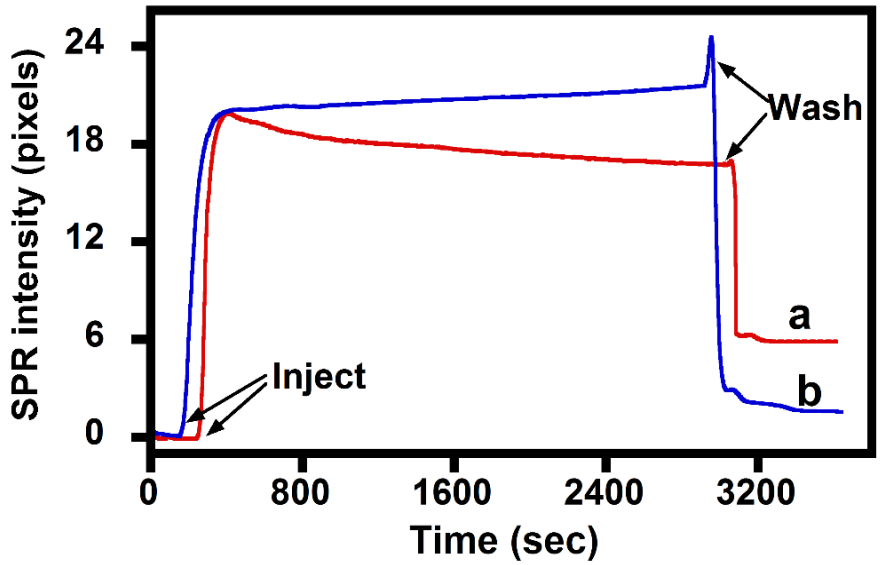

Figure 5. Real-time SPR response (average of eight array spots) for the binding of 0.5 pM of (a) target or (b) control oligonucleotide linked with AuNPs onto the surface immobilized capture probes at a flow rate of 50 μL/min. Sample injection and buffer wash points are labeled.

The blocking agent-treated SPR spots that contained only MHOH (Fig. 6) showed no nonspecific hybridization signals after exposure to the AuNP-linked target or control oligonucleotide. The dual-channel SPR microarray allowed measurement of the pixel intensity changes with the simultaneous introduction of similar concentrations of the target and control oligonucleotides. The observed changes in the pixel intensities for various concentrations of AuNP-linked target oligonucleotides (0.1 – 50 pM) are summarized in Figure 6 as 3D image representations, and line profiles. These data show that the small gold spot array surface with about 0.008 cm^2 of geometric area allows

sufficient immobilization of surface capture probe molecules to hybridize with the low concentration of target oligonucleotide.

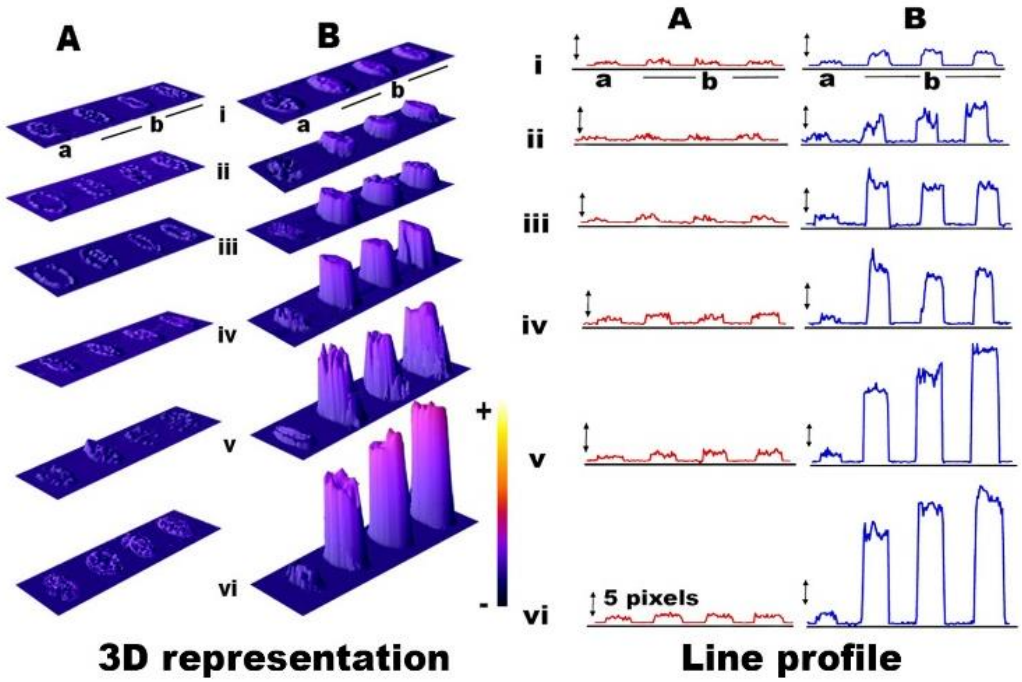

Figure 6. Representations of SPRi responses: the 3D representation (left) and the line profile (right) that depicts the SPR pixel intensities for various concentrations of target and control nucleotides. The spot labeled as (a) is the bare gold surface treated with 5 mM MHOH and that of (b) are the test spots containing the immobilized capture probes. (A)-b: control oligonucleotide of (i) 0.1, (ii) 0.5, (iii) 1, (iv) 10, (v) 30, and (vi) 50 pM concentrations conjugated with AuNPs; and (B)-b: target oligonucleotide of concentrations similar to those of the control allowed to bind with the surface capture probe.

The surface capture probe demonstrated excellent selectivity for the target oligonucleotide over the control oligonucleotide (with five base pair mismatches). The observed changes in the pixel intensities for the control spots were very low, illustrating that there was minimal non-specific interaction between the control oligonucleotide and the surface capture probe. The spots that were completely blocked with MHOH showed negligible non-specific binding to the target or the control oligonucleotide, suggesting no false-positive signals in the absence of the surface capture probe.

4.3.4 Comparison of QCM and SPRi methods

QCM is an excellent quantitation method, and it can provide high sensitivity and selectivity with use of an appropriate signal amplification strategy and surface chemistry. Results described herein are similar to those of our prior demonstration of an electrochemical QCM immunosensor for serum insulin measurements based on magnetic nanoparticle conjugation.[40] The double logarithmic response plot shown in Figure 7A shows a linear correlation (R^2=0.99) between the mass change and concentration of the target oligonucleotide. The limit of detection (LOD)[43,44] for QCM-based quantification was 28 fM, which is a promising detection level and indicates the uniqueness of the designed experimental conditions in achieving ultra-low detection resulting from minimal nonspecific and false-positive signals.

Although the QCM method provides sensitivity, quantitative details, and is useful for optimization of assay conditions, it is a low throughput approach (i.e., one sample at a time, and the most commonly available form is single quartz crystals). This is because designing a QCM crystal array is challenging due to engineering difficulties arising from the need to control piezoelectric properties across the array.[45,46] Better throughput can be achieved by using the SPR microarray strategy. The advantage of using the SPR microarray is that several concentrations can be studied on the same array platform without the need for multiple experiments. Thus, samples and controls can be analyzed in the same array in one experiment. Another advantage is that the required volume of samples is low (200 nL per SPR array spot are sufficient, whereas a QCM crystal needs several μL of sample). The use of AuNPs contributes to enhancement of the SPRi reflectivity changes due to the electronic coupling between the plasmons of AuNPs and that of the gold sensor surface upon hybridization of the nucleotides.[47,48] The LOD for the SPRi method in this study was 47 fM. Although this LOD is slightly higher than that of QCM, our assay in a microarray format displays a better throughput and similar sensitivity (Fig. 7B).

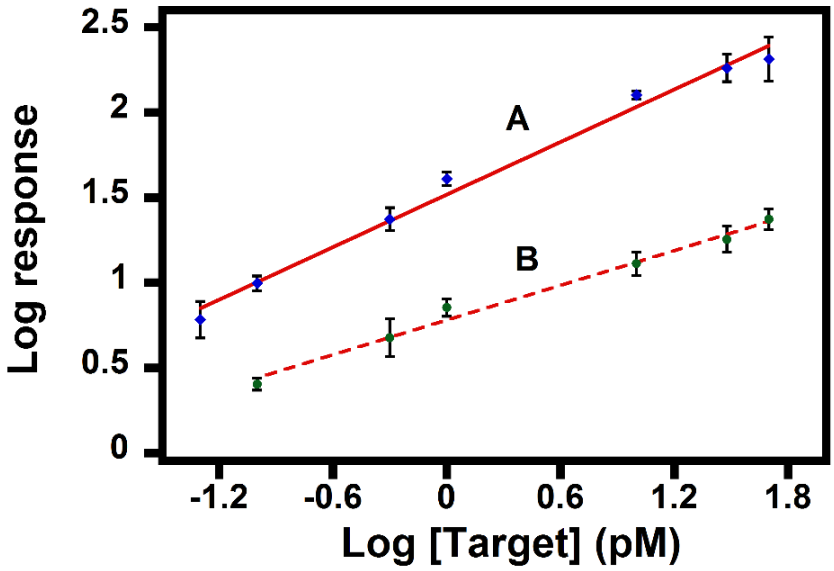

Figure 7. Double logarithmic calibration plots of **A.** QCM response (control response is subtracted) and **B.** SPRi response (control response is subtracted) upon hybridization of various concentrations of the AuNP-conjugated target oligonucleotide with the surface capture probe. (mean ± standard deviation for three replicates).

4.3.5 Assessment of selectivity

A recovery test was performed to evaluate the efficiency of the QCM and the SPRi microarray in detecting the AuNP-linked target oligonucleotide marker prepared in various concentrations of human serum. Prior to conjugation with AuNPs, 1 pM of the target and control oligonucleotides were suspended in different concentrations of human serum (10, 25, 50, and 75%) diluted in PBS solution (pH 7.4). A protocol similar to that described under the Experimental methods was followed to prepare AuNP-linked target or control oligonucleotides. Table 3 presents the sample recovery results for analyzing serum samples. Recovery was calculated as a percentage from the fraction of spiked nucleotide concentration detected after subtracting the control signals. The SPR microarray offered a reasonably good recovery until 25% serum was reached (> 90%), whereas for the QCM sensor analyte recovery (> 90%) was significantly affected above 10% serum. The results obtained suggest the likely applicability of calibration plots generated from buffer nucleotide

standards for the determination of nucleotide concentrations present in 10 - 25% serum samples. A lower dilution factor for serum sample analysis is preferred, as it would minimize dilution of the nucleotide marker in serum and facilitate easier detection when applied to patient samples.

Table 3. Analysis of the target oligonucleotide in different percentages of serum samples (diluted in PBS, pH 7.4) using the QCM and SPR microarray.

Serum %	**[Actual] (pM)**	**[Detected] from calibration (pM)**	**Recovery (%)**
QCM			
10	1.00	0.93	93%
25	1.00	0.82	82%
50	1.00	0.76	76%
75	1.00	0.67	67%
SPR microarray			
10	1.00	0.95	95%
25	1.00	0.93	93%
50	1.00	0.84	84%
75	1.00	0.64	64%

Table 4 provides a short comparative summary of previous studies that measured various nucleic acids using AuNPs as a source of signal amplification. Our SPR microarray (LOD: 47 fM) and QCM (LOD: 28 fM) results are better than or comparable with the detection levels reported in prior studies.

Table 4. Summary of recent studies related to nucleic acid detection.

Technique	**Tested molecules**	**Sample matrix**	**Detection limit**	**Ref.**
Multiplexed miRNA detection using AuNP-modified poly-T DNA hybridization SPR microarray	miRNA-16, miRNA-122b, miRNA-23b	0.3 M NaCl/ 10 mM phosphate buffer (pH 7.4)	10 fM	Fang *et al.*, 2006[49]
DNA sensing using catalytic growth of AuNP-enhanced SPR	cDNA, ssDNA	0.3 M NaCl/ 10 mM phosphate buffer (pH 7.0)	4.8 pM	Yang *et al.*, 2007[50]
AuNP-amplified SPR interfaces for the detection of mercury ions using hairpin DNA probes containing a 21mer T-rich Hg^{2+} binding sequence loop	Hairpin DNA	TE buffer (10 mM Tris–HCl, 50 mM NaCl, 1 mM EDTA, pH 8)	1 nM	Chang *et al.*, 2011[51]
Label free multiplexed detection of miRNA using silicon photonic microring resonator arrays	miRNA-24-1	PBS	150 fM	Qavi *et al.*, 2010[52]

Nanopore-based programmable oligonucleotide probe for circulating miRNA quantification	miRNA-155	1 M KCl buffered with 10 mM Tris (pH 8.0)	100 fM	Wang *et al.*, 2011[53]
Gold nanoprism based localized SPR sensor for miRNA detection	miRNA-21, miRNA-10b	PBS buffer (pH 7.4) and 40% human plasma	50 fM	Joshi *et al.*, 2014[54]
3D tetrahedral DNA nanostructure for DNA recognition and amplification by hybridization chain reaction using QCM	Synthetic DNA targets	TM buffer (10 mM Tris-HCl and 50 mM $MgCl_2$, pH 8.0)	0.1fM	Ge *et al.*, 2014[55]
Carboxy-polyethylene glycol microarray for AuNP-based detection of miRNA using differential interference contrast microscopy	let-7a let-7b let-7f let-7g	Saline sodium citrate	10 fM	Roy *et al.*, 2016[56]
Mass sensor SPR microarray	miRNA-21 mimic	Phosphate buffer (pH 7.4)	28 fM 47 fM	**This study**

4.4 Conclusions

We have designed highly sensitive sensors that provide a platform for detecting specific oligonucelotide biomarkers at femtomolar levels by linking them with AuNPs to enhance plasmonic sensitivity. The SPR microarray offers better throughput with a comparable LOD than a QCM sensor provides. Compared to the QCM sensor, the SPR microarray allows multiple experiments to be run with suitable controls using the dual-channel syringe pump system, minimizing assay time and offering improved precision. Thus, the SPR microarray approach is promising for clinical applications to accomplish early diagnosis, treatment, and monitoring of recurrence of diseases based on circulating miRNAs as biomarkers.

Author contributions

Gayan Premaratne performed the majority of experiments, data analysis and drafeted the manuscript. Zainab H. Al Mubarak contributed in performing the SPRi measurements. Lakmini Senavirathna provided support in designing the ssDNA sequences. Dr. Sadagopan Krishnan and Dr. Lin Liu provided thoughtful insights into the project and reviewed the manuscript.

4.5 References

1. J. Labuda, A.M.O Brett, G. Evtugyn, M. Fojta, M. Mascini, M. Ozsoz, I. Palchetti, E. Palecek, J. Wang, Electrochemical nucleic acid-based biosensors: concepts, terms, and methodology (IUPAC Technical Report), Pure. Appl. Chem. 82 (2010) 1116–1187.
2. S.D. Patil, D. G. Rhodes, D.J. Burgess, DNA-based therapeutics and DNA delivery systems: a comprehensive review. The AAPS journal 7 (2005) E61–E77.
3. Z. Shakoori, S. Salimian, S. Kharrazi, M. Adabi, R. Saber, Electrochemical DNA biosensor based on gold nanorods for detecting hepatitis B virus. Anal. Bioanal. Chem. 407 (2015) 455–461.
4. J.R. Urbez-Tones, P. Haag, P. Bowen, T. Lowery, D.T. O'Gorman, Development of a DNA macroarray for the detection and identification of fungal pathogens causing decline of young grapevines. Phytopathology 105 (2015) 1373–1388.
5. C. Frederickx, F.J. Verheggen, E. Haubruge, Biosensors in forensic sciences/Les biodétecteurs en sciences forensiques. Biotechnol. Agron. Soc. Environ. 15 (2011) 449–458.
6. M. Kasu, K. Shires, The validation of forensic DNA extraction systems to utilize soil contaminated biological evidence. Leg. Med. 17 (2015) 232–238.
7. M. Boeri, C. Verri, D. Conte, L. Roz, P. Modena, F. Facchinetti, E. Calabrò, C.M. Croce, U. Pastorino, G. Sozzi, MicroRNA signatures in tissues and plasma predict development and prognosis of computed tomography detected lung cancer. Proc. Natl. Acad. Sci. U.S.A., 108 (2011) 3713-3718.
8. Z. Hu, X. Chen, Y. Zhao, T. Tian, G. Jin, Y. Shu, Y. Chen, L. Xu, K. Zen, C. Zhang, H. Shen, Serum MicroRNA signatures identified in a genome-wide serum MicroRNA expression profiling predict survival of non–small-cell lung cancer. J. Clin. Oncol. 28 (2010) 1721-1726.

9. G.R.V. Pottelberge, P. Mestdagh, K.R. Bracke, O. Thas, Y.M.V. Durme, G.F. Joos, J. Vandesompele, G.G. Brusselle, MicroRNA expression in induced sputum of smokers and patients with chronic obstructive pulmonary disease. Am. J. Respir. Crit., 183 (2011) 898-906.
10. G. Liu, A. Friggeri, Y. Yang, J. Milosevic, Q. Ding, V.J. Thannickal, N. Kaminski, E. Abraham, miR-21 mediates fibrogenic activation of pulmonary fibroblasts and lung fibrosis. J. Exp. Med., 207 (2010) 1589-1597.
11. M.A. Cortez, G.A. Calin, MicroRNA identification in plasma and serum: a new tool to diagnose and monitor diseases. Expert. Opin. Biol. Ther. 9 (2009) 703–711.
12. G.Swaminathan, J.Martin-Garcia, S.Navas-Martin, RNA viruses and microRNAs: challenging discoveries for the 21st century. Physiol. Genomics, 45 (2013) 1035–1048.
13. P. T.Liu, M.Wheelwright,R.Teles, E. Komisopoulou, K.Edfeldt, B.Ferguson, M. D. Mehta, A. Vazirnia, T. H. Rea, E. N. Sarno, MicroRNA-21 targets the vitamin D-dependent antimicrobial pathway in leprosy. Nat. Med. 18 (2012) 267–273.
14. Y. Cheng, C. Zhang, MicroRNA-21 in cardiovascular disease. J. Cardiovasc. Trans. Res.3 (3) (2010) 251–255.
15. N. Yanaihara, N. Caplen, E. Bowman, M. Seike, K. Kumamoto, M. Yi, R. M. Stephens, A. Okamoto, J. Yokota, T. Tanaka, Unique microRNA molecular profiles in lung cancer diagnosis and prognosis. Cancer cell 9 (2006) 189–198.
16. C. I.Cheng, Y.-P.Chang,Y.-H. Chu, Biomolecular interactions and tools for their recognition: focus on the quartz crystal microbalance and its diverse surface chemistries and applications. Chem. Soc. Rev. 41 (2012) 1947–1971.
17. C. L. Wong, M. Olivo, Surface plasmon resonance imaging sensors: a review. Plasmonics 9 (2014) 809–824.
18. X. Wang, S. Zhan, Z. Huang, X. Hong, Review: advances and applications of surface plasmon resonance biosensing instrumentation. Instrum. Sci. Technol. 41 (2013) 574–607.

19. Y. Liu, Q. Liu, S. Chen, F. Cheng, H. Wang, W. Peng, Surface plasmon resonance biosensor based on smart phone platforms. Sci. Rep. 5 (2015) 12864.
20. M. Puiu, C. Bala, SPR and SPR imaging: Recent trends in developing nanodevices for detection and real-time monitoring of biomolecular events. Sensors 16 (2016) 870.
21. C. Lausted, Z. Hu, L. Hood, Label-free detection with surface plasmon resonance imaging. Protein Microarray for Disease Analysis: Methods and Protocols (2011) 321–333.
22. H. H. Nguyen, J. Park, S.Kang, M. Kim, Surface plasmon resonance: a versatile technique for biosensor applications. Sensors 15 (2015) 10481–10510.
23. J.M. Brockman, B.P. Nelson, R.M. Corn, Surface plasmon resonance imaging measurements of ultrathin organic films, Annu. Rev. Phys. Chem. 51 (2000) 41–63.
24. G. Spoto, M. Minunni, Surface plasmon resonance imaging: what next?, J Phys. Chem. Lett. 3 (2012) 2682–2691.
25. G. Li, X. Li, M. Yang, M. M. Chen, L. C. Chen, X. L. Xiong, A gold nanoparticles enhanced surface plasmon resonance immunosensor for highly sensitive detection of ischemia-modified albumin. Sensors, 13 (2013) 12794–12803.
26. E. E. Bedford, J. Spadavecchia, C. M. Pradier, F. X. Gu, Surface plasmon resonance biosensors incorporating gold nanoparticles. Macromol. Biosci. 12 (2012) 724–739.
27. Y. Li, A. W. Wark, H. J. Lee, R.M. Corn, Single-nucleotide polymorphism genotyping by nanoparticle-enhanced surface plasmon resonance imaging measurements of surface ligation reactions. Anal. Chem. 78 (2006) 3158–3164.
28. P.M. Tiwari, K. Vig, V.A. Dennis, S.R. Singh, Functionalized gold nanoparticles and their biomedical applications. Nanomaterials 1 (2011) 31-63.
29. J. B. Mills, E.Vacano, P. J. Hagerman, Flexibility of single-stranded DNA: use of gapped duplex helices to determine the persistence lengths of poly (dT) and poly (dA). J. Mol. Biol. 285 (1999) 245–257.

30. Y. Wang, T. Prokein, M. Hinz, H. Seliger, W. A. Goedel, Immobilization and hybridization of oligonucleotides on maleimido-terminated self-assembled monolayers. Anal. Biochem. 344 (2005) 216–223.
31. J. Z. Porterfield, A. Zlotnick, A simple and general method for determining the protein and nucleic acid content of viruses by UV absorbance. Virology 407 (2010) 281–288.
32. L. Soares, A. Csáki, J. Jatschka, W.Fritzsche, O. Flores, R. Franco, E. Pereira, Localized surface plasmon resonance (LSPR) biosensing using gold nanotriangles: detection of DNA hybridization events at room temperature. Analyst 139 (2014) 4964–4973.
33. K. C. Grabar, K. J. Allison, B. E. Baker, R. M. Bright, K. R. Brown, R. G. Freeman,A. P. Fox, C. D. Keating, M. D. Musick, M. J. Natan, Two-dimensional arrays of colloidal gold particles: a flexible approach to macroscopic metal surfaces. Langmuir 12 (1996) 2353–2361.
34. C. A. Mirkin, R. L. Letsinger, R. C. Mucic, J. J. Storhoff, A DNA-based method for rationally assembling nanoparticles into macroscopic materials. Nature 382 (1996) 607–609.
35. S. R. Nicewarner Peña, S. Raina, G. P. Goodrich, N. V. Fedoroff, C. D. Keating, Hybridization and enzymatic extension of Au nanoparticle-bound oligonucleotides. J. Am. Chem. Soc. 124 (2002) 7314–7323.
36. M. A. Hayat, Colloidal gold: principles, methods, and applications. Elsevier. (2012).
37. J. J. Storhoff, R. Elghanian, R. C. Mucic, C. A. Mirkin, R. L. Letsinger, One-pot colorimetric differentiation of polynucleotides with single base imperfections using gold nanoparticle probes. Journal of the American Chemical Society, 120 (1998) 1959–1964.
38. N. Bayat, V. R. Lopes, M. Sanchez-Dominguez, R. Lakshmanan, G. K. Rajarao, S. Cristobal, Assessment of functionalized iron oxide nanoparticles in vitro: introduction to integrated nanoimpact index. Environ. Sci. Nano. 2 (2015) 380–394.
39. V. Singh, S. Krishnan, Voltammetric immunosensor assembled on carbon-pyrenyl nanostructures for clinical diagnosis of type of diabetes, Anal. Chem. 87 (2015) 2648–2654.

40. V.Singh, S.Krishnan, An electrochemical mass sensor for diagnosing diabetes in human serum. Analyst 139 (2014) 724–728.
41. B. Della Ventura, M. Iannaccone, R. Funari, M. P. Ciamarra, C. Altucci, R. Capparelli, R. Velotta, Effective antibodies immobilization and functionalized nanoparticles in a quartz-crystal microbalance-based immunosensor for the detection of parathion. PloS one, 12 (2017) e0171754.
42. K. A. Marx, Quartz crystal microbalance: a useful tool for studying thin polymer films and complex biomolecular systems at the solution-surface interface. Biomacromolecules 4 (5) (2003) 1099–1120.
43. D. A. Armbruster, T.Pry, Limit of blank, limit of detection and limit of quantitation. Clin. Biochem. Rev. 29 (2008) S49–52.
44. F. T.Peters, O. H. Drummer, F. Musshoff, Validation of new methods. Forensic Sci. Int. 165 (2007) 216–224.
45. N. C.Speller, N. Siraj, S. Vaughan, L. N. Speller, I. M. Warner, Assessment of QCM array schemes for mixture identification: citrus scented odors. RSC Advances 6 (2016) 95378–95386.
46. K. Jaruwongrungsee, T. Maturos, P. Sritongkum, A. Wisitsoraat, M. Sangworasil, A. Tuantranont, Analysis of quartz crystal microbalance sensor array with circular flow chamber. Int. J.Appl. Biomed. Eng. 2 (2009) 51.
47. F. Salam, Y. Uludag, I. E. Tothill, Real-time and sensitive detection of Salmonella Typhimurium using an automated quartz crystal microbalance (QCM) instrument with nanoparticles amplification. Talanta 115 (2013) 761–767.
48. S. Elhadj, G. Singh, R. F. Saraf, Optical properties of an immobilized DNA monolayer from 255 to 700 nm. Langmuir 20 (2004) 5539–5543.

49. S. Fang, H. L. Lee, A. W. Wark, R.M. Corn, Attomole microarray detection of microRNAs by nanoparticle-amplified SPR imaging measurements of surface polyadenylation reactions. J. Am. Chem. Soc. 128 (2006) 14044–14046.
50. X. Yang, Q. Wang, K. Wang, W.Tan, H.Li, Enhanced surface plasmon resonance with the modified catalytic growth of Au nanoparticles. Biosen. Bioelectron. 22 (2007) 1106–1110.
51. C. -C. Chang, S. -Y. Lin, S. -C. Wei, C. -Y. Chen, C.-W. Lin, An amplified surface plasmon resonance "turn-on" sensor for mercury ion using gold nanoparticles. Biosen. Bioelectron. 30 (2011) 235–240.
52. A. J. Qavi, R. C. Bailey, Multiplexed detection and label-free quantitation of microRNAs using arrays of silicon photonic microring resonators. Angew. Chem. Int. Ed. 49 (2010) 4608–4611.
53. Y. Wang, D. Zheng, Q. Tan, M. X. Wang, L. Q. Gu, Nanopore-based detection of circulating microRNAs in lung cancer patients. Nat.Nanotech. 6 (2011) 668–674.
54. G. K. Joshi, S. Deitz-McElyea, M. Johnson, S. Mali, M. Korc, Sardar, R. Highly specific plasmonic biosensors for ultrasensitive microRNA detection in plasma from pancreatic cancer patients. Nano letters 14 (2014) 6955–6963.
55. Z. Ge, M. Lin, P. Wang, H. Pei, J. Yan, J. Shi, Q. Huang, D. He, C. Fan, X. Zuo, Hybridization chain reaction amplification of microRNA detection with a tetrahedral DNA nanostructure-based electrochemical biosensor. Anal. Chem. 86 (2014) 2124–2130.
56. S. Roy, J.H. Soh, J. Y. Ying, A microarray platform for detecting disease-specific circulating miRNA in human serum. Biosens. Bioelectron.75 (2016) 238–246.

CHAPTER 5

MULTIPLEXED SURFACE PLASMON ASSAY FOR SERUM PROTEINS AND MICRO-RIBONUCLEIC ACIDS: SIGNAL AMPLIFICATION BY BIMETALLIC Fe_3O_4@Au NANOPARTICLES

5.1 Introduction

To increase prediction rates by reducing false positive diagnoses based conventionally on a single marker analysis, it is important to measure a panel of key biomarkers. Highly expressed circulating protein and micro-ribonucleic acids (miRNA) markers have received increased attention in liquid biopsy studies due to their promising predictability feature.[1] Many analytical methods including enzyme-linked immunosorbent assay (ELISA), spectroscopic and molecular biology techniques (real-time polymerase chain reaction, northern blotting, microarray technology, and *in situ* hybridization) have been employed in cancer biomarker detection.[2,3]

In view of developing molecular technologies that enable more precise and objective decision making, surface plasmon resonance (SPR) spectroscopy with multiplexed imaging integrated with the advances in microfluidics is an attractive strategy. SPR is a highly sensitive surface analysis technique that can determine the binding events of various ligands to their respective receptors through refractive index changes.[4,5] Additionally, SPR can be used for high-throughput screening and to obtain real-time binding insights of biomolecular interactions by elegantly tuning the surface chemistries and metal-dielectric interfacial properties.[6-8] Due to these features, SPR methods have been widely employed for selective detection of various biomarkers.[9-11]

Incorporation of nanomaterials in bioassays offers the unique advantages of robustness due to superior chemical and solvent stability compared to light-sensitive labels, versatility to be adopted to various analytical techniques, and increased sensitivity and lowered detection limits. However, the compromise on the linear dynamic range for high sensitivity needs to be overcome for nanomaterial-based assays to measure various analyte concentrations in clinical samples.[12,13]

Among metal nanoparticles (NPs), the bimetallic NPs allow tuning of plasmonic and magnetic properties, and the core (inner component)/shell (outer component) class is one of the important types that combine the beneficial properties of the two different nanomaterials.[14,15] Different bimetallic combinations such as silver@gold, iron@platinum, platinum@cobalt, and gold@platinum have been designed for biosensing, bio-imaging, and drug delivery applications.[16] In particular, the magnetic properties of the iron-gold (Fe_3O_4@Au) bimetallic NPs offers the dual benefit of (i) easy conjugation and magnetic separation of desired compounds for subsequent detection in the assay;[17] and (ii) the plasmonic gold shell properties are useful for amplifying the surface plasmon detection signals.[18] In addition, the coating of Fe_3O_4 NPs with a gold material provides more dispersibility and room for various surface functionalization strategies (e.g., thiols, polymers, small molecules, dendrimers) for immobilizing biomolecules.[19,20] Brown *et al*. demonstrated the synthesis of homogeneous and larger NPs *via* a seeding method involving the reduction of gold salts by using either sodium citrate or hydroxylamine reagents.[21] Pham *et al.* magnetically separated IgG protein by gold-coated Fe_3O_4 NPs of 15-40 nm size.[17]

In this report, for the first time, we have devised a multiplexed SPR imager (SPRi) microarray utilizing Fe_3O_4@Au NPs to simultaneously measure two protein and two miRNA markers present in human serum. Greater plasmon enhancement signal in the imager by the synthesized Fe_3O_4@Au NPs over either Fe_3O_4 or Au NPs of similar sizes is demonstrated. To demonstrate the applicability of our SPRi bimetallic NP-based assay for health monitoring based on circulating biomarkers, we chose two interleukins (IL-6 and IL-8) and miRNAs (miRNA-21 and miRNA-155) as

representative biomolecules. These markers were detected by spiking them in 10% normal human serum.

IL-6 has been reported to be one of the major cytokines found in the tumor microenvironment and in the circulatory system, and it is found to be over-expressed in all types of tumors depicting their progression and severity.[22] At the same time, the serum concentration of IL-8 has been found to correlate with tumor burden, thus making it a useful pharmacodynamic-biomarker to detect responses to cancer immunotherapy.[23] Among the members of the miRNA family, miRNA-21 is one of the consistently upregulated circulatory biomarkers in cancer patients.[24] Similarly, the miRNA-155 is a robust oncogenic circulating miRNA, and its overexpression can indicate the promotion of tumorigenesis.[25] The circulating concentrations of miRNA-21 and miRNA-155 markers have the potential utility for early diagnosis and monitoring of tumors as well as for predicting chemoresistance.

Fe_3O_4@Au bimetallic NPs are employed as a signal amplification label on the SPRi platform to increase sensitivity and mitigate the responses arising from the non-specific interaction of other components in a serum sample. The designed sensor not only detects four biomarkers, but also offers kinetic information, which is vital to understanding the degree of interaction of the chosen receptors with the target analytes, and the analytical advantage of the designed assay strategy. Such an SPRi array platform represents a useful bioassay that can be well adapted for analysis of biomarkers present in clinical samples.

5.2 Experimental

5.2.1 Materials and chemicals

Thiol modified custom-designed DNA oligonucleotides and miRNAs (sequences presented in Table 1), bovine serum albumin (BSA), dithiothreitol (DTT), 6-mercaptohexanol (MHOH), 3-mercaptopropionic acid (MPA), ethyl-3-[3-dimethylaminopropyl]carbodiimide hydrochloride

(EDC), and *N*-hydroxysuccinimide (NHS), gold(III) chloride trihydrate ($HAuCl_4.3H_2O$), sodium borohydride, sodium citrate, gold and iron standards for ICP analysis (1000 ppm) were obtained from Sigma-Aldrich (St. Louis, MO). Recombinant IL-6 and IL-8 proteins, and purified anti-human IL-6 and IL-8 sandwich antibodies (the surface-immobilized antibody is monoclonal and the bimetallic NP-attached detection antibody is polyclonal) were purchased from BioLegend Inc., (San Diego, CA). The human serum samples were purchased from Fitzgerald Industries International Inc., (North Acton, MA). Citrate-stabilized magnetic nanoparticles (Fe_3O_4 NPs, 50 nm hydrodynamic diameter) were purchased from Chemicell GmbH Inc., (Berlin, Germany). Ultrapure deionized water (DI water) and NAP-10 columns were obtained from GE Healthcare (Cranbury, NJ). SpotReady-16 gold spotted glass microarray chips (spot size 1 mm diameter, SPR-1000-016) were obtained from GWC Technologies (Madison, WI).

Table 1. Sequences of the custom-designed DNA oligonucleotides employed in this study. (In the hairpin capture DNA, the sequences in italics (underlined) are complementarity to the target miRNA sequence, the sequences in bold are the hairpin forming sequence, and those highlighted in gray are complementary to the sequence of the bimetallic NPs attached detection DNA. The detection DNA partially hybridizes with the exposed region of the hairpin surface DNA when pre-hybridized with the miRNA marker)

miRNA-21	5'*UAGCUUAUCAGACUGAUGUUGA*3'
Hairpin capture DNA for miRNA-21	5'SH-$(CH_2)_6$-**ATTGAA**TCGAG*TCAACATCAGTCTGATAAGCTA*TGCATAGC**TTC AAT**-$(CH_2)_3$-$NH_2$3'
miRNA-155	5'*UUAAUGCUAAUCGUGAUAGGGGU*3'
Hairpin capture DNA of miRNA-155	5'SH-$(CH_2)_6$-**ATTGAA**TCGAG*ACCCCTATCACGATTAGCATTAA*TGCATAGC**TTC AAT**-$(CH_2)_3$-$NH_2$3'
Detection DNA (Fe_3O_4@Au NP bound)	5'SH-$(CH_2)_3$–TTTTTTTTTTTTTGATTGAAGCAT3'

5.2.2 Instrumentation

The optical measurements were made using a SPRimagerII array instrument at room temperature (Horizon SPR imager model) operating at a SPR source wavelength of 800 nm (GWC Technologies, Madison, WI, USA). The experiments were conducted using our custom designed four channel microfluidics set-up, each connected to a syringe pump (100 µL sample loop, New Era Pump System, Inc., NY, USA). The SPRi pixel intensities for increased miRNA or IL concentrations upon binding to their surface-immobilized selective receptors followed by signal amplification from the binding of Fe_3O_4@Au NPs linked detection probes were measured. Digital Optics V++ software package provided in the instrument was used to collect the SPRi difference images (i.e., differences of the pixel intensities before and after the binding events), and the 3D-images were represented using ImageJ 1.49v software (NIH, USA).

Quantification of oligonucleotides was done by a Nanodrop ND1000 spectrophotometer (Thermo Scientific, Waltham, MA). The UV-vis spectral absorbance of antibodies and DNA oligonucleotides was measured at 280 and 260 nm, respectively.[26] The elemental analysis of the Fe_3O_4@Au NPs was performed by an inductively coupled plasma optical emission spectrophotometric analyzer (ICP-OES, SPECTRO Analytical Instruments Inc., NJ, USA). The emission line selected for the Fe was 259.9 nm, and for Au, the line was 267.5 nm.[27]

Transmission electron microscopy (TEM, JEOL JEM-2100) images of the synthesized Fe_3O_4@Au NPs were obtained by preparing drop-coated samples on carbon surface grids. Surface characterization of the gold microarray before and after coating with the surface capture DNA, after hybridizing with the miRNA marker, and subsequently, with the plasmon enhancing Fe_3O_4@Au NPs linked detection probes was conducted by scanning electron microscopy (SEM, Model: FEI Quanta 600FE). An accelerating voltage of 20 kV was applied. The images were acquired using the FEIxT Microscope Control Software. The hydrodynamic diameter and surface charges of

Fe_3O_4@Au NPs covalently attached with the detection antibody or DNA were measured using a ZetaPALS potential analyzer (Brookhaven Instruments Corporation, Holtsville, NY, USA).

5.2.3 Synthesis and characterization of Fe_3O_4@Au bimetallic nanoparticles

By adopting a seed growth technique derived from the process called Ostwald ripening, gold NPs coated onto Fe_3O_4 NPs were synthesized (Figure 1).[28] During this process, the continuous growth of the gold layer will take place on the surface of Fe_3O_4 NPs. This will cause the bimetallic NPs to significantly grow in size. A reaction flask containing $HAuCl_4.3H_2O$ (10.3 mg/mL, 5 mL), sodium citrate (59.3 mg/mL, 5 mL), Fe_3O_4 NPs (25 mg/mL, 0.5 mL) and 25 mL of H_2O was refluxed at 100 ^oC for 10 min. A freshly prepared mixture of $HAuCl_4.3H_2O$ (4.53 mg/mL, 10 mL), Fe_3O_4 NPs (0.12 mg/mL, 10 mL), and sodium citrate (22.55 mg/mL, 10 mL) was then added to the reaction flask as 1 mL aliquots for every 2 min at 90 ^oC. This secondary addition of the reaction mixture controls the size of the outer Au shell formed around the Fe_3O_4 NPs.

Synthesized nanoparticles were characterized to determine their physical and chemical properties. The Fe_3O_4@Au NPs were compared with similarly sized Au NPs or Fe_3O_4 NPs to estimate the relative SPRi signal enhancement property.

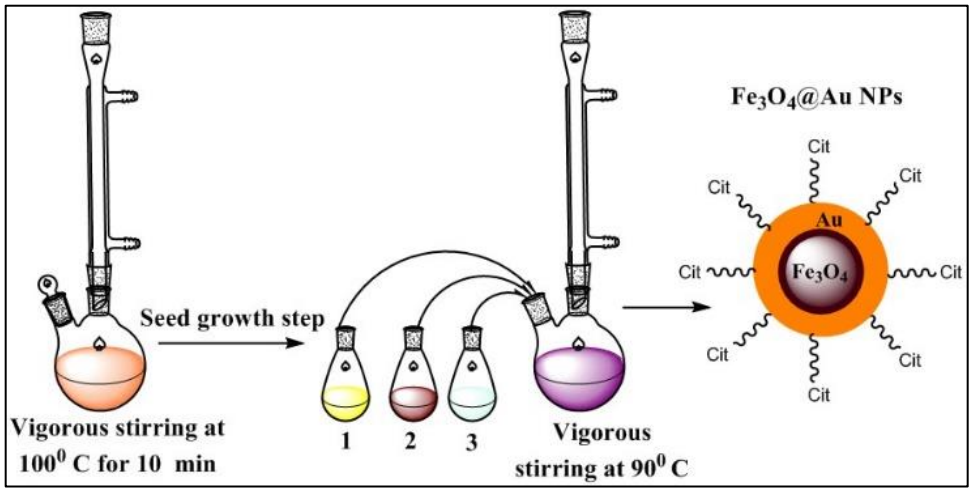

Figure 1. Schematic illustration of the synthesis of Fe_3O_4@Au bimetallic NPs using the reaction mixture consisting of **1.** $HAuCl_4.3H_2O$, **2.** Fe_3O_4 NPs, and **3.** sodium citrate.

5.2.4 Preparation of the covalent conjugates of Fe_3O_4@Au NPs with detection antibodies

The surface lysine residues of IL-6 and IL-8 second antibodies were attached to the carboxylic acid groups of citrate molecules adsorbed around Fe_3O_4@Au NPs using a protocol employed in our previously reported studies.[29-31] Briefly, the Fe_3O_4@Au NPs were suspended in freshly prepared aqueous solution containing EDC (0.35 M) and NHS (0.1 M) and allowed to incubate for 20 min to create the easily leaving *N*-succinimidyl ester units of the carboxyl groups. The NPs were separated magnetically by using a magnet to remove the unreacted EDC/NHS solution. The particles were then washed twice with phosphate buffered saline (PBS), magnetically separated after each wash, and resuspended in PBS (pH 7.4). A freshly prepared antibody solution (200 µL of 5 µg mL^{-1} in pH 7.4 phosphate buffer) was immediately added to the NP solution. The covalent attachment of antibodies to NPs was carried out for 1 h at room temperature with a continuous gentle mixing of the reaction tubes in an incubator (Labnet International Inc.,). Covalently attached Antibody-Fe_3O_4@Au conjugates were separated from the free antibody solution by the magnet and the conjugates were washed twice in PBS, resuspended in a 200 µL of a fresh PBS solution before using for SPR studies.

5.2.5 Preparation of the conjugates of Fe_3O_4@Au with detection DNA molecules

Initially, to prepare the DNA oligonucleotide linked to Fe_3O_4@Au NPs, a protocol provided by the manufacturer (Sigma-Aldrich) was followed to reduce the disulfide-modified oligonucleotide for thiol-activation. For this, the dry oligonucleotide sample was treated with an aqueous solution of DTT (100 mM) at 10:1 ratio (µL DTT to A260 units of oligonucleotides) and incubated for 1 h at room temperature. A NAP-10 column, pre-equilibrated with approximately 15 mL of 50 mM sodium phosphate buffer (pH 6.0), was used to remove DTT and any other irrelevant impurities. The concentration of the purified detection oligonucleotide was determined by measuring absorbance at 260 nm using a NanoDrop spectrophotometer (1 mm path length light source; CCD

array detector) and the molar extinction coefficient of the detection oligonucleotide sequence ($\varepsilon_{detection}$: 227.8 $mM^{-1}cm^{-1}$, Sigma-Aldrich).

DNA-Fe_3O_4@Au conjugates were prepared by chemisorbing the thiol-activated oligonucleotides according to our previously described method with slight modifications.[32] In short, 500 µL of 2 µM detection DNA oligonucleotide solution prepared in sodium phosphate buffer (pH 6.0) was mixed with 250 µL of Fe_3O_4@Au solution and incubated with gentle mixing for 4 h at 37 °C. Upon completion of incubation, 250 µL of 1 M NaCl/0.1 M sodium phosphate buffer (pH 7.4) and 500 µL of distilled water were added and incubated for 24 h at 37 °C. The high salt 1 M NaCl/0.1 M sodium phosphate buffer (pH 7.4) solution favors the thiolated DNA to adsorb well on to the gold surface of Fe_3O_4@Au NPs.[33] Following this, the DNA-Fe_3O_4@Au conjugates were magnetically separated from the supernatant and were rinsed twice with 0.3 M NaCl/0.1 M sodium phosphate buffer (pH 7.4) and brought to the original volume of 500 µL with PBS (pH 7.4), prior to use in the assay. The low salt 0.3 M NaCl/0.1 M sodium phosphate buffer (pH 7.4) prevents the irreversible growth of the Fe_3O_4@Au NPs after linking to DNA.[33]

5.2.6 Preparation of the four-channel microarray and multiplexed analysis

Eight spots on the SPRi gold array chip were incubated in 100 mM of MPA solution in ethanol for 12 h to form a self-assembled monolayer with free carboxyl surface groups. The chip was then washed thoroughly with DI water and dried under nitrogen. Following the EDC/NHS activation, the spots were rinsed with DI water and air-dried. The capture antibody of IL-6 or IL-8 (0.25 µL of 1 µg mL^{-1} per spot) was placed on four spots of the gold array. Similarly, the thiol-activated hairpin capture DNA of miRNA-21 or miRNA-155 (0.25 µL of 1 µM solution per spot) was placed on four spots of the gold array.

The capture molecules were immobilized for a duration of 1 h in a moist, cold environment (4 °C, Figure 2). The free surface of the oligonucleotide-coated spots was blocked using 5 mM MHOH

for 30 min and the chip was washed with PBS (pH 7.4) to minimize non-specific binding interactions.

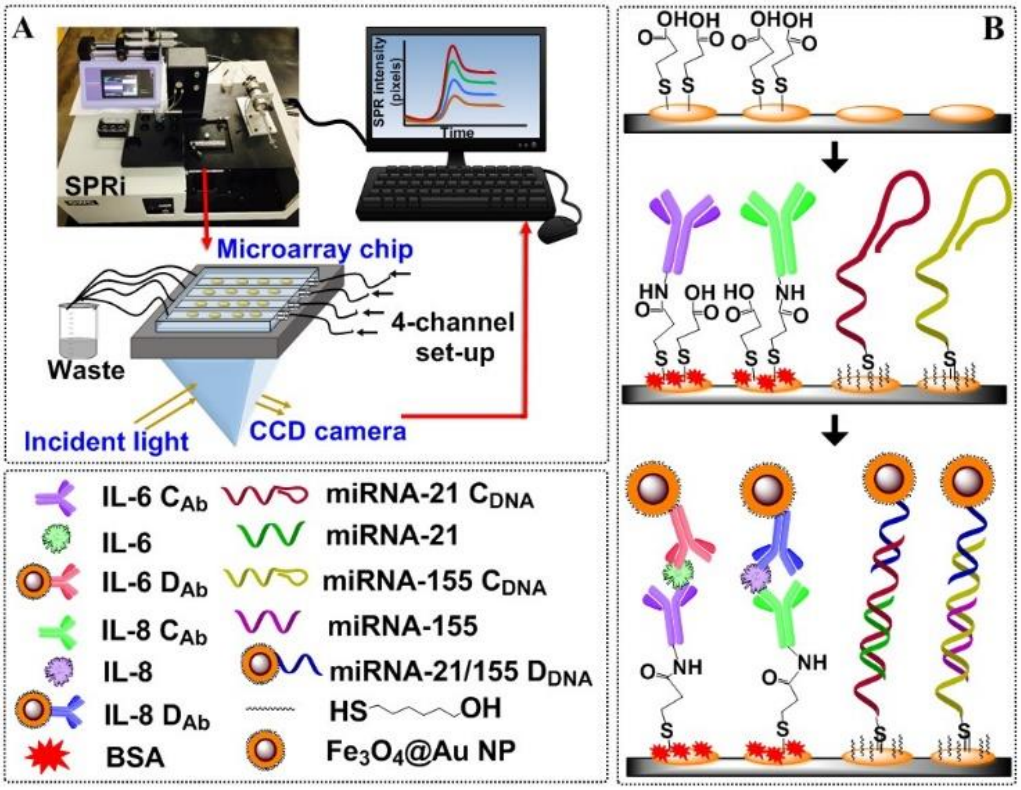

Figure 2. A. The experimental set-up for multiplexed SPRi analysis using a four-channel flow injection system. **B.** The SPRi chip was modified with capture probes (C_{Ab}: capture antibodies or C_{DNA}: capture DNA) and the analytes were assayed as follows: Two lanes (4 spots each) of the SPRi microarray were self-assembled with a monolayer of MPA. The remaining two lanes were self-assembled with thiol-activated hairpin capture DNAs of miRNA-21 and miRNA-155 (4 spots each) followed by blocking the free surface with MHOH. The IL-6 and IL-8 capture antibodies were covalently attached to the -COOH activated MPA surface (4 spots each) followed by blocking of the free surface with 1% BSA. Various concentrations of the protein and miRNA markers were spiked in 10% human serum and allowed to bind their respective capture molecules on the chip using the designated individual flow channels. The signal amplification step of the bioassay was subsequently followed by introducing the respective detection molecules (D_{Ab}: detection antibodies or D_{DNA}: detection DNA) conjugated to Fe_3O_4@Au NPs yielding detection DNA-Fe_3O_4@Au or detection antibody-Fe_3O_4@Au NPs.

The modified chip was immediately assembled on to the SPRi four-channel flow system with a layer of index matching fluid between the free glass side of the chip that will be in contact with the prism (Cargille Labs, NJ, USA). Each channel was connected to a sample injector unit and a syringe pump. Real-time measurements were performed using the running buffer, PBS (pH 7.4).

Initially, the running buffer was pumped at a flow rate of 50 μL min^{-1}, and a reference image of the array was taken at first. The sample injector loops (100 μL volume) were then separately filled with known concentrations of IL-6, IL-8, miRNA-21, or miRNA-155 solutions spiked in 10% normal human serum in PBS (pH 7.4), and allowed to pass onto the capture molecule modified arrays for 45 min. Upon completion of the incubation, the chip surface was washed for 10 min with the running buffer to remove all unbound molecules. Then 100 μL of Fe_3O_4@Au NPs conjugated to detection molecules were introduced and incubated for 30 min, and washed with running buffer for 10 min before measuring the net pixel intensity changes. A control experiment was conducted by treating the capture probe-modified microarray with only 10% serum to obtain the background signals.

The final images of the microarray were acquired using a CCD camera. The difference images taken before and after each assay step are represented in a 3D format using ImageJ software (1.49v, NIH, USA). Multiplexing provided room for the analysis of four biomarkers in a single assay and minimized multiple experiments due to the microarray platform.

5.3 Results and Discussion

5.3.1 Hydrodynamic size and zeta potential of Fe_3O_4@Au NPs and conjugates

The average hydrodynamic diameter of the synthesized Fe_3O_4@Au NPs and its conjugates with the detection molecules (second antibody or oligonucleotide) were determined by the dynamic light scattering (DLS) method (Table 2). A total of five measurements were made at a 90^o angle (2 min per measurement). The samples were diluted five times prior to measurements in PBS (pH 7.4).

The antibodies contain free surface lysine residues to covalently attach them to the surface carboxyl groups on Fe_3O_4@Au NPs with random orientations, and no additional steps were implemented for orienting the antibodies.[34]

The average size of the Fe_3O_4@Au NPs increased by about 25 nm after the antibody attachment. This is consistent with the typical hydrodynamic size of the antibodies (10 to 15 nm).[35] A similar size increment was observed upon chemisorption of thiol-activated DNA to the Fe_3O_4@Au NPs. The polydispersity index was ≤ 0.2 indicating good dispersion and narrow size distributions of the conjugated NPs in the buffer medium, which is likely the result of surface charge repulsions.

Table 2. The hydrodynamic diameters and ζ-potentials of Fe_3O_4@Au NPs and their conjugates with a detection antibody (shown here for IL-6 second antibody) or a detection DNA probe.

Parameter	**Fe_3O_4@Au NPs**	**Antibody-Fe_3O_4@Au**	**DNA-Fe_3O_4@Au**
Hydrodynamic diameter (nm)	105 ± 6	132 ± 11	124 ± 5
Polydispersity index	0.19 ± 0.03	0.18 ± 0.05	0.15 ± 0.01
ζ potential (mV)	-38 ± 4	-12 ± 1	-51 ± 3

The ζ-potential was calculated by phase analysis of light scattering (PALS) that determined the electrophoretic mobility of the particles by Smoluchowski's equation available with the instrument software. Diluted samples were used to measure the ζ-potential of the NPs and conjugates for a total of 10 measurements with each measurement lasting for 30 seconds (Table 2). The negative ζ-potential measured for the unconjugated NPs is due to the citrate surface groups. The anti-IL antibodies are members of an IgG class and they typically bear an isoelectric point (pI) of 8-9.5[36] and hence a net positive charge at pH 7.4. This is in agreement with the significant shift in the positive ζ-potential for the detection antibody attached Fe_3O_4@Au NPs. The intrinsic negative charge of nucleotides[37] due to their phosphate groups shifted the ζ-potential of Fe_3O_4@Au NPs to more negative values (Table 2).

5.3.2 Elemental composition of the Fe_3O_4@Au NPs

One mL of a solution of Fe_3O_4@Au NPs (3 mg/mL) was digested for 4 h in 9 mL of HNO_3:HCl (1:3) acid mixture in a hot-water bath.[38] Upon completion of the digestion, the samples were diluted to 25 mL volume with deionized water. The Fe and Au standard solutions (0.5 to 100 ppm) were prepared by diluting the stock solutions (1000 ppm) in DI water. A calibration curve was developed using the standard solutions prior to analyzing the digested Fe_3O_4@Au NPs nanoparticle samples (N = 3). The percentage composition of Fe and Au was found to be 21.5 ± 0.4 ppm (91%) and 2.1 ± 0.1 ppm (9%), respectively.

5.3.3 Estimation of SPRi signal amplification by Fe_3O_4@Au NPs over Fe_3O_4 or Au NPs of similar sizes

To determine the SPRi signal amplification, the pixel intensities of Fe_3O_4 NPs (100 nm), Au NPs (100 nm), and the synthesized Fe_3O_4@Au NPs (75 nm) or Fe_3O_4@Au NPs (105 nm) were compared, similar to that reported previously.[39] In brief, the SPRi microarray was coated with a polycationic layer, polyethyleneimine (PEI, 0.1 mg mL^{-1} in DI water), by adsorbing for 30 min, and washed with DI water. The negatively charged citrate-stabilized NPs were then adsorbed for 30 min on the polymer coated spots and rinsed with DI water to remove any unbound NPs. The difference image obtained (before and after the coating with NPs) was processed by ImageJ software to obtain 3D representations (Figure 3).

The pixel intensities for the synthesized Fe_3O_4@Au NPs (75 nm) were 9-times and 4-times higher than Fe_3O_4 (100 nm) NPs and Au NPs (100 nm) alone, respectively. The increase in the Au shell size in the case of 105 nm Fe_3O_4@Au NPs further increased the SPRi pixel intensity to ~ 11-times and 6-times over the Fe_3O_4 (100 nm) and Au NPs (100 nm) alone, respectively. This could be attributed to the spectral overlap of the surface plasmon resonance in the Au shell with an intrinsic

electronic transition with the Fe_3O_4 core.[18] The results provide evidence for the Au shell containing bimetallic NPs for enhancing the plasmon resonance.

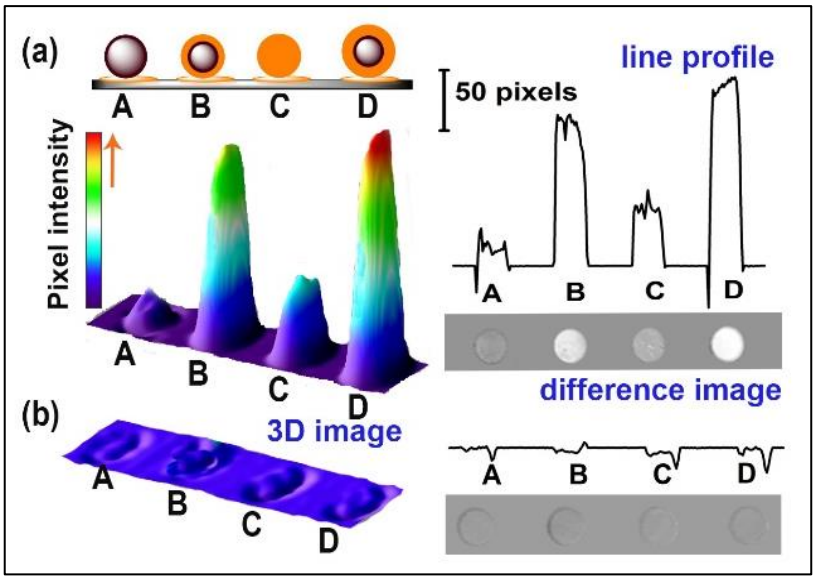

Figure 3. The SPRi responses of A. 100 nm Fe_3O_4 NPs, B. 75 nm Fe_3O_4@Au NPs, C. 100 nm Au NPs, and D. 105 nm Fe_3O_4@Au NPs adsorbed onto 0.1 mg mL^{-1} PEI coated gold surface. (a) Schematic and experimental 3D images of SPR pixel intensity, (b) only the PEI adsorbed gold surface. The corresponding line profiles and difference images (in grey) are shown on the right.

5.3.4 Microscopic characterization of the NPs and surface binding event of the conjugates made with detection probes

Figure 4A represents the TEM image of synthesized Fe_3O_4@Au NPs. The particles assumed nearly a spherical shape with an observable lighter Au layer around the darker Fe_3O_4 centers. The smaller size observed compared to the hydrodynamic diameter is due to the dried samples under the high vacuum conditions applied in the electron microscopic imaging.[29] Figures 4B to 4D are the SEM images obtained for the smooth gold surface of the microarray, the capture antibody/antigen/detection antibody-Fe_3O_4@Au NP complex for IL-6 protein, and the hairpin capture DNA /miRNA/detection DNA-Fe_3O_4@Au NP complex of miRNA-155, respectively.

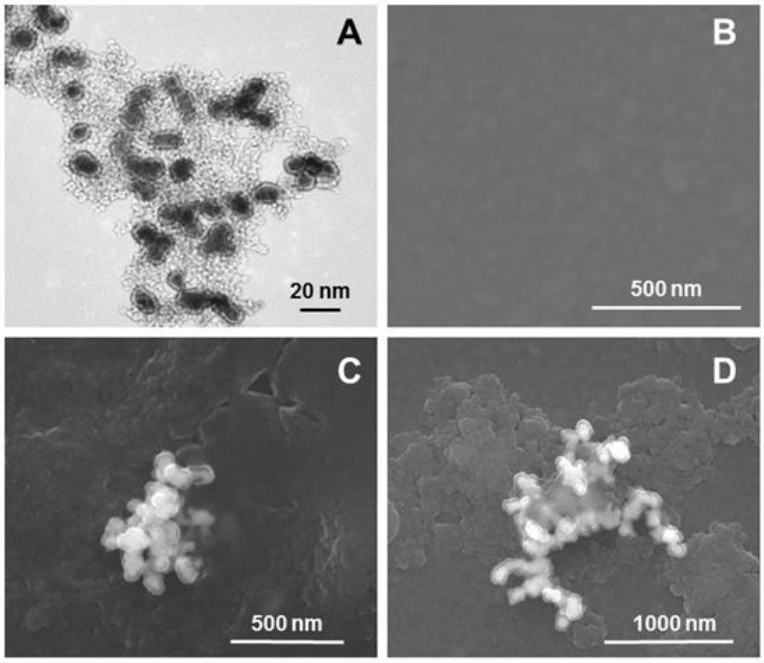

Figure 4. TEM image of A. Fe_3O_4@Au NPs. SEM images of B. bare Au surface of the microarray, C. IL-6 capture antibody/IL-6/Fe_3O_4@Au NP-IL-6 detection antibody assembly, and D. miRNA-155 capture DNA/miRNA-155/Fe_3O_4@Au NP-miRNA-155 detection DNA assembly.

5.3.5 Quantitation of capture and detection molecules used in the designed SPRi microarray for multiplexed detection of miRNAs and ILs

The fabricated microarray followed the sandwich type immunoassay strategy for IL detection and a dual hybridization of the hairpin capture DNA for selectively capturing the target miRNA marker from serum and detection with Fe_3O_4@Au NPs carrying the detection nucleotide. The spectrophotometric quantification of the amount of capture DNA self-assembled on the microarray surface and the number of detection probes attached to Fe_3O_4@Au NPs is presented in Table 3. This quantitation confirmed the successful immobilization on the desired surfaces.

Table 3. The quantitation of capture molecules immobilized on the microarray and detection molecules conjugated to the Fe_3O_4@Au NPs.

Molecules used for conjugation		Amount of molecules added (pmol)	Amount of molecules attached (pmol)	Average immobilization efficiency (%)
Surface immobilized biomarker capture molecules	IL-6 capture antibody	0.013 ± 0.002	0.008 ± 0.001	61 ± 10
	IL-8 capture antibody	0.013 ± 0.002	0.008 ± 0.002	60 ± 11
	miRNA-21 capture DNA	200 ± 38	155 ± 18	77 ± 17
	miRNA-155 capture DNA	200 ± 30	158 ± 15	79 ± 14
Fe_3O_4@Au NPs	IL-6 detection antibody	16.6 ± 3.5	12.3 ± 1.8	74 ± 18
	IL-8 detection antibody	16.7 ± 2.3	11.8 ± 1.5	71 ± 13
	miRNA-21/155 detection DNA	1000 ± 118	817 ± 52	82 ± 11

5.3.6 Real-time analysis of serum biomarkers

The real-time sensograms, difference images, 3-D representations, and line profiles corresponding to the multiplexed detection of ILs and miRNAs spiked in 10% human serum are presented in Figure 5. The detection probes conjugated to Fe_3O_4@Au NPs increased the SPRi responses by about 2-fold for the ILs and 8-times for the miRNAs. This can be attributed to the additional selective biological interaction and the NP-induced plasmon signal enhancements.

Figure 6 presents the linear response plots of SPRi signals subtracted for the signals resulted from the control serum sample. An increase in the SPRi responses for increased concentration of analytes spiked in to the serum confirms the specificity of the surface capture probes towards the target analytes of interest. IL-6 and IL-8 demonstrated a linearity from 20 pM – 100 nM and 10 pM

– 75 nM (~10^4 orders of magnitude), respectively. A wider dynamic range was observed for miRNA-21 and miRNA-155 from 50 fM – 2 nM and 25 fM – 4 nM (~10^8 orders of magnitud), respectively

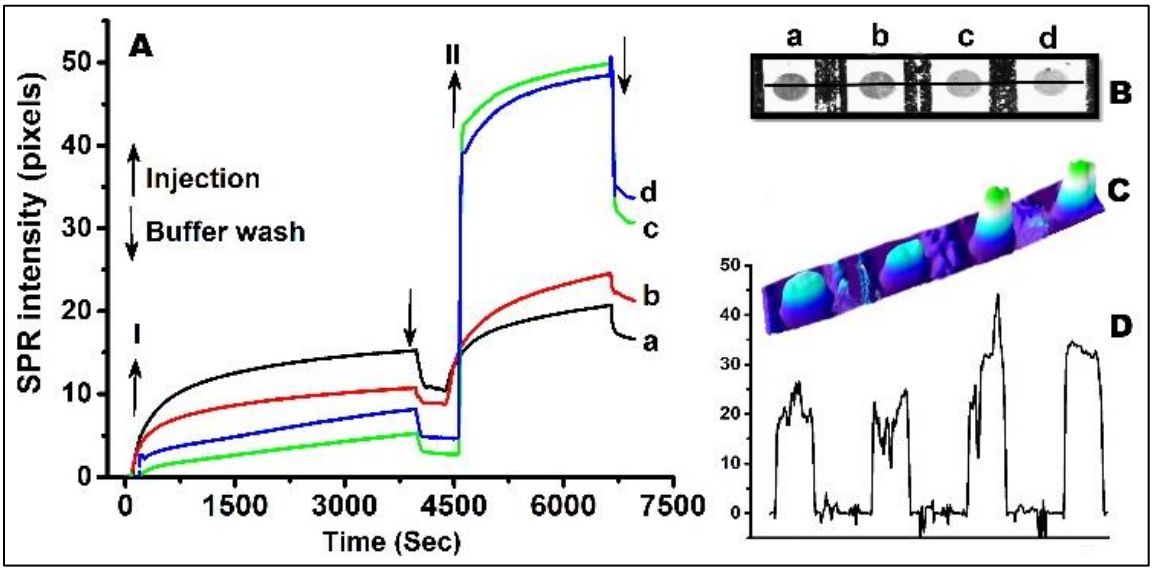

Figure 5. SPRi responses for a multiplexed assay by the 4-channel flow injection analysis **A.** Real-time pixel intensity changes for 10% serum spiked with a. IL-8 (10 nM), b. IL-6 (10 nM), c. miRNA-21 (0.25 nM), and d. miRNA-155 (0.25 nM). I. Represents the introduction of the 10% serum spiked with the markers to the capture probe coated microarray and II. represents the introduction of the detection probes conjugated to Fe_3O_4@Au NPs. **B.** Final difference image of the test spots after detection of protein and miRNA markers in a single microarray. **C** and **D.** Corresponding 3-D representation and line profile, respectively.

The observed differences in the dynamic range may be due to variations in the functionalization of the SPRi chip with capture probes and the sizes of the markers. The smaller self-assembled monolayer of capture miRNAs can be immobilized at greater densities than the larger antibodies of ILs. Thus, the sensitivities of miRNA detection were ~ 4-times greater than those for the ILs. Additionally, the hairpin capture DNA probes consist of a stem-loop oligomer structure that is structurally constrained, which thermodynamically increases the specificity of the target miRNA compared to a linear DNA probe.[40] The hairpin opens up only in the presence of the target to form a duplex with the highly specific complementary nucleotide sequence present in the loop. The

hairpin DNA probes can recognize nucleotide targets even with a single-nucleotide polymorphism.[41]

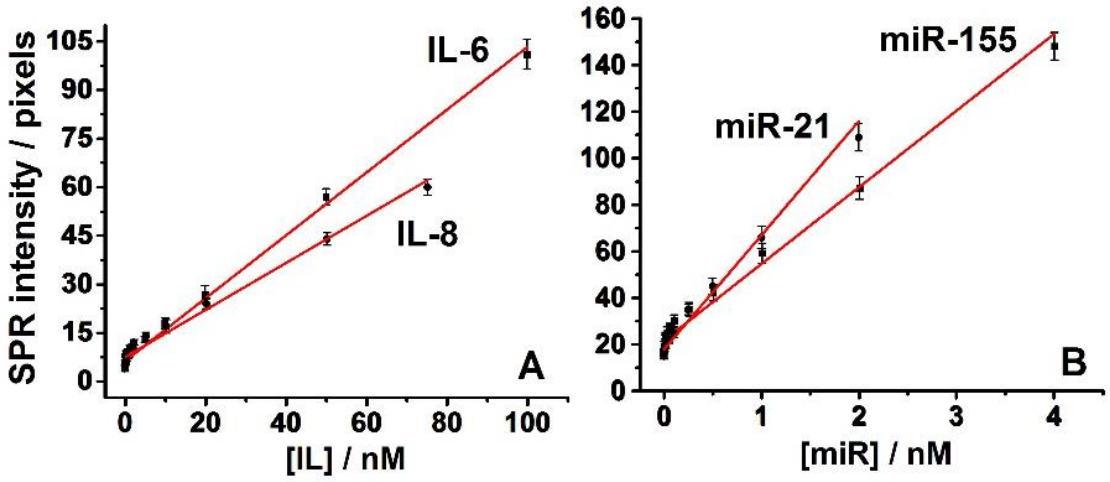

Figure 6. SPRi calibration plots for **A.** protein markers (IL-6 and IL-8) and **B.** miRNA markers (miRNA-21 and miRNA-155) in 10% human serum. (N = 3 replicates).

The detection limits (DLs) for miRNAs and ILs were calculated by the following equation: DL = 3 x standard deviation of the control/slope of the regression line. The DLs for IL-6, IL-8, miRNA-21, and miRNA-155 were 28 pM, 18 pM, 502 fM, and 483 fM, respectively. These DLs and dynamic ranges were compared to those of other recent SPR assays that detected protein or miRNA biomarkers in various matrices using different amplification strategies (Table 4). Our methodology is unique in quantifying the serum protein and miRNA biomarkers through a multiplexed detection format. The higher DLs resulted when measurements are carried out in serum medium over a simple buffer solution can be understood from Table 4 data for miRNAs and proteins.

5.3.7 Analysis of binding strength of protein and miRNA markers

Determining binding kinetics is an important parameter to assess the strength of inteactions between the markers and their receptors on the designed assay surface. Additionally, we can use the binding constants as the quality control parameter to reproducibly make and use the bioassays for reliable large-scale applications.

The Langmuir adsorption isotherm was followed to determine the equilibrium dissociation kinetics based on a 1:1 bimolecular interaction model,[42] where T is the target biomolecule and P is the surface capture probe involving the following binding event forming the complex, TP (eq 1):

$$T + P \underset{k_d}{\overset{k_a}{\rightleftharpoons}} TP \qquad (1)$$

If Γ is the surface concentration of the TP complex and Γ_{max} is the total concentration of binding sites available on the surface for the biomarkers, the adsorption (k_a) and desorption (k_d) kinetics can be described by eq 2,

$$\frac{d\theta}{dt} = k_a(1-\theta)[T] - k_d\theta \qquad (2)$$

At equilibrium, the relative surface coverage ($\theta = \Gamma/\Gamma_{max}$) reaches a steady state ($d\theta/dt = 0$), and θ can be expressed by eq 3,

$$\theta = \frac{K_{ads}C}{1+K_{ads}C} \qquad (3)$$

Γ_{max} can be related to the maximum signal upon saturating all the binding sites of the surface capture probes. C is the concentration of biomarkers and K_{ads} is the Langmuir adsorption coefficient ($K_{ads} = k_a/k_d$).

Figure 7 shows the plots of relative surface coverage (θ) plotted against the tested concentrations of each biomarker. The data points were fit to a Langmuir isotherm (eq. 2) using OriginPro 2015 software (Originlab, Northampton, MA). The difference in the shapes of the Langmuir isotherms for ILs and miRNAs can be due to the variations in their association rates.[43] The K_{ads} values obtained for IL-6, IL-8, miRNA-21, and miRNA-55 were 2.50 (± 0.17) x 10^7 M^{-1}, 6.10 (± 1.08) x 10^7 M^{-1}, 7.00 (± 0.76) x 10^8 M^{-1} and 7.47 (± 1.10) x 10^8 M^{-1}, respectively. At a bulk concentration equal to $1/K_{ads}$, the concentrations of capture probes at 50% surface coverage ($C_{\theta 0.5}$) were determined. We

found $C_{\theta 0.5}$ values of 40.1, 22.4, 1.4, and 1.2 nM for IL-6, IL-8, miRNA-21, and miRNA-155, respectively.

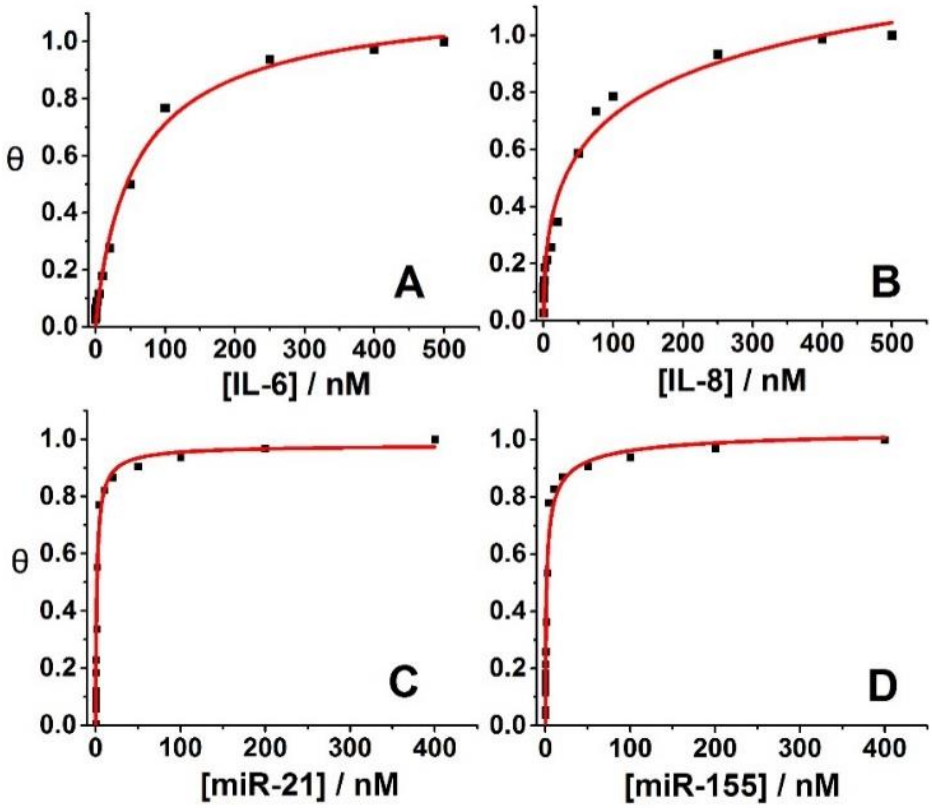

Figure 7. Representative plots of the relative surface coverage (θ) as a function of the concertation of **A.** IL-6, **B.** IL-8, **C.** miRNA-21, and **D.** miRNA-155. The solid line represents the Langmuir isotherm fit to the data. All measurements were made in triplicates.

Table 4. Detection performance comparison of our method with other SPR methods.

Analyte	**Matrix used for calibration**	**Surface receptor**	**Amplification method**	**Dynamic range**	**Detection limit**	**Ref**
IL-8	Cellular elements removed saliva	Anti-IL-8 antibody	Monoclonal second antibody	9.5 - 191 pM (in buffer)	184 pM	44
Thrombin	20 mM HEPES buffer (pH 7.4)	DNA-aptamer	Different shapes of Au NPs	Up to 200 nM	Cages:1 fM Rods:10 aM Quasi-spheres:1 aM	45
C-reactive protein (CRP)	1% human serum in diluted in 10 mM Tris, 15 mM NaCl and 2 mM $CaCl_2$ (pH 7.4)	biotinylated aptamers	CRP-Specific Aptamer reacted with Quantum dots	5 – 5000 fg mL^{-1}	5 fg mL^{-1}	10
miRNA-21	10 mM PBS (pH 7.4)	Stem-loop DNA	AuNPs and DNA supersandwich*	-	8 fM	46

miRNA-15a	0.1 M PBS (pH 7.0)	Hairpin capture DNA	Orthogonal signal amplification	5 fM - 0.5 nM	0.5 fM	47
miRNA-21	10 mM PBS (pH 7.4)	Stem-loop DNA	Ag NPs adsorbed to DNA supersandwich* on DNA-linked AuNPs	-	0.6 fM	48
miRNA-141	10 mM PBS (pH 7.4)	DNA oligonucleotide	DNA-linked AuNPs-MoS_2 Nanocomposite	-	0.5 fM	49
Insulin glucagon somatostatin	PBS	Insulin glucagon somatostatin antigens	Direct binding of antibodies to their respective antigens	Insulin: 34 - 633 ng mL^{-1} Glucagon: 85 - 1592 ng mL^{-1} Somatostatin: 719 - 4000 ng mL^{-1}	Insulin: 1 nM Glucagon: 4 nM Somatostatin: 246 nM	50
Fibronectin	PBS (pH 7.4)	anti-fibronectin antibody	Direct antigen bound to antibodies	5 - 400 ng mL^{-1}	1.5 ng mL^{-1}	51

IL-1β IL-6 IFN-γ TNF-α	PBS with 0.075% Tween 80 and 0.5% BSA	Capture antibodies for the respective antigens	Neutravidin and a gold nanoparticle cascade	7 logarithms (100 fg mL^{-1} - 1 μg mL^{-1} test range)	IL-1β: 1.2 pg mL^{-1} IL-6: 50 fg mL^{-1} IFN-γ: 22 pg mL^{-1} TNF-α:15 pg mL^{-1}	52
IL-6 IL-8 miRNA-21 miRNA-155	10% normal human serum diluted in PBS (pH 7.4)	Hairpin capture DNA for miRNAs and capture antibodies of ILs	Fe_3O_4@Au bimetallic NPs tagged detection molecules	IL-6: 0.02 - 100 nM IL-8: 0.01 - 75 nM miRNA-21: 50 fM - 2 nM miRNA-155: 25 fM - 4 nM	IL-6: 28 pM IL-8: 18 pM miRNA-21: 502 fM miRNA-155: 483 fM	This work

5.4 Conclusions

The designed surface plasmon microarray platform offers multiplexed assaying of ILs and miRNAs directly from human serum samples. The combined magnetic and plasmon enhancing features of Fe_3O_4@Au NPs were useful for separating the attached detection probes easily and amplifying the SPRi signal output while minimizing the non-specific signals arising from the serum matrix. These features improved the selectivity and sensitivity of the assay. The binding constants observed from the μM to nM range provide evidence for strong affinities between the analyte biomarkers and their receptor molecules on the designed sensor surface. Broader application of this approach to other proteins and miRNA biomarkers is feasible.

5.5 References

1. Mehta, S.; Shelling, A.; Muthukaruppan, A.; Lasham, A.; Blenkiron, C.; Laking, G.; Print, C. *Ther. Adv. Med. Oncol*. **2010**, *2*, 125-148.
2. de Planell-Saguer, M.; Rodicio, M. C. *Anal. Chim. Acta*, **2011**, *699*, 134-152.
3. Wu, L.; Qu, X. *Chem. Soc. Rev.* **2015**, *44*, 2963-2997.
4. Maley, A.M.; Lu, G.J.; Shapiro, M.G.; Corn, R.M. *ACS Nano*, **2017**, *11*, 7447-7456.
5. Manuel, G.; Lupták, A.; Corn, R.M. *J. Phys. Chem. C.* **2016**, *120*, 20984-20990.
6. Shen, M.; Joshi, A.A.; Vannam, R.; Dixit, C.K.; Hamilton, R.G.; Kumar, C.V.; Rusling, J.F.; Peczuh, M.W. *ChemBioChem*, **2017**, *19*, 197-197.
7. Walgama, C.; Al Mubarak, Z. H.; Zhang, B.; Akinwale, M.; Pathiranage, A.; Deng, J.; Berlin, K. D.; Benbrook, D. M.; Krishnan, S. *Anal. Chem.* **2016**, *88*, 3130–3135.
8. Singh, V.; Nerimetla, R.; Yang, M.; Krishnan, S., *ACS Sensors*, **2017**, *2*, 909-915.
9. Krishnan, S.; Mani, V.; Wasalathanthri, D.; Kumar, C. V.; Rusling, J. F. *Angew. Chem. Int. Ed.* **2011**, *50*, 1175 –1178.
10. Vance, S.A.; Sandros, M.G. *Sci. Rep*. **2014**, *4*, 5129.
11. He, L.; Pagneux, Q.; Larroulet, I.; Serrano, A.Y.; Pesquera, A.; Zurutuza, A.; Mandler, D.; Boukherroub, R.; Szunerits, S. *Biosens. Bioelectron*. **2017**, *89*, 606-611.
12. Chinen, A.B.; Guan, C.M.; Ferrer, J.R.; Barnaby, S.N.; Merkel, T.J.; Mirkin, C.A. *Chem. Rev.* **2015**, *115*, 10530-10574.
13. Howes, P.D.; Chandrawati, R.; Stevens, M.M. *Science*, **2014**, *346*, 1247390.
14. Zaleska-Medynska, A.; Marchelek, M.; Diak, M.; Grabowska, E. *Adv. Colloid. Interface. Sci.* **2016**, *229*, 80-107.
15. Zhang, C.; Chen, B.Q.; Li, Z.Y.; Xia, Y.; Chen, Y.G. *J. Phys. Chem. C*. **2015**, *119*, 16836-16845.

16. Srinoi, P.; Chen, Y.T.; Vittur, V.; Marquez, M.D.; Lee, T.R. Preprints, **2018** (doi:10.20944/preprints201804.0104.v1)
17. Pham, T.T.H.; Cao, C.; Sim, S.J. *J. Magn. Magn. Mater*, **2008**, *320*, 2049-2055.
18. Jain, P.K.; Xiao, Y.; Walsworth, R.; Cohen, A.E. *Nano Lett.* **2009**, *9*, 1644-1650.
19. Saha, K.; Agasti, S.S.; Kim, C.; Li, X.; Rotello, V.M. *Chem. Rev.* **2012**, *112*, 2739-2779.
20. Sperling, R.A.; Parak, W.J. Philos. *Trans. Royal Soc. A: Math. Phys. Eng*, **2010**, *368*, 1333-1383.
21. Brown, K.R.; Walter, D.G.; Natan, M.J., *Chem. Mater*. **2000**, *12*, 306-313.
22. Kumari, N.; Dwarakanath, B.S.; Das, A.; Bhatt, A.N. *Tumour Biol.* **2016**, *37*, 11553-11572.
23. Alfaro, C.; Sanmamed, M.F.; Rodríguez-Ruiz, M.E.; Teijeira, Á.; Oñate, C.; González, Á.; Ponz, M.; Schalper, K.A.; Pérez-Gracia, J.L.; Melero, I. *Cancer Treat. Rev*. **2017**, *60*, 24-31.
24. Komatsu, S.; Ichikawa, D.; Kawaguchi, T.; Miyamae, M.; Okajima, W.; Ohashi, T.; Imamura, T.; Kiuchi, J.; Konishi, H.; Shiozaki, A.; Fujiwara, H. *Am. J. Cancer Res*. **2016**, *6*, 1511.
25. Jurkovicova, D.; Magyerkova, M.; Kulcsar, L.; Krivjanska, M.; Krivjansky, V.; Gibadulinova, A.; Oveckova, I.; Chovanec, M. *Neoplasma*, **2014**, *61*, 241-251.
26. Desjardins, P.; Conklin, D. *J. Vis. Exp*. **2010**, *45*.
27. Winge, R. K.; Peterson, V. J.; Fassel, V. A. *Appl. Spectrosc*. **1979**, *33*, 206-219.
28. Gentry, S. T.; Kendra, S. F.; Bezpalko, M. W. *J. Phys. Chem. C.* **2011**, *115*, 12736.
29. Premaratne, G.; Nerimetla, R.; Matlock, R.; Sunday, L.; Hikkaduwa Koralege, R. S.; Ramsey, J. D.; Krishnan, S. *Catal. Sci. Technol.* **2016**, *6*, 2361–2369.
30. Premaratne, G.; Farias, S.; Krishnan, S. *Anal. Chim. Acta*. **2017**, *970*, 23–29.
31. Petkova, G.A.; Záruba, K.; Žvátora, P.; Král, V. *Nanoscale Res. Lett*. **2012**, *7*, 287.
32. Premaratne, G.; Al Mubarak, Z.; Senavirathna, L.; Liu, L.; Krishnan, *Sens. Actuator B Chem.* **2017**, *253*, 368–375.
33. Mirkin, C.A.; Letsinger, R.L.; Mucic, R.C.; Storhoff, J.J. *Nature*, **1996**, *382*, 607.
34. Mustafaoglu, N.; Kiziltepe, T.; Bilgicer, B. *Nanoscale*, **2017**, *9*, 8684-8694.

35. Nobbmann, U.; Connah, M.; Fish, B.; Varley, P.; Gee, C.; Mulot, S.; Chen, J.; Zhou, L.; Lu, Y.; Sheng, F.; Yi, J. *Biotechnol. Genet. Eng. Rev*. **2007**, *24*, 117-128.

36. Ducancel, F.; Muller, B.H. Molecular engineering of antibodies for therapeutic and diagnostic purposes. *In MAbs*, Taylor & Francis, **2012**, *4*, 445-457.

37. Götting, N.; Fritz, H.; Maier, M.; Von Stamm, J.; Schoofs, T.; Bayer, E. *Colloid Polym. Sci*. **1999**, *277*, 145-152.

38. Hseu, Z.Y.; Chen, Z.S.; Tsai, C.C.; Tsui, C.C.; Cheng, S.F.; Liu, C.L.; Lin, H.T. *Water Air Soil Pollut*. **2002**, *141*, 189-205.

39. Sugawa, K.; Tahara, H.; Yamashita, A.; Otsuki, J.; Sagara, T.; Harumoto, T.; Yanagida, S. *ACS Nano*, **2015**, *9*, 1895-1904.

40. Bonnet, G.; Tyagi, S.; Libchaber, A.; Kramer, F.R. Proc. Natl. Acad. Sci. 1999, 96, 6171-6176

41. Tyagi, S.; Bratu, D.P.; Kramer, F.R. *Nature Biotechnol.* **1998**, *16*, 49-53.

42. Lee, H.J.; Wark, A.W.; Corn, R.M. *Langmuir*, **2006**, *22*, 5241-5250.

43. O'Shannessy, D.J.; Brigham-Burke, M.; Soneson, K.K.; Hensley, P.; Brooks, I. *Methods. Enzymol.* **1994**, *240*, 323-349.

44. Yang, C.Y.; Brooks, E.; Li, Y.; Denny, P.; Ho, C.M.; Qi, F.; Shi, W.; Wolinsky, L.; Wu, B.; Wong, D.T.; Montemagno, C.D. *Lab Chip*. **2005**, *5*, 1017-1023.

45. Kwon, M.J.; Lee, J.; Wark, A.W.; Lee, H.J. *Anal. Chem.* **2012**, *84*, 1702-1707.

46. Wang, Q.; Liu, R.; Yang, X.; Wang, K.; Zhu, J.; He, L.; Li, Q. *Sens. Actuators B. Chem*. **2016**, *223*, 613-620.

47. Hu, F.; Xu, J.; Chen, Y. *Anal. Chem.* **2017**, *89*, 10071-10077.

48. Liu, R.; Wang, Q.; Li, Q.; Yang, X.; Wang, K.; Nie, W. *Biosens. Bioelectron.* **2017**, *87*, 433-438.

49. Nie, W.; Wang, Q.; Yang, X.; Zhang, H.; Li, Z.; Gao, L.; Zheng, Y.; Liu, X.; Wang, K. *Anal. Chim. Acta*. **2017**, *993*, 55-62.

50. Castiello, F.R.; Tabrizian, M. *Anal. Chem.* **2018**, *90*, 3132-3139.

51. Sankiewicz, A.; Romanowicz, L.; Pyc, M.; Hermanowicz, A.; Gorodkiewicz, E. *J. Pharm. Biomed. Anal.* **2018**, *150*, 1-8.

52. Hendriks, J.; Stojanovic, I.; Schasfoort, R.B.; Saris, D.B.; Karperien, M. *Anal. Chem*. **2018**, *90*, 6563-6571.

CHAPTER 6

SUMMARY

Development of robust and sensitive analytical approaches for the detection of biomarkers present in clinical matrices pave an attractive direction towards future diagnostics. As a result, clinicians could not only diagnose deadly diseases at a preliminary stage, but also plan suitable therapeutic protocols and monitor their outcomes. This dissertation discussed different nano-inspired electrochemical and optical analytical methodologies that were developed for small and large molecule biomarker measurement in view of advancing the field of biosensors. A summary of the objectives and associated key contributions under each chapter is presented below:

The first chapter of this dissertation attempted to summarize and recognize the recent scientific contributions made on developing sensitive biosensor approaches for clinically relevant small and large molecule biomarker measurements. A literature review was conducted on novel electrochemical sensor methodologies, which combined the advancements in nanochemistry and the biorecognition elements such as enzymes, aptamers, antigens and antibodies. Furthermore, SPRi based approaches for multiplexed biomarker measurement were summarized. The combination of elegant nanomaterials was useful for detection signal amplification, increasing surface functional groups as well as highly oriented bioreceptor immobilization, and minimization of the non-specific interactions of molecules other than the biomarker of interest present in the sample matrices (e.g., serum, urine). The research field on electrochemical and SPRi biosensors is exponentially growing and many more novel discoveries are anticipated in the near future.

The second chapter reported an amperometric nano-bioelectrode design that uniquely combined 1-pyrenebutyric acid units pi-pi stacked with carboxylated multiwalled carbon nanotubes on the surface of gold screen printed electrodes for covalent attachment of NAD^+ dependent formaldehyde dehydrogenase (FDH). The designed enzyme bioelectrode offered 6 ppb formaldehyde detection in 10-times diluted urine with a wide dynamic range of 10 ppb to 10 ppm. Fourier transform infrared, Raman, and electrochemical impedance spectroscopic characterizations confirmed the successful design of the FDH bioelectrode. Flow injection analysis provided lower detection limit and greater affinity for formaldehyde (apparent K_M 9.6 ± 1.2 ppm) when compared with stirred solution method (apparent K_M 19.9 ± 4.6 ppm). Selectivity assays revealed that the bioelectrode was selective toward formaldehyde with a moderate cross-reactivity for acetaldehyde (~ 25%) and negligible cross-reactivity toward propanaldehyde, acetone, methanol, and ethanol. This methodology can be broadly applied for measuring other small molecule biomarkers by tuning marker specific enzymes.

The next study focused on correlating picomolar affinities between surface plasmon and electrochemical immunoassays for the binding of serum glutamic acid decarboxylase-65 autoantibody (GADA), a biomarker of type 1 diabetes, to its antigen GAD-65. Carboxylated (~ 5.0%) graphene modified immunoassembly on a gold surface plasmon chip or on an electrochemical array provided significantly greater binding affinity, sensitivity, and lower detection limits than a self-assembled monolayer surface of mercaptopropionic acid (MPA). Estimation of the relative surface–COOH groups by covalent tagging of an electroactive aminoferrocene showed that the graphenyl surface displayed greater number of –COOH groups than the MPA surface. Additionally, the binding constant values obtained for the GADA-GAD65 binding through real-time SPRi studies can be useful as a quality control checkpoint for reproducible and reliable production of large-scale biosensors for clinical bioassays.

The fourth chapter focused on comparing detection performances of a quartz crystal microbalance (QCM), which is a mass sensor, with that of a surface plasmon resonance (SPR) microarray for an

oligonucleotide mimic of microRNA-21 biomarker. Surface immobilized capture oligonucleotide probe was used to hybridize with the target oligonucleotide (i.e., the microRNA-21 mimic) to facilitate selective detection. To obtain ultra-low femtomolar (fM) detection sensitivity, gold nanoparticles (50 nm) were conjugated with the target oligonucleotide. Detection limits of 28 and 47 fM were achieved for the target oligonucleotide by the QCM and SPRi microarray, respectively. Additionally, sample recovery study and matrix effect analysis was performed for the target oligonucleotide. Although the QCM had a lower detection limit, the microarray approach offered better throughput for analysis of up to 16 samples. We confirmed that the designed assay was selective for the target oligonucleotide and did not show signals for the control oligonucleotide with five mismatch sites relative to the target sequence. Combination of the QCM and microarray methods that utilize the same assay chemistry on gold are useful for overcoming clinical sample matrix effects and achieving ultra-low detection of small nucleotide biomarkers with quantitative insights.

In the final chapter, a surface plasmon resonance imager (SPRi) microarray employing citrate-stabilized Fe_3O_4@Au core/shell nanoparticles (NPs) as the plasmon signal amplification label was presented. A 4-channel microfluidic system was designed to demonstrate the feasibility for multiplexed assaying of two serum protein markers, interleukin-6 (IL-6) and interleukin-8 (IL-8) by a sandwich immunoassay, and two serum microRNA markers (miRNA-21 and miRNA -155) by a double hybridization assay. The Fe_3O_4@Au (105 nm) NPs exhibited 13-times higher plasmon signal intensities than that of only Fe_3O_4 (100 nm) and 6-times greater signals than Au only NPs (100 nm). The detection limits achieved for the markers were in the pM to sub-pM concentrations. The dynamic range of detection for the proteins was from pM to nM concentration in 10% serum, and for the miRNAs the dynamic range was from fM to nM in 10% serum. Additionally, the strength of selective binding interaction between the analyte biomarkers and their surface bioreceptors was assessed by the Langmuir-type binding kinetics. The binding constants estimated for IL-6, IL-8, miRNA -21 and miRNA -155 were 2.50 (±0.17) x 10^7 M^{-1}, 8.10 (±1.08) x 10^7 M^{-1},

7.00 (±0.76) x 10^8 M^{-1} and 7.47 (±1.10) x 10^8 M^{-1}, respectively. The synergistic multiplexed biosensing and kinetic assessment features associated with SPRi can be useful to measure potential disease biomarkers and make decisions on the surface biorecognition elements on their suitability for the assay.

In summary, the studies discussed in the dissertation suggest that highly sensitive, selective, and wide dynamic range analytical methods are of paramount significance for assaying biomarkers, which are typically present at very low levels in complex clinical matrices (e.g., whole blood, serum, saliva, tissues, and urine). The presented electrochemical biosensor methodologies offered highly sensitive electrochemical detection of biomarkers with minimum background effects as a result of the functionalization strategies employed. Also, similar nanobio-modifications can be adopted to expand the current electrode systems into multi-array formats for multiple biomarkers measurement and validation studies. With the recently growing attention on SPRi in clinical chemistry, this dissertation adds further significance for applications in biomarker identification and validation assays offering both binding insights and '3D' image based assay results.

VITA

Aluth Gedara Gayan Chandima Premaratne

Candidate for the Degree of

Doctor of Philosophy

Dissertation: ELECTROCHEMICAL AND OPTICAL BIOASSAY FOR CIRCULATING BIOMARKERS

Major Field: Analytical Chemistry

Education:
Completed the requirements for the Doctor of Philosophy in Chemistry at Oklahoma State University, Stillwater, Oklahoma in July 2018.
Completed the requirements for the Master of Science in Analytical Chemistry at University of Colombo, Sri Lanka in June 2014
Completed the requirements for the Bachelor of Science in Microbiology, Botany and Chemistry at St. Joseph's College of Arts and Science (affiliated to University of Bangalore), India in May 2010.

Experience:
Graduate Assistant, Department of Chemistry, Oklahoma State University (2013 – 2018)

- Research experience – Development of bioassays for disease-related biomarker measurements in clinical matrices, voltage driven microsomal and bactosomal drug metabolizing platforms, protein-nanoconjugates for biocatalytic applications.
- Teaching experience - Taught chemistry laboratory courses in general chemistry I (CHEM 1314), general chemistry II (CHEM 1515), quantitative analysis (CHEM 2122), and modern methods of chemical analysis (CHEM 4020).

Fellowships, Scholarships and Awards:

- Robberson Summer Dissertation Fellowship – OSU Graduate College (2017)
- 2nd place of Arts and Science Graduate 3MT competition – OSU Graduate College (2017)
- Travel Awards – American Chemical Society and Electrochemical Society (2016 – 2017)
- Skinner Fellowship and O. C. Dermer Award – Department of Chemistry (2013 – 2017)

Leadership and Service:

- Chair – Oklahoma Chapter of the Electrochemical Society (2017 – 2018)
- President – Phi Lambda Upsilon Chemical Society (2017 – 2018)
- Vice President – International Student Organization (2015 – 2016)

Professional Memberships:
Electrochemical Society, American Chemical Society, Phi Kappa Phi Honor Society